

Rochester Institute of Technology

RIT Digital Institutional Repository

Theses

8-2-2023

Purification and Detection of Antibiotic-resistant Bacteria from Whole Blood with Nano-sieve

Xinye Chen
xxc6180@rit.edu

Follow this and additional works at: <https://repository.rit.edu/theses>

Recommended Citation

Chen, Xinye, "Purification and Detection of Antibiotic-resistant Bacteria from Whole Blood with Nano-sieve" (2023). Thesis. Rochester Institute of Technology. Accessed from

This Dissertation is brought to you for free and open access by the RIT Libraries. For more information, please contact repository@rit.edu.

R.I.T

Purification and Detection of Antibiotic-resistant Bacteria from Whole Blood with Nano-sieve

by

Xinye Chen

A dissertation submitted in partial fulfillment of the requirements
for the degree of Doctorate of Philosophy in Microsystems Engineering

Microsystems Engineering Program
Kate Gleason College of Engineering

Rochester Institute of Technology
Rochester, New York
August 2nd, 2023

**Purification and Detection of Antibiotic-resistant Bacteria
from Whole Blood with Nano-sieve**

by

Xinye Chen

Committee Approval:

We, the undersigned committee members, certify that we have advised and/or supervised the candidate on the work described in this dissertation. We further certify that we have reviewed the dissertation manuscript and approve it in partial fulfillment of the requirements of the degree of Doctor of Philosophy in Microsystems Engineering.

Dr. Ke Du Assistant Professor, Chemical and Environmental Engineering	Date
--	------

Dr. Thomas Gaborski Professor, Department of Biomedical Engineering	Date
--	------

Dr. Blanca Lapizco-Encinas Professor, Department of Biomedical Engineering	Date
---	------

Dr. Ruoqian (Roger) Wang Assistant Professor, Civil and Environmental Engineering	Date
--	------

Dr. Shiyu Xu Senior Principal Scientist, Colgate Palmolive	Date
---	------

Certified by:

Dr. Stefan Preble Director, Microsystems Engineering Program	Date
---	------

ABSTRACT

**Kate Gleason College of Engineering
Rochester Institute of Technology**

Degree: Doctor of Philosophy

Program: Microsystems Engineering

Authors Name: Xinye Chen

Advisors Name: Dr. Ke Du

Dissertation Title: Purification and Detection of Antibiotic-resistant Bacteria from Whole Blood with Nano-sieve

Life-threatening bloodstream infections (BSI), such as sepsis, mainly caused by the body's syndromic response to pathogen infection, are a major public health concern, leading to ~11 million deaths each year. The identification of sepsis presents significant challenges in the diagnostic process, as the isolation of low concentration pathogens from bodily fluids (e.g., human blood) is extremely demanding, and typically relies on time-consuming and complicated isolation processes. Therefore, this work aims to explore the potential of microfluidics as a powerful tool for rapid purification and concentration of antibiotic-resistant bacteria (ARB) from blood samples, meanwhile developing a molecular diagnostic technology by combining a recombinase polymerase amplification (RPA) with clustered regularly interspaced short palindromic repeats (CRISPR) and CRISPR-associated proteins (Cas), aiming to rapidly and accurately targeting the specific genetic marker or DNA sequences unique to the bacteria of interest.

A novel pneumatically-regulated nano-sieve device is successfully designed and fabricated for purifying and concentrating the target bacteria, such as Methicillin-resistant *Staphylococcus aureus* (MRSA), by applying a three-dimensional (3-D) beads-stacked

microstructure within the nano-scale channel (~200 nm in depth). Leveraging this deformable nanosystem, the captured bacteria can be retrieved from the channel by retrieving with a small volume (e.g., 30 μL) of fresh buffer solution, which makes the collected sample directly eligible for downstream analysis. An on-chip concentration factor of 15 has been achieved while dealing with a 600 μL MRSA-spiked sample under a low concentration of 100 colony forming unit (CFU)/mL. As expected, RPA/CRISPR-Cas system offers a naked-eye detection after a multiplexing purification of MRSA by nano-sieve device under a flow rate of 4 $\mu\text{L}/\text{min}$ per channel. This suggests that the integration of proposed nano-sieve device and RPA/CRISPR-Cas technique enables the purification and concentration of a low-concentration bacteria sample, potentially suitable for identifying sepsis-causing pathogens from whole blood.

ACKNOWLEDGMENTS

I would like to express my deepest gratitude to my academic supervisors, Dr. Ke Du, and Dr. Jiandi Wan, for their unwavering guidance, invaluable insights, and continuous support throughout the entire research process regarding the fundamental microfluidics and biosensing techniques. Their patience and encouragement have been instrumental in shaping this dissertation and my academic growth. I am truly fortunate to have such dedicated mentors who challenged and inspired me to reach new heights.

I am thankful to all members of my dissertation committee, Dr. Tom Gaborski, Dr. Blanca Lapizco-Encinas, Dr. Ruoqian (Roger) Wang, and Dr. Shiyu Xu, for their valuable feedbacks, constructive criticism, and scholarly inputs. Their expertise in the field has significantly enhanced the quality of this research. I am grateful for their time, insightful discussions, and the thoughtful suggestions that have shaped the final outcome of this dissertation.

I am immensely grateful to the participants of this study, including Dr. Yu Gan, Dr. Jie Zhang, Grant Korensky, Shuhuan Zhang, Abby Miller, and so on. Their cooperation and willingness to share their experiences and insights have made this research possible. Their contributions have enriched the findings and added depth to the understanding of the topic. I sincerely appreciate their time and willingness to engage in this study.

I extend my heartfelt appreciation to the Microsystems Engineering at Rochester Institute of Technology for providing the necessary resources, research facilities, and

academic support that have been integral to the successful completion of this study. The access to the library, laboratory equipment, and research materials has been vital in conducting experiments, analyzing data, and drawing meaningful conclusions. Especially, I would like to calling out Mrs. Lisa Zimmerman for her consistent support of me, as well as Dr. Bruce Smith and Dr. Stefan Preble for creating a positive and unique degree experience.

Furthermore, I would like to acknowledge the financial support received from The National Institutes of Health (NIH). Their generous funding played a pivotal role in enabling the execution of this research project. I am grateful for their belief in the importance of this work and their investment in advancing scientific knowledge in the field.

Last but not least, I am indebted to my family, friends, and loved ones for their unwavering support, patience, and understanding throughout this challenging journey. Their constant encouragement, love, and belief in my abilities have been my pillar of strength, and I am immensely grateful for their presence in my life.

In conclusion, this dissertation would not have been possible without the contributions, support, and encouragement of the individuals and organizations mentioned above. Their collective efforts have played an integral role in the successful completion of this research, and for that, I am sincerely thankful.

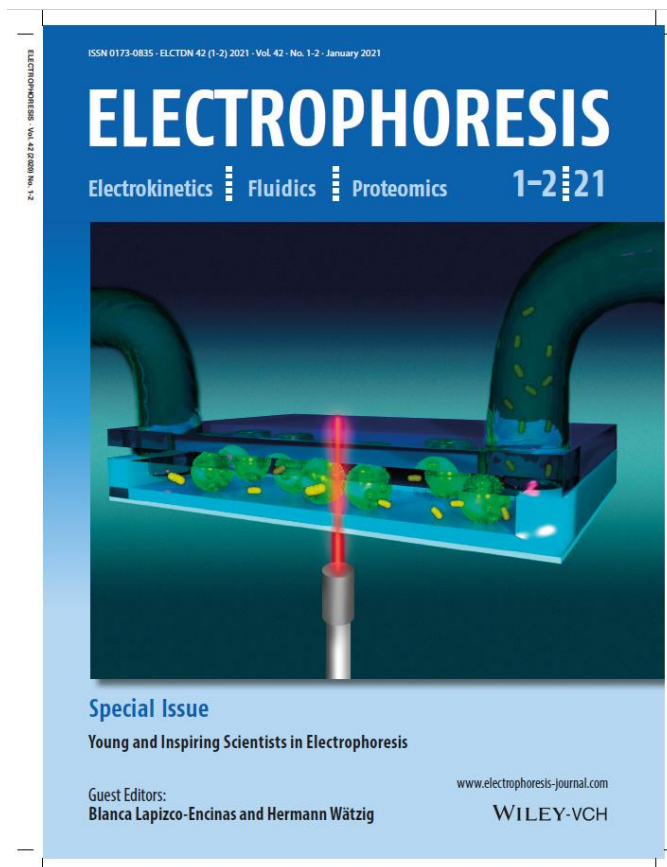
LIST OF PUBLICATIONS

First Authored Peer-reviewed Journal Publications

- 1) **Chen, X.**, Ryan, K.M., Hines, D., Pan, L., Du, K. and Xu, S., 2023. Three-dimensional visualization of dentine occlusion based on FIB-SEM tomography. *Scientific Reports*, 13(1), p.2270.
- 2) **Chen, X.**, Zhang, S., Gan, Y., Liu, R., Wang, R.Q. and Du, K., 2022. Understanding microbeads stacking in deformable Nano-Sieve for Efficient plasma separation and blood cell retrieval. *Journal of Colloid and Interface Science*, 606, pp.1609-1616.
- 3) Korensky, G. §, **Chen, X.** §, Bao, M., Miller, A., Lapizco-Encinas, B., Park, M. and Du, K., 2021. Single *Chlamydomonas reinhardtii* cell separation from bacterial cells and auto-fluorescence tracking with a nanosieve device. *Electrophoresis*, 42(1-2), pp.95-102.

§ *Both authors have contributed equally to this work*

* **Front cover**



- 4) **Chen, X.**, Miller, A., Cao, S., Gan, Y., Zhang, J., He, Q., Wang, R.Q., Yong, X., Qin, P., Lapizco-Encinas, B.H. and Du, K., 2020. Rapid *Escherichia coli* trapping and retrieval from bodily fluids via a three-dimensional bead-stacked nanodevice. *ACS applied materials & interfaces*, 12(7), pp.7888-7896.

* **Selected complementary cover**



- 5) **Chen, X.**, Falzon, L., Zhang, J., Zhang, X., Wang, R.Q. and Du, K., 2019. Experimental and theoretical study on the microparticle trapping and release in a deformable nano-sieve channel. *Nanotechnology*, 31(5), p.05LT01.

Co-Authored Peer-reviewed Journal Publications

- 1) Nanaware, A., Kranbuhl, T., Ching, J., Chen, J.S., **Chen, X.**, Tu, Q. and Du, K., 2022. Pneumatic controlled nanosieve for efficient capture and release of nanoparticles. *Journal of Vacuum Science & Technology B*, Nanotechnology and Microelectronics: Materials, Processing, Measurement, and Phenomena, 40(6), p.063002.

- 2) Yang, J., He, Y., Zhang, X., Yang, W., Li, Y., Li, X., Chen, Q., **Chen, X.**, Du, K., Yan, Y., 2021. Improving the electrical conductivity of copper/graphene composites by reducing the interfacial impurities using spark plasma sintering diffusion bonding. *Journal of Materials Research and Technology* 15, 3005–3015.
- 3) Ma, M.C., Li, G., **Chen, X.**, Archer, L.A. and Wan, J., 2021. Suppression of dendrite growth by cross-flow in microfluidics. *Science Advances*, 7(8), p.eabf6941.
- 4) Chang, Y., **Chen, X.**, Zhou, Y. and Wan, J., 2019. Deformation-based droplet separation in microfluidics. *Industrial & Engineering Chemistry Research*, 59(9), pp.3916-3921.
- 5) Fan, R., **Chen, X.**, Wang, Z., Custer, D. and Wan, J., 2017. Flow-Regulated Growth of Titanium Dioxide (TiO₂) Nanotubes in Microfluidics. *Small*, 13(30), p.1701154

* **Featured frontispiece**



TABLE OF CONTENTS

ABSTRACT	III
ACKNOWLEDGMENTS	V
LIST OF PUBLICATIONS	VII
TABLE OF CONTENTS	X
LIST OF FIGURES	XIII
LIST OF TABLES	XX
CHAPTER 1. GENERAL INTRODUCTION	1
1.1 <i>Background</i>	2
1.2 <i>The Current Diagnostic Workflow for BSI</i>	3
1.3 <i>Microfluidic Platform as a Powerful Tool for Diagnosing BSI</i>	5
1.3.1 <i>Bacteria Separation from Blood</i>	5
1.3.2 <i>On-chip Detection Followed by Microfluidic Separation</i>	9
1.3.3 <i>Downstream (off-chip) Analysis for Detecting Target Bacteria</i>	10
1.4 <i>Motivation and Objectives of This Study</i>	14
1.4.1 <i>Motivation</i>	14
1.4.2 <i>Objectives of This Study</i>	15
CHAPTER 2. THEORETICAL MODEL ON MICROPARTICLE TRAPPING AND RELEASING IN A DEFORMABLE NANO-SIEVE CHANNEL	18
2.1 <i>Introduction</i>	19
2.2 <i>Material and Methods</i>	20
2.2.1 <i>Fabrication of nano-sieve device</i>	20
2.2.2 <i>Microparticles trapping process</i>	21
2.2.3 <i>Spectrofluorometric Characterization</i>	21
2.3 <i>Results and Discussion</i>	22
2.4 <i>Conclusion</i>	30
CHAPTER 3. EXPERIMENTAL STUDY ON MICROPARTICLES TRAPPING AND RELEASING BY A ROBUST NANO-SIEVE DEVICE	31
3.1 <i>Introduction</i>	32
3.2 <i>Material and methods</i>	36
3.2.1 <i>Nano-device fabrication</i>	36
3.2.2 <i>Preparation of microparticles and nanoparticles</i>	37
3.2.1 <i>E. coli culture and staining</i>	37
3.2.2 <i>C. reinhardtii cell culture</i>	38
3.2.3 <i>C. reinhardtii cell trapping</i>	38
3.2.4 <i>Spectrofluorometric Characterization</i>	39

3.2.5	SEM imaging	39
3.3	<i>Experimental results</i>	39
3.3.1	Microparticles and nanoparticles trapping and releasing	41
3.3.2	Soft cells separation	44
3.4	<i>Discussion</i>	47
3.5	<i>Conclusion</i>	50

CHAPTER 4. A THREE-DIMENSIONAL (3-D) BEAD-STACKED NANODEVICE FOR RAPIDLY CAPTURING AND RETRIEVING BACTERIA FROM BLOOD PLASMA **52**

4.1	<i>Introduction</i>	53
4.2	<i>Materials and methods</i>	55
4.2.1	Nano-sieve device fabrication	56
4.2.2	Cell culture and labeling	56
4.2.3	Bead stacking and bacteria-trapping	58
4.2.4	CFD modeling	58
4.2.5	Tomography scanning	58
4.2.6	Segmentation via machine learning	59
4.2.7	Spectrofluorometric characterization	59
4.2.8	Fluorescence microscopy imaging	59
4.2.9	Scanning electron microscopy (SEM)	60
4.3	<i>Experimental results</i>	61
4.4	<i>Discussion</i>	68
4.5	<i>Conclusion</i>	73

CHAPTER 5. UNDERSTANDING THE 3-D MICROBEADS STACKING IN DEFORMABLE NANO-SIEVE FOR EFFICIENT PLASMA SEPARATION AND BLOOD CELL RETRIEVAL **74**

5.1	<i>Introduction</i>	75
5.2	<i>Materials and methods</i>	77
5.2.1	Materials	77
5.2.2	Preparation of PDMS	78
5.2.3	Hardness testing	78
5.2.4	Nano-sieve device fabrication	79
5.2.5	Microbeads stacking and characterization	79
5.2.6	OCT scanning and processing	79
5.2.7	Plasma separation and RBCs retrieval	80
5.3	<i>Experimental results</i>	80
5.4	<i>Discussion</i>	88
5.5	<i>Conclusion</i>	90

CHAPTER 6. COUPLING A MOLECULAR DIAGNOSTICS WITH BACTERIA CONCENTRATION BY A PNEUMATICALLY-REGULATED NANO-SIEVE DEVICE **92**

6.1	<i>Introduction</i>	93
6.2	<i>Materials and methods</i>	95
6.2.1	Device fabrication	96
6.2.2	Beads stacking deposition	97
6.2.3	Bacterial culture	97
6.2.4	Bacteria staining.....	98
6.2.5	RBCs depletion immunoassay.....	98
6.2.6	Bacteria capture and concentration.....	99
6.2.7	Fluorescence microscopy imaging.....	99
6.2.8	Nucleic acid preparation	100
6.2.9	RPA amplification and CRISPR-Cas12a detection	101
6.3	<i>Results and Discussion</i>	102
6.4	<i>Discussion</i>	112
6.5	<i>Conclusion</i>	114
CHAPTER 7. CONCLUSION AND FUTURE OPPORTUNITIES		115
7.1	<i>Research summary</i>	116
7.2	<i>Key contributions</i>	120
7.3	<i>Future opportunities</i>	123
7.3.1	Develop a pneumatically-regulated nano-sieve for targeting biomolecules	123
7.3.2	Study microalgae cells with a nano-sieve device for next-generation biosensor	126
CHAPTER 8. BIBLIOGRAPHY		130
APPENDIX A		146

LIST OF FIGURES

- Figure 1.1** The overview of current diagnostic workflow for BSI, including 1) samples from patient blood (5 - 10 mL) cultured in nutrient rich media (25 mL) for the presence of a pathogen; 2) the identification of pathogens based on culture methods or molecular methods; 3) the determination of antibiotic susceptibility. Reprinted from [19]. 3
- Figure 1.2** The schematic of microfluidic platform is based on soft inertial separation, presenting the curved and focused sample flow segment and the inertial force on fluid element. The image on top-left corner shows the curved and focused sample flow segment visualized by fluorescent dye. Reprinted from [39]..... 6
- Figure 1.3** The proposed device showing inertial focusing amplification for particle separation with a straight channel design with one inlet and three outlets. The separation process includes the migration of large particles by inertial lift to equilibrium positions, RBC migration closer to the channel wall, and collection of RBCs at the side outlets and bacteria at the middle outlet. Reprinted from [40]..... 7
- Figure 1.4** (a) Bacteria separation from RBC-bacteria mixture and the concentration of bacteria at the central area without RBC. (b) The SERS spectra of RBC, RBC-bacteria mixture, and the *S. aureus* dielectrokinetically separated from blood. Reprinted from [41]. 8
- Figure 1.5** Illustration of acoustic separation of bacteria from blood. The mixture of bacteria and blood flows from the side inlets in laminar flow while a density-matched buffer flows in the center inlet. Acoustophoresis causes the blood cells (red and white blood cells) to migrate laterally toward the center of the channel and out the center outlet, while bacteria respond weakly to the acoustic field to the side outlets. Reprinted from [37]..... 8
- Figure 1.6** The schematic of labeling RPA in solution as a molecular detection technique: two oligonucleotide primers form a complex with a recombinase (green ovals) and are directed to homologous sequences on the target sequence where they can invade the DNA double strand. The polymerase (blue) elongates the strand for the duplication. RPA runs continuously at 38 °C. A labeling of amplification product is achieved by using a reverse primer coupled with a Cy5 reporter dye (red). Reprinted from [48]. 11
- Figure 1.7** Schematic illustration of CRISPR/Cas12 mechanism. The Cas12 protein only needs CRISPR-RNA (crRNA) to create double-stranded breaks (DSBs). Cas12 protein cleaves the target region beside an adjacent protospacer motif (PAM) sequence (CTA, TTN, TTTN) with the help of the RuvC and nuclease lobe (NUC) domains. Once Cas12 is active, R-loop can be initiated, which forms base-pair (bp) hybridization between the crRNA and the target DNA strand. During this step, Cas12 matches the < 17 bp of the target sequence and leads to an R-loop formation. Once R-loop is formed, the Cas12 protein uses its active RuvC domain and generates a staggering cut in the non-target strand with the help of the PAM sequence. (RuvC stands for an *E. coli* protein involved in DNA repair). Reprinted from [58]. 12

Figure 1.8 The designed device based on deformable microfluidics. (a) The schematic presenting a proposed “nano-sieve” filtering system based on hydrodynamic deformation of PDMS roof. (b) The device modeled by Solidworks consists of a PDMS layer on the top and a glass substrate on the bottom. Blue dots mean the applied particles pumped into the channel, then trapped by the deformable PDMS roof. Red arrows present the flow direction. 14

Figure 2.1 The schematic of deformable microchannel with a compliant cover, where H is the initial height of microchannel, L is the length of microchannel, and W is the width of microchannel. u is the deformation of the top roof. Reprinted from [73]. 22

Figure 2.2 The fabrication process of a single channel for nano-sieve device. The SEM image with low-magnification and high-magnification to confirm the final height of microchannel. Reprinted from [73]. 24

Figure 2.3 The experimental deposition of particles within the microchannel. *Left*: a high-magnification image showing the highly-concentrated particles around the inlet. *Middle*: the entire profile of deposited particles within the fabricated microchannel. *Right*: a high-magnification image showing the concentrated particles close to the outlet. The dashed light-gold lines present the edges of channel. The white dashed-parabolic line means the predicted particle distribution of the developed theoretical model. Scale bar: 1 mm. Reprinted from [73]. 25

Figure 2.4 The capture efficiency of experimental results (solid red) and theoretical calculations (patterned blue) under various flow rates applied. Inset: the fluorescence intensity of serial dilution of the original microparticles solution that was applied for calculating the capture efficiency. Error bars are the standard deviation of the mean. Reprinted from [73]. 27

Figure 2.5 The capture efficiency of experimental results (purple) versus theoretical calculation with three different channel height. Error bars are the standard deviation of the mean. Reprinted from [73]. 28

Figure 2.6 The calculated capture efficiency based on the developed theoretical model. (a) the channel height as a function of flow rates. (b) the particle size versus flow rates. Reprinted from [73]. 29

Figure 3.1 Illustration of two methods for collapse-free nanoslit. (a) without glass support on the side of PDMS, roof collapse occurs as shown in inset; (b) with glass support on the side of PDMS, the stable roof is achieved. (c) the method of wafer filling to successfully create the nanoslit channels. Reprinted from [88]. 33

Figure 3.2 The fabrication flow of two-step sealing-and-reinforcement bonding paradigm for two different approaches that are used to create the SU-8 microchannel by photolithography (left) and the glass wet etching (right): the microchannel sidewalls are created through SU-8 photolithography (as) or glass wet etching (ag). At the sealing step, a PET film coated with a thin layer of SU-8 seals the microchannel sidewalls

(S1,s and S1,g). The chip is then illuminated by UV light and post-exposure baking to cure the adhesive layer (S2,s and S2,g). The slight SU-8 reflow can cause the round corners from the cross-sectional view. At the reinforcement step, a glass substrate coated with a SU-8 layer is attached to the bare side of the PET film (R1,s and R1,g). The sample is then illuminated by UV light and post-exposure baking to cure the adhesive layer at the bonding interface of the reinforcement glass and the PET film (R2,s and R2,g). Reprinted from [92].
 34

Figure 3.3 The fabrication process of nano-sieve device by using a dual photolithography. Reprinted from [93]. 35

Figure 3.4 (a) Microscope images of the sacrificial PR layer before (a-i) and after (a-ii) the acetone washing. (b) SEM images display the sacrificial PR layer in the channel with low magnification (b-i) and the channel height with high magnification. (c) The measured air flow rate versus the applied pressure in the nano-sieve channel with (red bars) and without (blue patterned bars) PR layer. The inset shows more details of the measurement regarding air flow rate. Reprinted from [93]. 40

Figure 3.5 (a) Fluorescent particles trapped in the channel with a parabolic pattern (a-i) toward the outlet. The inlet area: highly-concentrated particles were deposited (a-ii). (b) Fluorescent particles solution before (*left*) and after (*after*) filtration. Reprinted from [73].
 41

Figure 3.6 The measurement of fluorescent intensity from the filtered supernatant as a function of various flow rates. Inset: SEM image shows dried microparticles applied with the diameter of 5 μm (scale bar: 5 μm). Reprinted from [73]. 42

Figure 3.7 The measurement of fluorescent intensity from the filtered supernatant as a function of various flow rates. Inset: SEM image shows dried nanoparticles applied with the diameter of 100 nm (scale bar: 100 nm). Reprinted from [73]. 43

Figure 3.8 Schematic of experimental design for nano-sieve device trapping *C. reinhardtii* cells; (B) The optical micrograph exhibiting the practical device (left); the blue food dye is filled within the entire channel (right). Reprinted from [93]. 44

Figure 3.9 (a-i) The filtered solution and original solution collected in the centrifuge tube. The microscope images show the density of cells before (a-ii) and after (a-iii) the filtering process. (b) The *C. reinhardtii* cells trapped within the nano-sieve channel. The white arrow indicates the flow direction. The white dashed parabola shows the profile of the trapped cells. The enlarged region shows the dense *C. reinhardtii* cells. Reprinted from [93]. 45

Figure 3.10 (A) The *C. reinhardtii* cells capture efficiency as a function of various applied flow rates of (a) 4 $\mu\text{L}/\text{min}$; (b) 6 $\mu\text{L}/\text{min}$; (c) 8 $\mu\text{L}/\text{min}$, respectively. Reprinted from [93].
 46

Figure 3.11 The mixture of *E. coli* and *C. reinhardtii* cell separated by nano-sieve device, under the applied flow rate from (a) 4 $\mu\text{L}/\text{min}$; (b) 6 $\mu\text{L}/\text{min}$; (c) 8 $\mu\text{L}/\text{min}$, respectively.

The blue curve represents original solution, and the orange curve shows the filtered supernatant. Reprinted from [93]. 47

Figure 4.1 (a) Illustration of the magnetic beads stacked nano-sieve device for bacteria isolation: (a-i) beads trapped in the nano-sieve; (a-ii) pumping bacteria into the nano-sieve; (a-iii) bacteria retrieval via high flow rate buffer washing. (b) Magnetic beads trapping: (b-i) Experimental setup. Inset: photograph of beads stacked nano-sieve device. SEM images of the beads stacked nano-sieve channel: (b-ii) Left (high-magnification); (b-iii) Middle (low-magnification); (b-iv) Right (high-magnification). Fluorescence microscope image of the channel before (c) and after (d) bacteria-trapping. The white arrow indicates the flow direction. Reprinted from [94]. 60

Figure 4.2 (a) Beads stacking process during 72 s with a flow rate of 40 $\mu\text{L}/\text{min}$. The dashed purple box indicates the boundary of channel. The blue arrow indicates the flow direction. Scale bar: 4 mm. Reprinted from [94]. 62

Figure 4.3 The simulated results from computational fluid dynamics (CFD). Top: CFD calculation of nano-sieve deformation and beads flow pattern; bottom: flow velocity with a flow rate of (i) 20 $\mu\text{L}/\text{min}$; (ii) 30 $\mu\text{L}/\text{min}$; (iii) 40 $\mu\text{L}/\text{min}$; (iv) 50 $\mu\text{L}/\text{min}$. Reprinted from [94]. 63

Figure 4.4 (a) Optical coherence tomography scan of the beads stacked nano-sieve with the flow rate ranging from 20 - 50 $\mu\text{L}/\text{min}$. (b) Cross-section view of beads stacking: raw 2D image (top) and segmented 2D mask (bottom). (c) Experimentally measured volume of the deposited beads and maximum height in the channel after beads stacking. Reprinted from [94]. 64

Figure 4.5 (a) Uncorrected emission curve of filtered solution from nano-sieve with a flow rate of 8 $\mu\text{L}/\text{min}$: Original solution (pink); Stacked with only 10 μm beads (green); Stacked with mixed beads with sizes of 2.8 μm , 5 μm , and 10 μm (blue). The emission peaks are centered at ~ 520 nm. (b) Bacteria-trapping efficiency versus flow rate of nano-sieve only (yellow) and beads mixture stacked nano-sieve (patterned green). Reprinted from [94]. 65

Figure 4.6 (a-i) Photograph of the bacteria samples: Original (left); Filtered (middle); Retrieved (right). Fluorescence microscope image of original solution (a-ii), filtered solution (a-iii), and retrieved solution (a-iv). Scale bar: 10 μm . (b) Bacteria-trapping efficiency and retrieval efficiency from PBS (brown) and pig plasma (patterned blue). The applied flow rate is 8 $\mu\text{L}/\text{min}$. Error bars indicate standard deviation of the mean. Reprinted from [94]. 66

Figure 4.7 (a) Uncorrected emission curve of bacteria solution with various concentrations. The emission peak is centered at ~ 520 nm. The input bacteria concentration and volume are 1.11×10^7 CFU/mL and 1,300 μL , respectively (solid pink line). The retrieved sample is in 100 μL PBS (solid red line). Three other measured fluorescence intensities (colored dashed lines, marked as C_{ref}) indicate the stained bacteria stock solution with a concentration of 2.22×10^7 , 4.44×10^7 , and 1.11×10^8 CFU/mL, respectively. These references are used to calculate the concentration factor. Inset: Uncorrected emission curve

of filtered solution. (b) Fluorescence intensity versus bacteria concentration. The estimated concentration factor is 13 and the evaluated concentration factor is ~11. Error bars are standard error of the mean. (c) Fluorescence microscope image of original solution (left); filtered solution (middle); retrieved (right). Scale bar: 10 μm . Reprinted from [94]. 67

Figure 4.8 (a) The investigation on the trapping efficiency as a function of various *E. coli* bacteria concentrations, under a flow rate of 8 $\mu\text{L}/\text{min}$. (b) The linearity of three concentrations tested (from high to low: 5.55×10^8 , 1.11×10^8 , and 2.22×10^7 CFU/mL). Reprinted from [94]. 69

Figure 4.9 The washing process for retrieving the bacterial and magnetic beads from nano-sieve channel. (a) The trapped beads and bacteria; (b) The washed channel by PBS. Scale bar: 4 mm. 72

Figure 5.1 (a) Schematic of the microbeads packed nano-sieve device for the separation of blood cells and plasma. (b) Micrograph of the multiplexing nano-sieve system for plasma separation and RBCs retrieval. Reprinted from [195]. 81

Figure 5.2 The experimental procedure for separating plasma and retrieving RBCs from whole blood. (a) Beads stacking in the channel; (b) RBCs separation; (c) RBCs and microbeads collection; (d) RBCs extraction. Reprinted from [195]. 82

Figure 5.3 (a) Fluorescence microscope images of the packed microbeads in nano-sieve at various flow rates (20-60 $\mu\text{L}/\text{min}$) and PDMS curing agent/base ratio (1:5 to 1:20). Reprinted from [195]. 82

Figure 5.4 Measured volume and maximum height of the microbeads packed nano-sieve by OCT with curing agent/base ratio of: (a) 1:5; (b) 1:10; and (c) 1:20. Reprinted from [195]. 83

Figure 5.5 Measured mechanical properties of PDMS with a curing agent/base ratio ranging from 1:5 to 1:20: (a) Hardness. (b) Calculated elastic modulus. Reprinted from [195]. 84

Figure 5.6 Force analysis of a single microbead sandwiched between two deformable surfaces. Reprinted from [195]. 84

Figure 5.7 “Leaked” (red) versus “unleaked” nano-sieve (blue) at various flow rates observed under a fluorescence microscope. The grey dashed line is the “leaking” boundary based on the theoretical prediction, agreeing with the experimental results. Reprinted from [195]. 86

Figure 5.8 (a) Optical micrograph of a working nano-sieve for the isolation of plasma. The fluids at the outlet are more transparent as blood cells are removed. (b) Bright-field microscope image showing the microbeads pattern and captured RBCs: (i) low magnification; (ii) high magnification. (c) Microscope image of (i) original whole blood showing a high concentration of RBCs; (ii) Filtered plasma solution without RBCs. (iii) Retrieved RBCs from the nano-sieve. Reprinted from [195]. 87

Figure 6.1 The process flow of fabricating a pneumatically-controlled nano-sieve device, including the creation of nano-sieve channel (<i>Top row</i>), the PDMS pneumatic chamber (<i>Middle row</i>), and a PDMS thin film (<i>Bottom row</i>).	102
Figure 6.2 (a) The optical picture of an experimental multi-channel nano-sieve device filled with food dye. (b) The stacked beads array secured by the pneumatic layer with positive pressure (b-i) and the beads released by the pneumatic layer with negative pressure.	103
Figure 6.3 (a) Optical picture of <i>E.coli</i> -spiked whole blood before (left tube) and after (right tube) RBCs removal. (b) Fluorescence of the spiked bacteria before (b-i) and after (b-ii) removing RBCs from whole blood. The inserts show the comparison of RBCs density accordingly.	104
Figure 6.4 (a) Distribution of trapped bacteria under various low magnifications. The white arrow indicates the flow direction, and the yellow dashed line shows the region of 5 μm microbeads. The red dashed line is the interface of different sizes of microbeads. (b) Bacteria density before (b-i) and after (b-ii) nano-sieve filtering.	105
Figure 6.5 The time-lapse fluorescent images display the distribution of MRSA bacteria under the dynamic processing at the time of 30 minutes (a) and 60 minutes (b). The white arrow shows the flow direction. The green dots represent the MRSA bacteria stained by green dye.	106
Figure 6.6 The optical picture of multi-channels (blue dashed lines) nano-sieve device with a pneumatically-controlled layer (red dashed lines). Each channel has a magnetic beads array with various size of 5 μm and 10 μm in order.	106
Figure 6.7 The procedure of bacterial lysis and DNA purification by using the functional magnetic beads.	108
Figure 6.8 The schematic presents the mechanism of RPA amplification process, including (a) primers binding; (b) recombinase-mediated strand displacement and Primer extension; (c) amplification and strand displacement.	109
Figure 6.9 The schematic shows the mechanism of CRISPR-Cas12a system to cleave the target DNA and ssDNA with fluorophore-quencher molecules for a visual detection. The ssDNA probe is linked with fluorophore-quencher molecules. The crRNA means a guided RNA that is designed to be complementary for the target DNA sequence.	110
Figure 6.10 (a) The quantitative data plotted by introducing the fluorescence intensity versus various bacterial concentration from 10^3 to 10^1 CFU/mL. "NTC" refers to no template control. The data are represented as mean \pm standard deviation (n=3). For statistical analysis, ns, not significant = $p > 0.05$; * = $0.01 < p \leq 0.05$; ** = $0.001 < p \leq 0.01$; **** = $p \leq 0.0001$. (b) The endpoint image displays the visual detection by presenting the yellow-green fluorescence signal under the ultraviolet light.	111
Figure 7.1 (a) Schematic of the pneumatic controlled nano-sieve device. (b) SEM image of the microgrooves inside the channel with a feature size of 5 μm . (c) Schematic of the microgrooves patterned on the glass substrate with the introduced nanoparticles. (d) TEM	

image of the applied quantum dots. (e) Photograph of the channel: after target capture (e-i) and after target release (e-ii). Reprinted from 125

Figure 7.2 (A) The integrated fluorometer used to measure the auto-fluorescence signal from the trapped *C. reinhardtii* cells. (B) The auto-fluorescence intensity of *C. reinhardtii* cells under continuous excitation: (B-i) 0-50 s; (B-ii) 50-100 s; (B-iii) 100-150 s; (B-iv) 150-200 s; (B-v) 200-250 s. The background signal without *C. reinhardtii* cells is $\sim 1.9 \times 10^3$ a.u., which is over a full order of magnitude lower than the signal observed with *C. reinhardtii* cells. Reprinted from [93]. 128

LIST OF TABLES

Table 1.1. Physical characteristics of main blood components regarding a sepsis-causing pathogen (<i>E.coli</i>) [19].	4
Table 4.1 Conversion of <i>E. coli</i> cell number from cells/mL to CFU/mL [94].	57
Table 6.1 List of synthetic oligos sequence used in this study.	100
Table 6.2 Concentration factor after the bacterial retrieval by nano-sieve device.	107
Table A.1 Bill of Materials	146

Chapter 1. General Introduction

The content of this chapter provides an overview of the current landscape of antibiotic resistance and the relevant-septic infections, highlighting the magnitude of the problem and its impact on public health. It examines the advantages of microfluidic platforms and their potential applications in the field of bloodstream infections, such as sepsis. Additionally, this chapter also discusses the limitations of existing bacterial purification methods and the need to improve techniques for a rapid detection of antibiotic-resistant strains, meanwhile introducing a combined molecular technology for rapidly and specifically identifying the target bacteria with very low concentration.

1.1 Background

Antibiotic-resistant bacteria (ARB) is defined as the ability of bacteria or other microorganisms to develop resistance mechanisms against the specific antibiotics, which means the ARB can survive themselves and continue to grow by defeating the antibiotic drugs. Nowadays, the emergence and dissemination of ARB has become a rising concern for human health globally. The life-threatening bloodstream infections (BSI) caused by ARB, such as sepsis, have gradually led to increased treatment costs for patients [1], the longer hospitalization [2], [3], and most seriously, it could result in much higher rates of morbidity and mortality [4]–[6]. For example, sepsis is a leading cause of death and hospitalization due to sepsis costs the healthcare system more than any other conditions in the United States [7]–[9]. An early and rapid recognition of those ARB causing the sepsis should be achieved for the appropriate treatments, since the mortality rate from sepsis would be increased by 7.6% per hour if the treatment is delayed [10].

Additionally, the incorrect prescription, including overuse and misuse of broad-spectrum antibiotics in hospitals, is significantly accelerating the evolution of ARB to further reduce the effectiveness and reliability of antibiotic treatment for infectious patients [11]. Furthermore, developing new-generation antibiotics is still a challenge, as fewer pharmaceutical companies are engaged in the process of developing new antibiotics since the 1990s, resulting in a resistant development of bacteria outpacing human innovation [12]. The first list of antibiotic-resistant “priority pathogens” was announced by the World Health Organization (WHO), to particularly highlight ARB have built-in abilities to disable the antibiotic treatments [13]. And these ARB can transmit the genetic material to other bacteria, leading to the generation of new ARB. Currently, antibiotic-resistant infections

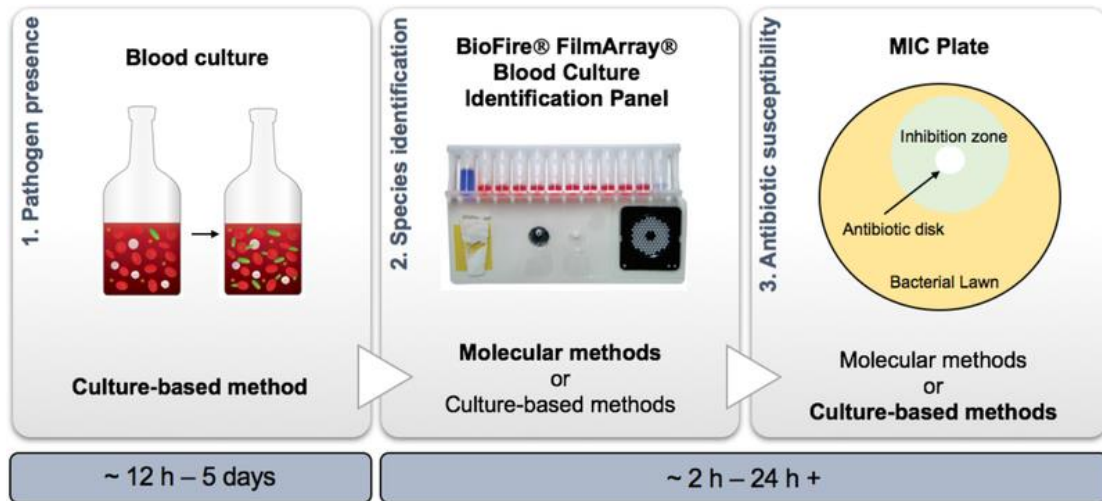


Figure 1.1 The overview of current diagnostic workflow for BSI, including 1) samples from patient blood (5 - 10 mL) cultured in nutrient rich media (25 mL) for the presence of a pathogen; 2) the identification of pathogens based on culture methods or molecular methods; 3) the determination of antibiotic susceptibility. Reprinted from [14].

approximately cause the death of 700,000 people each year worldwide. According to a projected analysis, the global mortality rate could reach at 10 million each year by 2050 and lead to economic loss of \$100 trillion annually if no actions are taken to restrict antibiotic-resistance infections or develop new-generation antibiotics [15]–[17]. To reduce the mortality rates for BSI and the economic burden on the healthcare system, the identification of those ARB at an early stage could help clinicians preserve the high efficacy of existing antibiotics for patients who urgently need them, meanwhile it could shortly guide clinicians to prescribe the appropriate antibiotics and avoid the application of broad-spectrum antibiotics [18], [19].

1.2 The Current Diagnostic Workflow for BSI

Currently, blood culture remains the gold standard diagnostic method for the detection of BSI [20]. As an example, the diagnostic workflow of sepsis, as displayed in **Figure 1.1**,

Table 1.1. Physical characteristics of main blood components regarding a sepsis-causing pathogen (*E.coli*) [14].

Components	Size (μm)	Concentration (cells/mL)	Density (g/mL)
Red blood cells (RBCs)	7.5 - 8.7 (diameter)	$3.7 - 5.8 \times 10^9$	1.086 - 1.122
White blood cells (WBCs)	7 - 20 (diameter)	$3.0 - 11.7 \times 10^6$	1.057 - 1.092
Platelets	1.5 - 3 (diameter)	$2.0 - 4.0 \times 10^8$	1.072 - 1.077
Plasma	-	-	1.024
<i>E. coli</i>	1 - 3 (length)	< 10	1.105

mainly consists of 1) pathogen presence by blood culture method, 2) species identification by molecular methods or culture-beads methods, 3) antibiotic susceptibility profiling.

Briefly, the blood culture involves the incubation of a patient's blood sample in a culture medium, which supports the growth of microorganisms. If pathogens are present in the bloodstream, they can proliferates within the culture medium, leading to visible signs of growth. It usually needs the time longer than 12 hours, up to 5 days, which depends on the growth rate of the specific pathogens causing the infection [21], [22]. After the presence of those pathogens through a blood culture, the specific identification and the characteristics of antibiotic susceptibility for pathogens are necessary to be proceeded, so that guiding the clinicians to most effectively treating sepsis infections. For instance, the traditional culture-based methods requires at least 24 hours for the identification process [23]. Despite the excellent sensitivity, the time to diagnose the infectious diseases is extremely long and it can only detect bacteria that readily grow under culture conditions [24], [25].

On the other hand, the anticipated emergence of molecular methods can enable the rapid species-level identification and characterization of antibiotic resistance for specific pathogens in a time period from 2 to 7.5 hours after the blood culture positivity [26], [27]. Therefore, this technical improvement could help clinicians to more rapidly determine the transition of therapy from a broad-spectrum antibiotic to a targeted antibiotic, leading to the more efficient treatment for sepsis in a time manner. However, the purification of target bacteria from whole blood still remains a pressing technical challenge, since whole blood is a complicated biological medium, as shown in **Table 1.1**, consisting of red blood cells (RBCs), white blood cells (WBCs), platelets, and other biological molecules [28]. It is noted that the largest challenge in purifying target bacteria from whole blood may be the extremely high concentration of RBCs, in which a single bacteria is heavily outnumbered due to a very low concentration of bacteria from the blood of patient in sepsis (1 - 100 CFU/mL in adults) [20]. On the other hand, some of these biological materials, such as platelets and proteins, may inhibit or interfere with the sensitivity of the molecular detection through light scattering and competitive binding or blocking [29], [30].

1.3 Microfluidic Platform as a Powerful Tool for Diagnosing BSI

1.3.1 Bacteria Separation from Blood

In the last decade, the field of microfluidics has gained significant attention as a promising technology for biomedical research and clinical diagnostics of bacteremia such as sepsis. Microfluidics enables the manipulation of either small volume or large volume of fluids, offering precise control over fluid flow and analysis. The inherent advantages of microfluidics, such as high throughput and compatibility with automation, make it an ideal

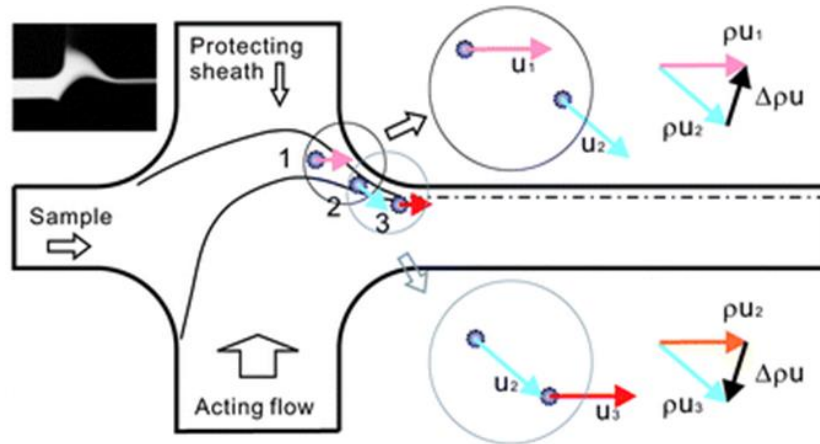


Figure 1.2 The schematic of microfluidic platform is based on soft inertial separation, presenting the curved and focused sample flow segment and the inertial force on fluid element. The image on top-left corner shows the curved and focused sample flow segment visualized by fluorescent dye. Reprinted from [31].

platform for addressing the challenges associated with simultaneous purification and detection of multiple bacterial targets.

There are several examples in the literature reporting the separation of target bacteria from blood samples, depending on the migration of RBCs and particle focusing. The microfluidic devices established well in these cases are combined with inertial force [32], [33], hydrodynamics [34], [35], electrophoresis [36], [37], or acoustics [38], [39], aiming to efficiently isolate and detect target bacteria from blood samples. For example, Wu *et al.* present the bacteria separation from dilute blood samples by changing the fluid and particle momentum [31], where the massive blood cells were deflected more than bacteria, so that selectively isolating and obtaining the bacteria (**Figure 1.2**). Although the good separation was successfully achieved in this study, the final dilution of blood samples was reported around 1:1000. Mach and Di Carlo reported a massively parallel filtering system, consisting of forty 2-stage channels to reach the high filtering rate of 8 mL/min (or of 1 μ L/min in a single channel, as exhibited in **Figure 1.3**), based on inertial lift forces to

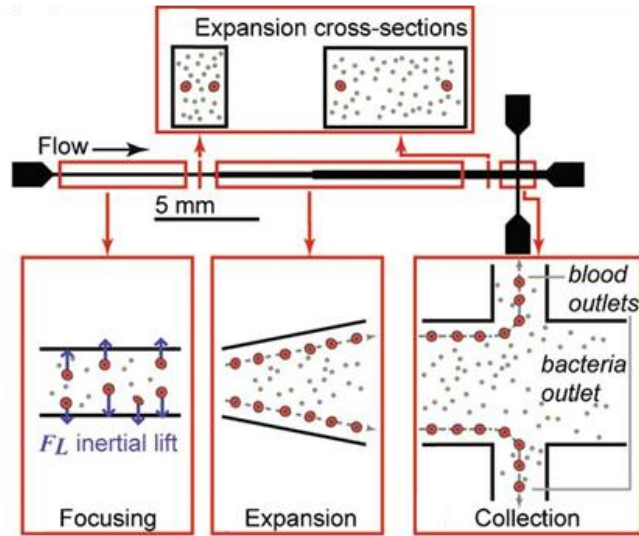


Figure 1.3 The proposed device showing inertial focusing amplification for particle separation with a straight channel design with one inlet and three outlets. The separation process includes the migration of large particles by inertial lift to equilibrium positions, RBC migration closer to the channel wall, and collection of RBCs at the side outlets and bacteria at the middle outlet. Reprinted from [40].

separate the target bacteria from dilute blood [40]. By removing about 88% of RBCs with losing some bacteria, the bacteria with a high concentration of 10^8 CFU/mL were separated from diluted blood, but with the recovery rate of 80%. However, these methods require the dilute blood samples with extremely large volumes (such as dilution rate with 1:200 and 1:1000), and the capacity of these devices could be limited by the applied flow rate per channel related to the rapid and effective separation under the inertial microfluidics. All these factors further result in a longer processing period of isolating target bacteria, potentially losing more bacteria during the microfluidic processing.

In the case of electrophoresis and acoustic approaches, Cheng *et al.* developed a new method to separate specific bacteria (*S. aureus* and *P. aeruginosa*) from blood cells dependent on arrays of quadruple electrodes [41]. Bacteria can be trapped at the center of electrodes while blood cells migrate away from the center. The captured bacteria can be

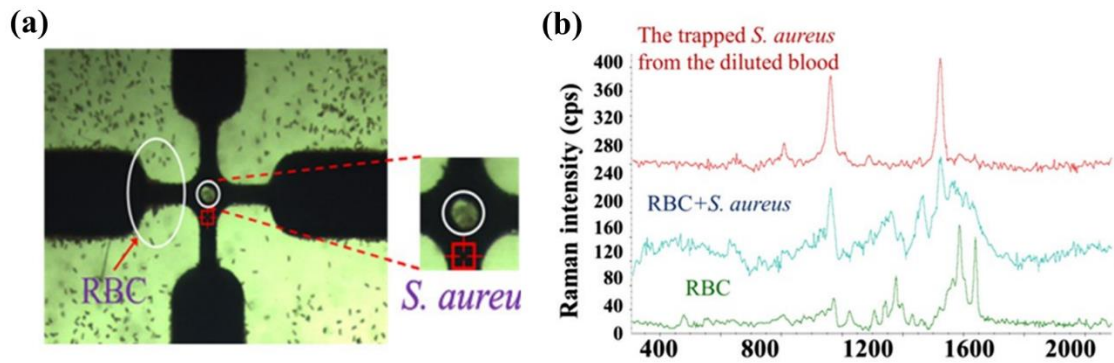


Figure 1.4 (a) Bacteria separation from RBC-bacteria mixture and the concentration of bacteria at the central area without RBC. (b) The SERS spectra of RBC, RBC-bacteria mixture, and the *S. aureus* dielectrokinetically separated from blood. Reprinted from [41].

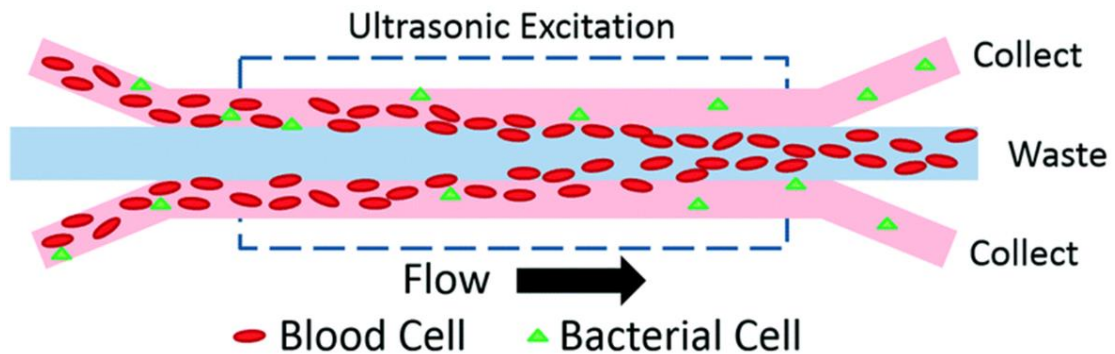


Figure 1.5 Illustration of acoustic separation of bacteria from blood. The mixture of bacteria and blood flows from the side inlets in laminar flow while a density-matched buffer flows in the center inlet. Acoustophoresis causes the blood cells (red and white blood cells) to migrate laterally toward the center of the channel and out the center outlet, while bacteria respond weakly to the acoustic field to the side outlets. Reprinted from [38].

identified by collecting gold nanoparticles with the bacteria at the center by using surface enhanced Raman spectroscopy, as displayed in **Figure 1.4**. However, this technique is challenged by the need of sufficient signal-to-noise for the detection, which corresponds to the diluted blood with a high concentration of target bacteria. Most recently, Dow *et al.* performed the purification of bacteria from blood via acoustophoresis in a plastic microfluidic chip, then detecting the target bacteria using engineered bacteriophage

luminescence assay that needs to be prepared over 48 hours [38], as shown in **Figure 1.5**. Their system can achieve a 40-60% yield of bacteria spiked into blood samples, meanwhile leading to red blood cell removal of 85-95%. However, all these approaches need either complicated design and fabrication or supplementary instruments to generate practical devices with high complexity, not enabling to be the excellent candidates for separating the sepsis-causing pathogens with low concentration from whole blood for point-of-care (POC) environments.

1.3.2 On-chip Detection Followed by Microfluidic Separation

Nowadays, the integration of on-chip pathogen detection techniques with microfluidic separation holds significant promise for sepsis diagnostics, potentially simplifying the current diagnostic workflow and reducing the time-to-diagnosis for rapid identification of sepsis-causing pathogens. This combined technique would shortly modulate the imperial treatment with the targeted therapy, further improving the outcomes of sepsis-infectious patients.

From the literature, only a few reports demonstrating the integration of enriched bacteria and on-chip detection platform. To the best of our knowledge, most research studies, which is over 85%, are unable to integrate the microfluidic separation of sepsis-causing pathogens with on-chip detection [14]. As would be impressive, Cooper *et al.* demonstrated a strategy for efficiently isolating target bacteria (*C. albicans* fungal cells) through microfluidic channels, captured by immunomagnetic beads coated with mannose binding lectin (MBL) [42]. Afterwards, the on-chip optimized approach was applied to optically identify the isolated beads and bacteria on a homogenous layer within the microchannel. In their study, a 98% of the fungal pathogens were separated

from the initial blood samples with the concentration of 10-100 cells/mL [42]. However, the limitation of optically detecting the captured pathogens is still existing, due to the high ratio (1000:1) of mixing the functional magnetic beads with pathogens, so that only achieving the detection of 67% in 1:1 diluted blood sample and of 68% in saline. Alternatively, Cai *et al.* creatively produced a dielectrophoresis-coupled microfluidic device equipped with on-chip PCR array for multiplexing detections of target bacteria (*E. coli*). The high-concentration bacteria spiked into diluted blood were tested, finally leading to the capture efficiency of 70.9% (1:10 diluted blood) and 91.5% (1:100 diluted blood), respectively [43]. Using dielectrophoresis for the separation process, the captured bacteria were subsequently mixed with the PCR reagents pre-loaded in the device. Followed by *in situ* thermocycling, the identification of target bacteria was proceeded by a fluorescent readout [43].

While the studies mentioned above can successfully isolate target bacteria from diluted blood samples, Cooper *et al.* offered an optical detection with the critical limitation of highly dense pile of beads and Cai *et al.* was not testing the low-concentration sample by their on-chip PCR detection system, so that not enabling an efficient and direct identification of sepsis-causing pathogen under the condition of extremely low concentration (1 - 100 CFU/mL in adults) [20].

1.3.3 Downstream (off-chip) Analysis for Detecting Target Bacteria

On the other hand, although many other investigations can successfully separate the target bacteria from blood, in those cases, the off-chip imaging process or characterization, such as microscope technologies [44] and molecular methods [45], still are required for quantitatively identifying the target bacteria.

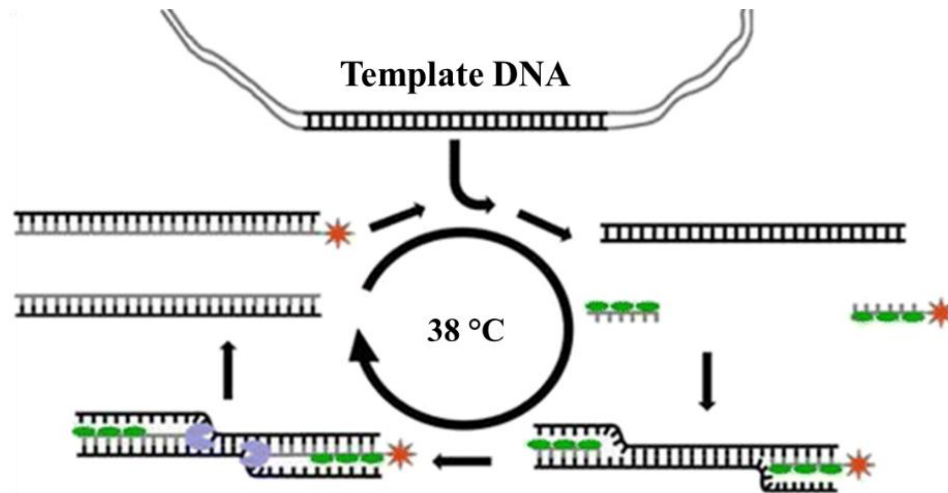


Figure 1.6 The schematic of labeling RPA in solution as a molecular detection technique: two oligonucleotide primers form a complex with a recombinase (green ovals) and are directed to homologous sequences on the target sequence where they can invade the DNA double strand. The polymerase (blue) elongates the strand for the duplication. RPA runs continuously at 38 °C. A labeling of amplification product is achieved by using a reverse primer coupled with a Cy5 reporter dye (red). Reprinted from [46].

Molecular diagnostic technology has been widely used for bacteria identification due to their numerous advantages over traditional methods [47], [48], such as high accuracy and specificity, for targeting the specific genetic marker or DNA sequences unique to the bacteria of interest. Moreover, the processing time based on molecular methods can be optimized within several hours, compared with the culture-based methods.

During recent years, the rapid development of biotechnology has attracted more attentions of researchers for faster and more accurate detection of pathogenic bacteria. For instance, polymerase chain reaction (PCR), which is amplification-based nucleic acid tests (NAT)[49], can exhibit the superior performance for detecting about 10 types of bacteria down to 10 CFU/mL from patient blood samples within four hours [50]–[52]. However, this technique requires the complicated and accurate thermocycles to

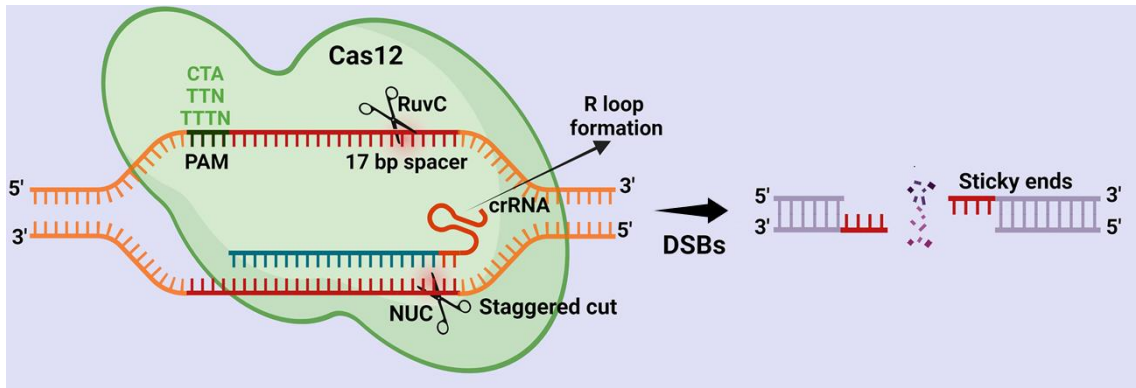


Figure 1.7 Schematic illustration of CRISPR/Cas12 mechanism. The Cas12 protein only needs CRISPR-RNA (crRNA) to create double-stranded breaks (DSBs). Cas12 protein cleaves the target region beside an adjacent protospacer motif (PAM) sequence (CTA, TTN, TTTN) with the help of the RuvC and nuclease lobe (NUC) domains. Once Cas12 is active, R-loop can be initiated, which forms base-pair (bp) hybridization between the crRNA and the target DNA strand. During this step, Cas12 matches the < 17 bp of the target sequence and leads to an R-loop formation. Once R-loop is formed, the Cas12 protein uses its active RuvC domain and generates a staggered cut in the non-target strand with the help of the PAM sequence. (RuvC stands for an *E. coli* protein involved in DNA repair). Reprinted from [53].

rapidly shuttle the temperature between 95 °C and 50 °C, as well as skilled technicians to operate the tests [54]. To address these drawbacks, the isothermal amplification technique has been developed to be more remarkable in its simplicity, multiplexing capacity, and extremely rapid amplification. For example, recombinase polymerase amplification (RPA) could be an excellent candidate, as a molecular detection method as shown in **Figure 1.6**, to run at a constant and low temperature of 37 °C - 42 °C, which is the optimal temperature for the process of amplifying target DNAs or RNAs [55]. Especially, even the body temperature can also activate the amplification process as needed [56], and the limit of detection can be reached to detect as low as 10 copies of genomic DNA of methicillin-resistant *Staphylococcus Aureus* (MRSA) sample, under the processing time of 30 mins [57]. These features make it suitable for the source-limited setting or remote area for pathogen detection.

On the other hand, CRISPR-Cas (clustered regularly interspaced short palindromic repeats and CRISPR-associated proteins) system is a revolutionary gene editing technology in recent years [58]–[63]. CRISPR are regions of DNA sequences found in the genomes of bacteria and other microorganisms [64], and Cas are enzymes that work together with CRISPR to facilitate DNA editing. CRISPR-Cas12 technique, as shown in **Figure 1.7**, has drawn more and more attention to highly specific and rapid diagnostics of bacterial targets [65], [66]. Once recognizing the DNA targets, Cas nucleases are activated to indiscriminately cleave non-desired single-stranded nucleic acid molecules, which has been widely applied to detect the specific DNA by nonspecifically degrading a reporter DNA [67], [68]. Particularly, CRISPR-Cas method characterized with specific binding activity and high cleavage has been developed to rapidly and precisely detect various target bacteria (e.g., *Escherichia coli* and Methicillin-resistant *Staphylococcus aureus*), by combining with other detection techniques such as fluorescence-based reading [69], [70] and electrochemistry workstations [71], [72].

Therefore, integrating CRISPR-Cas system with RPA, could be potentially a versatile platform of a relatively rapid, specific, and highly sensitive detection technology, leading to the molecular identification of sepsis-causing pathogens.

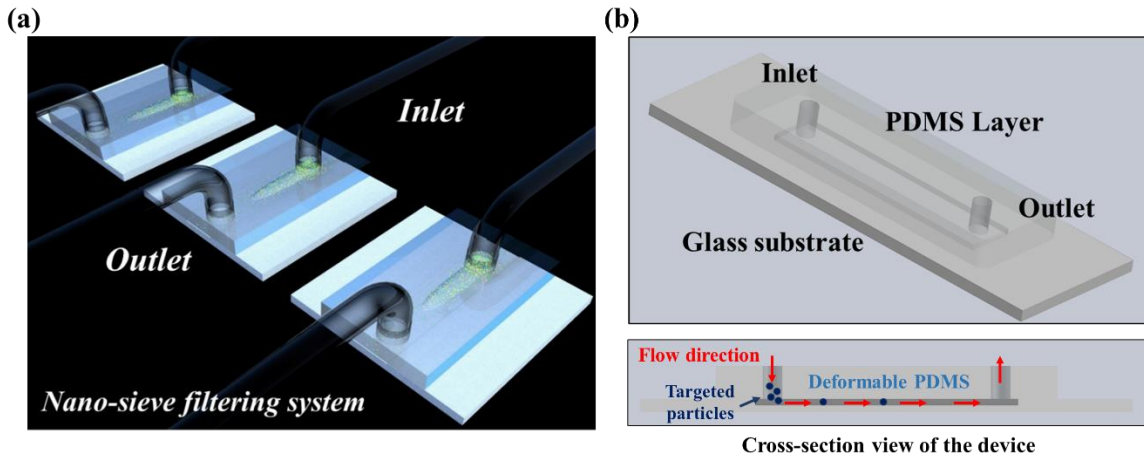


Figure 1.8 The designed device based on deformable microfluidics. (a) The schematic presenting a proposed “nano-sieve” filtering system based on hydrodynamic deformation of PDMS roof. (b) The device modeled by Solidworks consists of a PDMS layer on the top and a glass substrate on the bottom. Blue dots mean the applied particles pumped into the channel, then trapped by the deformable PDMS roof. Red arrows present the flow direction.

1.4 Motivation and Objectives of This Study

1.4.1 Motivation

The diagnosis of sepsis is still extremely challenging as the isolation of low concentration pathogens from bodily fluids such as whole blood is difficult, and typically relies on time-consuming and complicated isolation processes. In this study, the aim is to explore the potential of microfluidics as a powerful tool for rapid purification of ARB from whole blood samples. The unique features of microfluidic devices, such as miniaturization and integration of multiple functionalities, would provide a microfluidic platform for a rapid and efficient isolation and characterization of bacteria from complex biological matrices, such as human whole blood. Regarding the detection of those ARB after purification, the integration of CRISPR-Cas system

with RPA could offer a fast, specific, and sensitive identification of purified target bacteria obtained from a functional microfluidic platform, so that achieving a fast and efficient purification and detection of ARB from whole blood for early diagnosis and treatment of sepsis.

1.4.2 Objectives of This Study

In this study, a novel and deformable microfluidic device, named nano-sieve, was proposed here (**Figure 1.8**), which could be further optimized for efficient and rapid purification of target bacteria from whole blood, integrated with the detection technology based on molecular methods (e.g., RPA/CRISPR-Cas system) for accurate identification of sepsis-causing pathogens. Several objectives are stated as below:

Objective #1

The idea of designing a microfluidic-based platform with a deformable microchannel is proposed. The theoretical model is established to investigate the capture efficiency in terms of channel depth and microparticle size, respectively, during the microparticle trapping process. On the other hand, the practical device is designed and fabricated to study the fundamental mechanism of dynamic microfluidics, by introducing rigid particles and soft cells into the nano-sieve channel. The trapping efficiency can be subsequently evaluated by investigating the amounts of microparticles captured by nano-sieve and the one collected through the waste outlet. This established model is also discussed for further optimizing the microfluidics of nano-sieve, offering a guidance to potentially trap the target bacteria.

Objective #2

The established nano-sieve device is subsequently optimized by collaborating with a three-dimensional (3-D) magnetic beads-assistant microstructure within the microfluidic channel for efficiently trapping, retrieving, and concentrating *Escherichia coli* (*E. coli*) from bacteria suspension in PBS and blood plasma. The stained *E.coli* bacteria are applied to evaluate the capability of this new filtering system under various flow rates given by the syringe pump. Additionally, the technology of computational fluid dynamics (CFD) and 3-D optical tomography are employed to explore the construction of stacked beads within the deformed nano-sieve channel, aiming to understand the mechanism of deformable microfluidics during the bacteria separation process.

Objective #3

The target bacteria could be isolated and purified from bacteria-spiked whole blood. Firstly, only 10 μm magnetic beads are chosen to form 3-D microstructure for filtering red blood cells (RBCs), as RBCs make up about 45% of blood that should be filtered out from blood samples to prevent the clogging issue. It is supposed that bacteria with much smaller size than RBCs can pass through the voids between 10 μm beads. To achieve this goal, the microbead-packed deformable microfluidic system was tested for efficiently separating RBCs and obtaining highly purified plasma from whole blood, as well as retrieving captured blood cells from the device. Additionally, a highly accurate model is constructed to help understand the relationship between the mechanical properties of the microfluidics, flow rate, and microbeads packing/leaking based on the

microscope imaging and the optical coherence tomography (OCT) scanning. These all investigations is aiming to develop a reliable beads-stacked nano-sieve device for efficiently purifying and concentrating the target bacteria from whole blood.

Objective #4

The nano-sieve device is further developed by adding the pneumatic layer, to better secure the beads stackings for a robust process of purifying bacteria from the initial samples. In addition, it is found that an immunomagnetic assay can be employed for a fast and effective separation of blood cells from whole blood, while not reacting with target bacteria. In this study, the microfluidic motion inside this developed nano-sieve device is also investigated by computational fluid dynamics (CFD) and operational experiments, enabling the reliable beads stacking and efficient capture of target bacteria under a higher flow rate. The purified and concentrated bacteria from blood samples, with the employment of an optimized multiplexing filtering process via the pneumatically-regulated nano-sieve device, were specifically identified by RPA-CRISPR/Cas assay. Importantly, a rapid, sensitive, and specific detection can be visually achieved when dealing with a low-concentration bacteria (e.g., MRSA) blood sample, potentially leading to the application of on-chip detection for sepsis diagnosis.

Chapter 2. Theoretical Model on Microparticle Trapping and Releasing in a Deformable Nano-sieve Channel

*Part of the content in this Chapter reprinted with the permission from “Chen, X., Falzon, L., Zhang, J., Zhang, X., Wang, R.Q. and Du, K., 2019. Experimental and theoretical study on the microparticle trapping and release in a deformable nano-sieve channel. *Nanotechnology*, 31(5), p.05LT0.”*

This chapter demonstrates the fundamental principles of trapping and releasing microparticles by the deformable microfluidics, covering the physics and design aspects of a desired microfluidic device. A theoretical model was established, based on computational fluid dynamics (CFD), to reveal the capture efficiency as a function of the dimensions of channel and the size of microparticles in diameter. The various geometries and flow rates were applied to the designed nano-sieve device that reacted with microparticles, then comparing with the theoretical data to further optimize the next generation deformable microfluidics for the efficient microstructure manipulation.

2.1 Introduction

Deformable microfluidics is an emerging field within microfluidics that focuses on the development and utilization of microfluidic devices with deformable elements. These deformable elements, such as flexible membranes, hydrogels, or elastomers, allow for dynamic control and manipulation of fluid flow, sample handling, and device functionality [73]–[75]. By integrating the principles of microfluidics with deformable materials, researchers have been able to create innovative platforms with enhanced capabilities and unique functionalities.

Theoretical models play a critical role in understanding and predicting the behavior of deformable micro-/nano-fluidic systems. These models could provide a framework for analyzing the fluid flow, deformation, and mechanical properties of the deformable elements within the micro-/nano-fluidic device. They offer valuable insights into the underlying physics and mechanics governing the system's behavior, enabling the design, optimization, and customization of deformable micro-/nano-fluidic devices for specific applications.

The lack of a theoretical model for investigating the capture efficiency of a deformable microfluidics could result in significant particle loss and reduced performance within a practical device, such as the nano-sieve device proposed in this study, ultimately limiting the widespread application of deformable micro-/nano-fluidics. First, even though hydrodynamically induced fluid–solid deformation in shallow microfluidic systems has been reported before, no size-selective sieves have been previously designed to take advantage of the continually varying deformation pattern. Second, to maximize the flow rate for rapid processing of a large sample volume, a deformable microchannel with an

extremely low aspect-ratio (height/width) is often preferred. These types of microchannels or nanochannels with increased widths usually suffer from significant deformation patterns and fail to maintain their trapping efficiency owing to unexpected particle losses. These two problems require us to build a theoretical model to explore the complicated fluid–structure interaction and control undesired deformations. Moreover, a reliable model can guide designers to achieve the required deformation for particle size-selective trapping.

Therefore, in this study, we first introduced a high-flow rate nano-sieve device with an extremely low aspect ratio of 1:2000 for size-selective microparticle trapping and established a theoretical model based on a fluorescence detection of the microparticles to evaluate the design of deformable nano-sieve device with potential applications in optical waveguide [76], size-based filtration [77], and biomedical imaging [78].

2.2 Material and Methods

Polydimethylsiloxane (PDMS, SYLGARD™ 184) was purchased from Ellsworth Adhesives, WI, USA. The fluorescent microspheres with the diameter of 5 μm were obtained from Thermo Fisher Scientific, MA, USA. The glass wafer (D263, 550 μm in thickness, double side polished) were received from University Wafer, MA, USA.

2.2.1 Fabrication of nano-sieve device

Briefly, a 1 μm thick silicon oxide was deposited on the surface of cleaned glass wafer via chemical vapor deposition (AME P5000), then a positive photoresist (PR) layer was spin-coated on top. Followed by standard photolithography for transferring the channel pattern (2 mm \times 8 mm) onto the PR layer, silicon oxide was wet-etched by

buffered oxide etching (BOE) with the etching rate of 163 nm/min to create the nano-sieve channel. The mixture of BOE solution consists of 49% hydrofluoric acid (HF) and 40% ammonium fluoride (NH₄F). After stripping the PR layer by soaking in acetone solution, the nano-sieve channel was ready for binding with PDMS block, which was mixed with the base and the curing agent at a ratio of 10:1. A 5 mm thick PDMS block was cured in the oven at 85 °C overnight, the inlet and outlet were opened by using a biopsy punch (1 mm in diameter). Finally, the PDMS was bonded onto the glass substrate by applying corona treater (Electro-Technic Products) with a baking process at 100 °C for 2 hours.

2.2.2 *Microparticles trapping process*

The fluorescent particles at 5 μm in diameter were prepared in DI water with the desired concentration of $\sim 9 \times 10^6$ particles/mL. Those particles were pumped into the channel by a syringe pump under various flow rates from 20 μL/min to 120 μL/min. The waste liquid was collected from the outlet of channel for further fluorescent measurement.

2.2.3 *Spectrofluorometric Characterization*

The fluorescent intensity of initial solution (5 μm particles, 100 μL) was measured by using a JASCO FP-8500 spectrofluorometer with the excitation wavelength of 480 nm. The raw data was then exported and replotted for the quantitative analysis, so that evaluating the capture efficiency by comparing the intensity peaks between initial solution and waste solution.

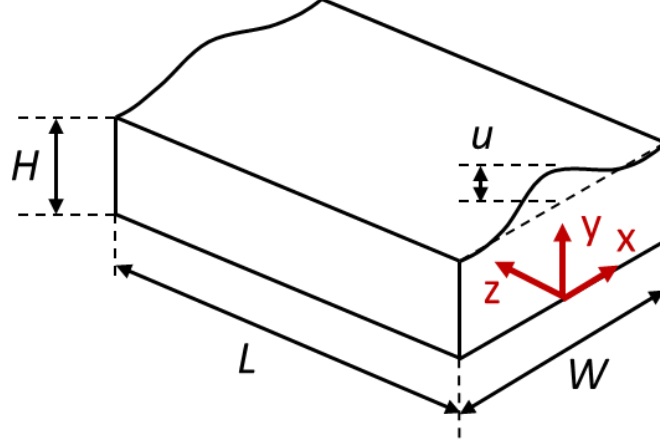


Figure 2.1 The schematic of deformable microchannel with a compliant cover, where H is the initial height of microchannel, L is the length of microchannel, and W is the width of microchannel. u is the deformation of the top roof. Reprinted from [79].

2.3 Results and Discussion

To explore the fundamental principles of trapping and releasing microparticles by the deformable microfluidics, our theoretical model was first proposed and created dependent on the fluid-structure interaction problem with a Stokes flow in a microchannel finished with a compliant cover (**Figure 2.1**). The streamwise velocity can be obtained using classical theory, i.e.

$$v_z = \frac{1}{2\mu} \frac{\partial p}{\partial z} (H + u - y)y. \quad (2.1)$$

where p is the pressure, μ is the dynamic viscosity, and v_z is the flow velocity along the channel, H is the original depth of the channel, and u is the deformation height of the top roof. The flow rate Q can be found by integrating **Eq. 2.1**,

$$Q = \int_{-\frac{W}{2}}^{\frac{W}{2}} \int_0^{H+u} v_z dy dx = -\frac{1}{12\mu} \frac{dP}{dz} \int_{-\frac{W}{2}}^{\frac{W}{2}} (H + u)^3 dx. \quad (2.2)$$

Due to the pressure gradient inside the channel, the PDMS cover curves upward and forms a slope from the inlet toward the outlet. The deformation of the top roof can be described by the Kirchhoff–Love equation for isotropic quasi-static bending of a plate under a transverse load due to the fluid pressure, with the assumption that channel length is much greater than the width,

$$u(x, z) = \frac{p(z)}{24B} \left(x + \frac{W}{2}\right)^2 \left(x - \frac{W}{2}\right)^2 \quad (2.3)$$

where $B = \frac{Et^3}{12(1-\nu^2)}$ is the bending energy, E is the Young's modulus and $\nu = 0.5$ is the Poisson ratio of the material (PDMS), W is the channel width.

Inserting **Eq 2.3** into **Eq 2.2**, we can solve the equation for p to the leading order, assuming the top roof is stiff,

$$p(z) = \frac{24BH}{W^4} \left(\sqrt{\left(\frac{W^4 p_0}{24BH} + 10\right)^2 + \frac{10\mu W^3 Q}{BH^4} (L - z)} - 10 \right) \quad (2.4)$$

The outlet has a pressure drop due to the geometry and a connecting tube, so we used an empirical model similar to Darcy-Weisbach equation to quantify,

$$p_0 = C \cdot \frac{\mu Q}{D^4}. \quad (2.5)$$

If $p_0 = 0$, the present derivation becomes the same as the theoretical model developed by Christov *et al.* [80], which has been verified with experiments. To calibrate the model, we estimate the area that the particles can enter, which can be obtained by letting

$$u + H = d, \quad (2.6)$$

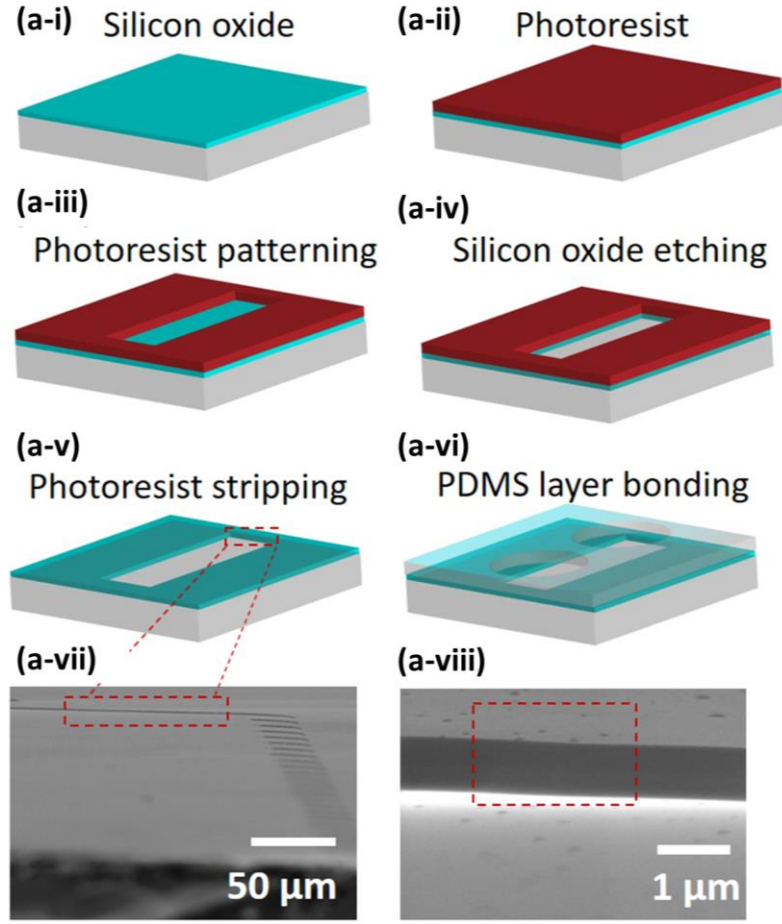


Figure 2.2 The fabrication process of a single channel for nano-sieve device. The SEM image with low-magnification and high-magnification to confirm the final height of microchannel. Reprinted from [79].

where d is the particle diameter. So the area that allows particle to enter is bounded by $x = x_c(z)$, which can be expressed as

$$x_c = \begin{cases} \pm W \left[\frac{1}{4} - \left(\frac{d}{H} - 1 \right)^{1/2} \left(\sqrt{\left(\frac{W^4 p_0}{24BH} + 10 \right)^2 + \frac{10\mu W^3 Q}{BH^4} (L - z)} - 10 \right)^{-1/2} \right]^{1/2} & (Q > Q_c) \\ 0 & (Q < Q_c) \end{cases} \quad (2.7)$$

To determine the constant C in **Eq 2.5**, a practical microchannel was then fabricated (as shown in **Figure 2.2**) and tested by using the 5 μm fluorescent microparticles that were

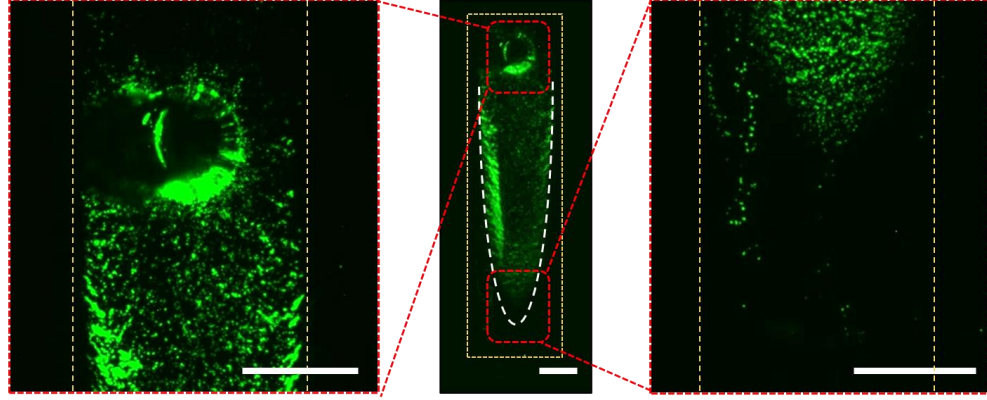


Figure 2.3 The experimental deposition of particles within the microchannel. *Left*: a high-magnification image showing the highly-concentrated particles around the inlet. *Middle*: the entire profile of deposited particles within the fabricated microchannel. *Right*: a high-magnification image showing the concentrated particles close to the outlet. The dashed light-gold lines present the edges of channel. The white dashed-parabolic line means the predicted particle distribution of the developed theoretical model. Scale bar: 1 mm. Reprinted from [79].

pumped into the channel. **Eq 2.7** was plotted in **Figure 2.3** with white dashed-parabolic line. The value of C was determined to be 2.1×10^5 . As shown in the **Figure 2.3**, the shape of the theoretical prediction closely matches the fluorescent particle area, thus indicating that our theoretical model can accurately predict particle trapping in the experimental observations. The transportation and trapping of particles inside the channel are a complicated process and is difficult to model. To fully understand this complicated system, high-resolution computational fluid dynamics is required [81]–[83]. Herein, a generalized semi-empirical model was developed. We first classify the flow into two types: filtered and escaping flows. The filtered flow indicates that the particles carried in the flow have been trapped in the nano-sieve and that no particles are contained. The escaping flow exits the nano-sieve without filtration, allowing the contained particles to escape. The escaping flow rate can be estimated by integration

$$\begin{aligned}
Q_{escape} &= \int_{-x_c(L)}^{x_c(L)} \int_0^{H+u} v_z(L) dy dx = \frac{25Q}{12WH^3(\beta+10)} \int_{-x_c(L)}^{x_c(L)} (H+u(L))^3 dx \\
&= \frac{25Q}{12(\beta+10)} \sum_{n=1}^7 C_n \left(\frac{x_c(L)}{W} \right)^{2n-1}
\end{aligned} \tag{2.8}$$

The trapping efficiency is estimated by

$$\eta = 1 - \varepsilon \frac{Q_{leak}}{Q} = 1 - \varepsilon \frac{\sum_{n=1}^7 C_n \left(\frac{x_c(L)}{W} \right)^{2n-1}}{\sum_{n=1}^7 C_n \left(\frac{1}{2} \right)^{2n-1}} \tag{2.9}$$

where the coefficient ε is used to quantify the effect that particles can be trapped at the inlet and the inaccuracy of the flow classification, and

$$C_1 = \frac{(\beta+16)^3}{2048}, \tag{2.10}$$

$$C_2 = -\frac{\beta(\beta+16)^2}{256}, \tag{2.11}$$

$$C_3 = \frac{3\beta(5\beta^2+96\beta+256)}{640}, \tag{2.12}$$

$$C_4 = -\frac{\beta^2(5\beta+48)}{56}, \tag{2.13}$$

$$C_5 = \frac{\beta^2(5\beta+16)}{24}, \tag{2.14}$$

$$C_6 = -\frac{3\beta^3}{11}, \tag{2.15}$$

$$C_7 = \frac{2\beta^3}{13}, \tag{2.16}$$

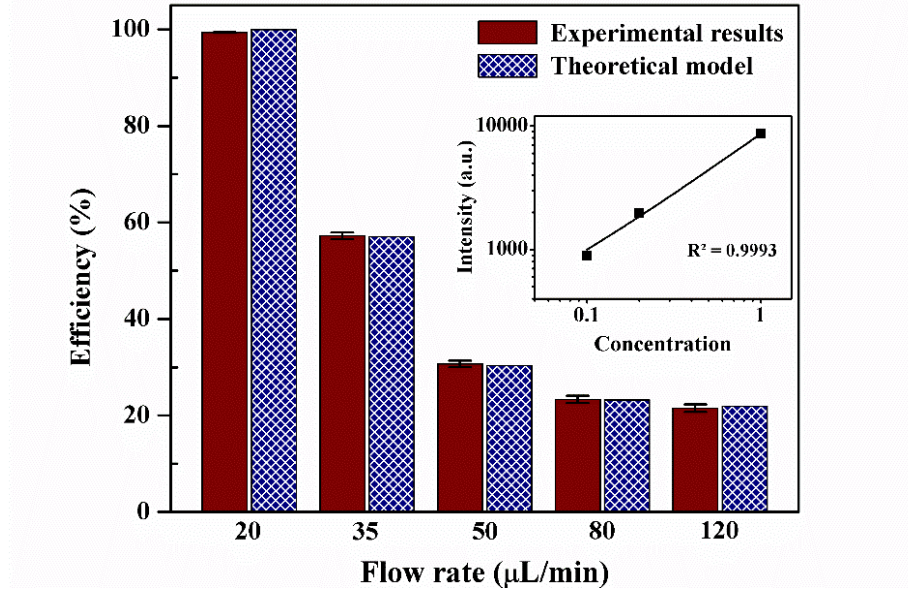


Figure 2.4 The capture efficiency of experimental results (solid red) and theoretical calculations (patterned blue) under various flow rates applied. Inset: the fluorescence intensity of serial dilution of the original microparticles solution that was applied for calculating the capture efficiency. Error bars are the standard deviation of the mean. Reprinted from [79].

$$\beta = \frac{c\mu QW^4}{24BHD^4} \quad (2.17)$$

To calculate the trapping efficiency, the fluorescence intensity of the serially diluted microparticle solution was measured with a spectrofluorometer, and the results are plotted in the inset of **Figure 2.4**. The fluorescence intensity of the supernatant collected from the nano-sieve was also measured. The trapping efficiency was then determined by subtracting the signal from the supernatant. As shown in **Figure 2.4** (solid red), the measured efficiency is 99% at 20 μL/min and drops to 58% at 35 μL/min, thus demonstrating 1) a substantial inflation of the PDMS layer along the transverse direction, and 2) microparticle release. The efficiency is further reduced to 21% under a flow rate of 120 μL/min. The calculated efficiency is 100% at 20 μL/min, 52% at 35 μL/min, and 20% at 120 μL/min (patterned blue), when $\varepsilon = 0.775$ is applied in **Eq 2.9**. The microparticle trapping efficiency

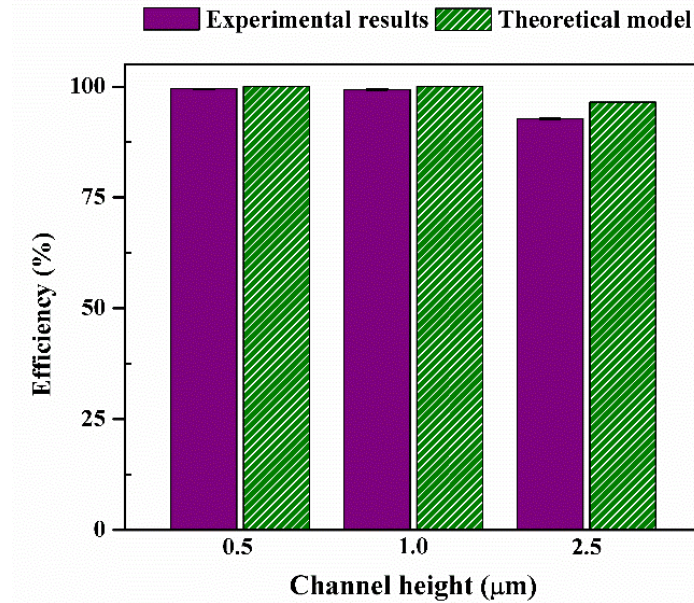


Figure 2.5 The capture efficiency of experimental results (purple) versus theoretical calculation with three different channel height. Error bars are the standard deviation of the mean. Reprinted from [79].

vs. nano-sieve channel height is shown in **Figure 2.5**. We tested nano-sieve devices with channel height ranging from 0.5-2.5 μm. At a flow rate of 20 μL/min, the measured capture efficiencies are 99% for 0.5 μm channel, 99% for 1 μm channel, and 93% for 2.5 μm channel, respectively. These agree with our theoretical prediction. Thus, our model based on a circular boundary can accurately predict the trapping efficiency of microparticles at various flow rates and channel heights.

With this highly accurate theoretical model, we can predict the trapping efficiency of the nano-sieve for a wide range of geometries. Based on the current design, we calculated the dependence on trapping efficiency when the initial slit height or particle diameters varied. **Figure 2.6(a)** shows that the trapping efficiency can be decreased at increasing flow rates and/or initial slit heights. Furthermore, the 100% trapping efficiency exhibits a

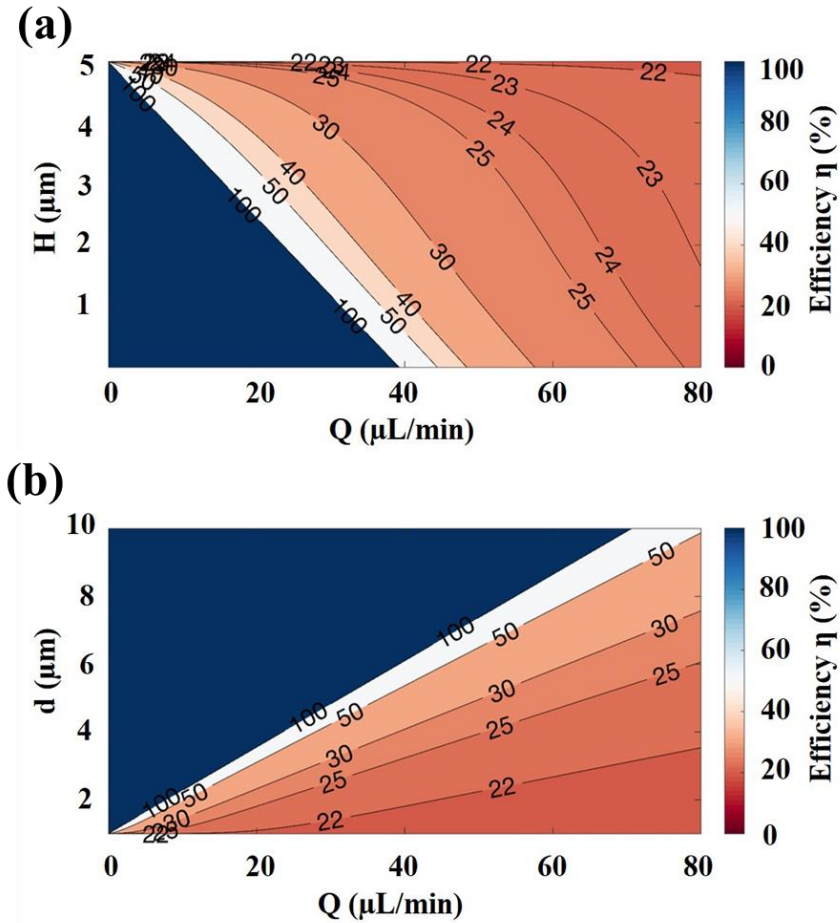


Figure 2.6 The calculated capture efficiency based on the developed theoretical model. (a) the channel height as a function of flow rates. (b) the particle size versus flow rates. Reprinted from [79].

straight-line boundary, with a maximum flow rate of $39 \mu\text{L}/\text{min}$ for 100% trapping efficiency. The trapping efficiency decreases more dramatically with the increased flow rate at a lower initial slit height. **Figure 2.6(b)** shows the trapping efficiency dependence on the particle size and flow rate. This shows that lower flow rates are required to capture smaller particles and that the trapping efficiency drops rapidly as a function of the flow rate. **Figure 2.6(b)** further indicates that if multi-size particles are injected into the device (poly-dispersion), particles with different sizes will have different trapping efficiencies

assuming that interactions between them can be ignored. This can be used to partially separate deposited particles moving into the device. The distribution of the trapping positions of different size particles will also differ. Future studies are required to verify whether nano-sieve device would be able to separate particles with closer discrepancy of dimensions.

2.4 Conclusion

In this study, the fluorescent microparticle trapping efficiency in a super shallow nano-sieve was experimentally measured to validate the theoretical model. To further optimize nano-sieve microfluidics, this established model was used to understand the channel deformation at different flow rates. As a result, the calculated capture efficiency was very closely matched to the experimental data. This robust model can successfully predict the trapping efficiency change at various flow rates and channel heights. We further developed general guidelines for next generation deformable microfluidics to isolate and release micro- and nano-particles with different channel heights and flow rates that can be extensively used for nanotechnology and biomedical engineering applications.

**Chapter 3. Experimental Study on Microparticles Trapping and Releasing
by a Robust Nano-sieve Device**

*Part of the content in this Chapter reprinted with the permission from “Korensky, G., **Chen, X.**, Bao, M., Miller, A., Lapizco - Encinas, B., Park, M. and Du, K., 2021. Single *Chlamydomonas reinhardtii* cell separation from bacterial cells and auto-fluorescence tracking with a nanosieve device. **Electrophoresis**, 42(1-2), pp.95-102.” and “**Chen, X.**, Falzon, L., Zhang, J., Zhang, X., Wang, R.Q. and Du, K., 2019. Experimental and theoretical study on the microparticle trapping and release in a deformable nano-sieve channel. **Nanotechnology**, 31(5), p.05LT01.”*

This chapter elucidates the optimized fabrication techniques and materials employed in microfluidic chip production, to generate an extremely high aspect ratio of 1:10,000 (height : width), along with the characterization methods for assessing the performance of nano-sieve device. This chapter also provides a discussion for the capability of nano-sieve device by evaluating the capture efficiency for the rigid microparticles and soft cells, under various flow rates. These experimental data could give a guidance to develop the nano-sieve filtering system for those desired targets.

3.1 Introduction

Deformable microfluidics have drawn considerable scientific interest in the recent past. The excellent tunability of deformable microfluidic devices can provide controllable capture, deposition, and target release. In the field of nanotechnology and biomedical engineering, the size-selective micro/nanoparticles separation and deposition are required by the specific particle size distributions [84], [85]. Currently, flow cytometry [86], electrophoresis [87], and remotely applied magnets [88] are commonly used for particle separation. but these approaches need complicated design and expensive external actuation. For instance, the separation of microparticles by electrophoresis needs the high alternating current voltage that can modify the physical and chemical properties of target particles [89], so that impacting the downstream analysis of those targets. The physical filtration with membrane is extensively employed to isolate the particles by size. However, this approach is difficult to be integrated with a planar and micro/nano device without the leakage, leading to the inefficient filtration. Additionally, the extraction of trapped particles from membrane is still a challenge for processing and imaging the downstream samples [90].

An emerging solution for efficient size-selective particle trapping and manipulation is the use of a deformable microfluidic chamber with a physical barrier. This design does not require complicated instruments to operate, and has been used for clog-free filtration of cancer cells [91], as a Stokes flow rectifier [92], and as an optofluidics sensing device [93]. Unlike a rigid microchannel, which can generate sealing and clogging issues, a deformable microchannel can be programmed to change the geometry for precise particle release and deposition [94].

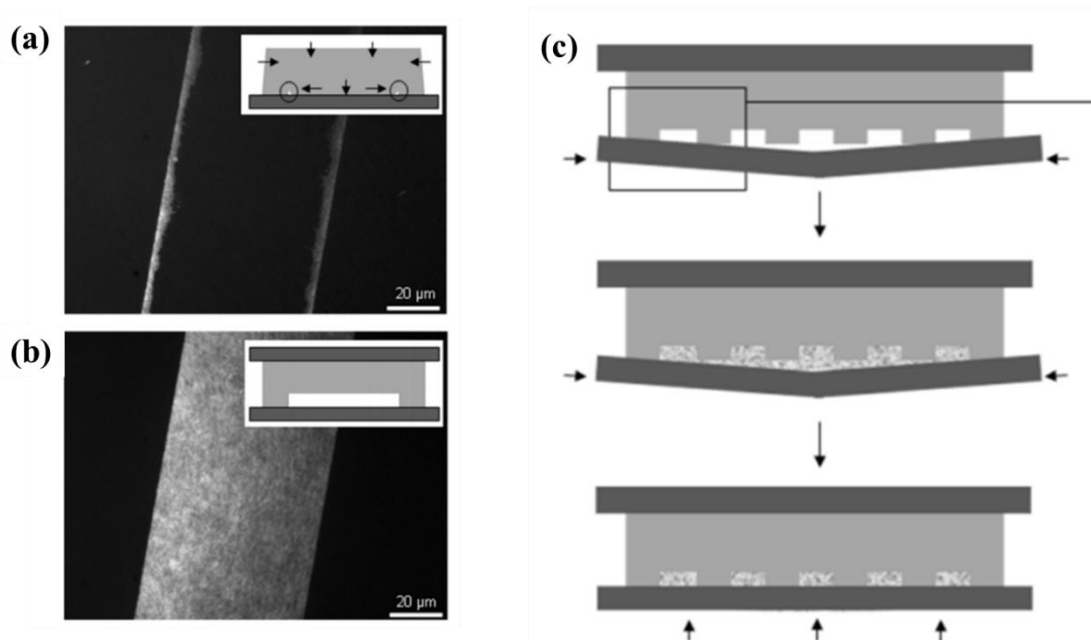


Figure 3.1 Illustration of two methods for collapse-free nanoslit. (a) without glass support on the side of PDMS, roof collapse occurs as shown in inset; (b) with glass support on the side of PDMS, the stable roof is achieved. (c) the method of wafer filling to successfully create the nanoslit channels. Reprinted from [95].

On the other hand, a rapid and robust fabrications of nano-slits or nanochannels using PDMS photolithography have recently generated great interest for single-cell genomic analysis [96] and individual bacteria trapping [97]. However, the fabrication of successfully creating nanostructures combined with PDMS still remains challenging due to the structural flexibility of PDMS and the surface adhesion energy. Lee, J. Y., *et al.* demonstrated two approaches to achieve the stabilization of PDMS nano-slits with a low aspect ratio (130 nm in height/100 μm in width) of 1:770 [95]. One method of glass support was applied by placing a glass slide on the other side of PDMS device during the bonding process (**Figure 3.1(a) and (b)**), which is effective to avoid roof collapse in the case of 340 nm × 60 μm nano-slit with the aspect ratio of 1:176; another method of water filling, as shown in **Figure 3.1(c)**, was used by slightly bending the glass substrate and filling the

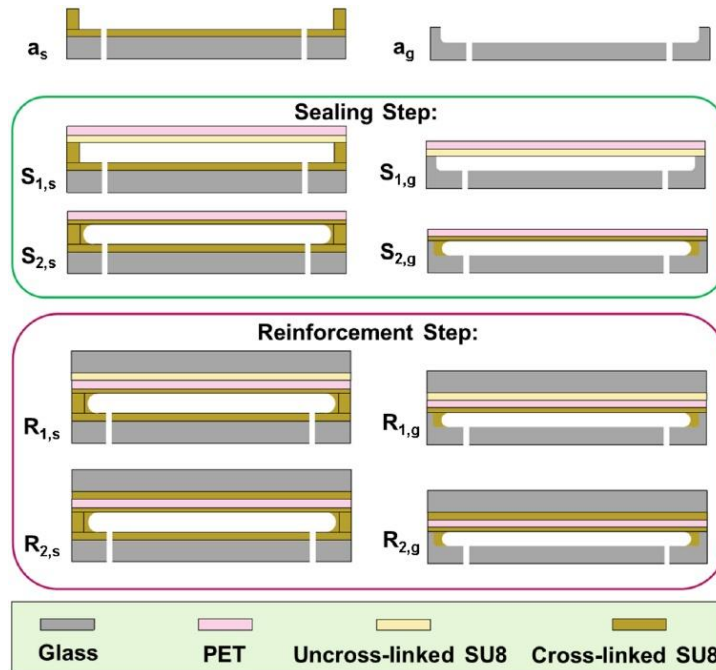


Figure 3.2 The fabrication flow of two-step sealing-and-reinforcement bonding paradigm for two different approaches that are used to create the SU-8 microchannel by photolithography (left) and the glass wet etching (right): the microchannel sidewalls are created through SU-8 photolithography (a_s) or glass wet etching (a_g). At the sealing step, a PET film coated with a thin layer of SU-8 seals the microchannel sidewalls ($S_{1,s}$ and $S_{1,g}$). The chip is then illuminated by UV light and post-exposure baking to cure the adhesive layer ($S_{2,s}$ and $S_{2,g}$). The slight SU-8 reflow can cause the round corners from the cross-sectional view. At the reinforcement step, a glass substrate coated with a SU-8 layer is attached to the bare side of the PET film ($R_{1,s}$ and $R_{1,g}$). The sample is then illuminated by UV light and post-exposure baking to cure the adhesive layer at the bonding interface of the reinforcement glass and the PET film ($R_{2,s}$ and $R_{2,g}$). Reprinted from [98].

water into the gap between PDMS and substrate, which achieve a robust bonding in the case of $100\ \mu\text{m} \times 130\ \text{nm} \times 100\ \mu\text{m}$ nano-slit with the aspect ratio of 770:1. However, these approaches are not effective for the case requiring the lower width/height ratio (maximum ratio of 770:1) and needs the more precise control during the process of plasma treatment, otherwise, the leakage may occur due to the weak bonding process. Additionally, Mehboudi, A. and Yeom, J. developed a new bonding strategy based on the application of low-temperature and low-pressure SU-8 bonding and a thin flexible film of polyethylene

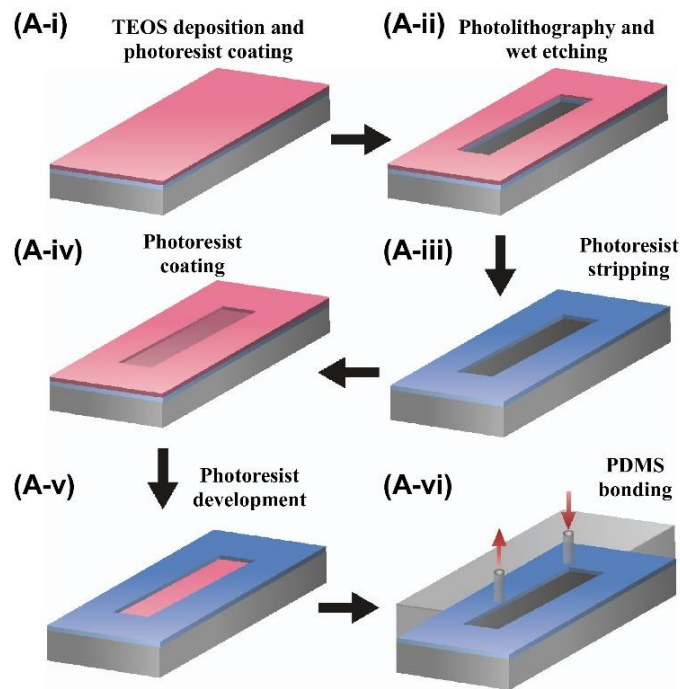


Figure 3.3 The fabrication process of nano-sieve device by using a dual photolithography. Reprinted from [99].

terephthalate (PET), to fabricate a microfluidic device for separating $3\ \mu\text{m}$ and $10\ \mu\text{m}$ particles, as shown in **Figure 3.2**. But the leaking issue could occur due to the defects of trapped air bubbles and small particles, thus leading to the failed separation of particles during the experiments [98].

In this chapter, it is noted that a one-dimensional nano-sieve device was successfully fabricated with an extremely low aspect ratio of 1:10,000 by introducing a sacrificial layer of positive photoresist (**Figure 3.3**), which was developed from the previous fabricated device with the ratio of 1:2,000 [79]. The size-selective capture and release of micro- and nano-particles were achieved by simply adjusting the flow rates. From the experiments, almost all the microparticles ($\sim 99\%$) were trapped in the nano-sieve device at a flow rate

of 20 $\mu\text{L}/\text{min}$. Increasing the flow rate induced a hydrodynamic deformation of the PDMS roof, leading to the loss of microparticles through the outlet. On the contrary, the nanoparticles were passing through the nano-sieve channel from the outlet, regardless of the applied flow rates. Additionally, soft cells, such as the mixture of microalgae and bacteria, were also introduced into nano-sieve channel to estimate the capture efficiency, potentially achieving the separation of cells by their size.

3.2 Material and methods

3.2.1 *Nano-device fabrication*

The nano-sieve device was fabricated on a glass substrate. Briefly, 200 nm of tetraethyl orthosilicate (TEOS) was deposited on a 6-inch glass wafer (University Wafer, Inc., MA, USA) by using Plasma Enhanced Chemical Vapor Deposition (AME P5000). First an adhesion promoter (hexamethyldisilazane, HMDS) was coated on the TEOS layer, followed by the spin coating of $\sim 1 \mu\text{m}$ thick positive photoresist (PR, AZ Mir™ 701) on the substrate. Then, soft bake was applied at 95 °C for 60 s, followed by standard photolithography patterning. After that, the wafer was baked at 100 °C for 60 s and developed by using CD-26 developer (Rohm and Haas Electronic Materials LLC, MA, USA) for 1 min. Buffered Oxide Etching (BOE) was used to etch TEOS layer with an etching rate of $\sim 163.2 \text{ nm}/\text{min}$. The sample was immersed into acetone for 1 min to completely remove the PR layer, followed by isopropyl alcohol (IPA) rinsing and cleaning for 15 - 20 s. Finally, the sample was dried by nitrogen gas. To avoid roof collapsing, a sacrificial PR layer ($\sim 1 \mu\text{m}$ in thickness) was patterned on the etched nano-sieve channel by standard photolithography. To seal the channel, Polydimethylsiloxane (PDMS, SYLGARD™ 184, Krayden Inc., CO, USA) base and

curing agent were mixed with a ratio of 10:1 and cast to a final thickness of ~3 mm. The PDMS layer was cured at 100 °C for 45 min. Inlet and outlet holes were created in the PDMS using a biopsy punch (Miltex Biopsy Punch, 1 mm in diameter). Eventually, the PDMS layer was permanently bonded on the glass substrate via oxygen plasma treatment (Electro-Technic Products Inc., IL, USA). Before on-chip experiments, acetone was injected into the nano-sieve channel under low pressure to dissolve the sacrificial PR layer within several seconds, followed by rinsing the entire channel with Deionized (DI) water.

3.2.2 Preparation of microparticles and nanoparticles

The fluorescent microparticles (diameter ~ 5 μm, concentration ~ 9×10^6 particles/mL (1:1), ~ 1.8×10^6 particles/mL (1:5), and ~ 9×10^5 particles/mL (1:10) and the fluorescent nanoparticles (diameter ~100 nm, concentration ~ 5.5×10^{11} particles/mL) were chosen for evaluating the capability of “nano-sieve” device for capturing and release particles. These particles were re-suspended in deionized (DI) water. Each 800 μL particles aliquot was introduced into the “nano-sieve” channel using a syringe pump (Harvard Apparatus) under a flow rate set from 20 - 120 μL/min.

3.2.1 E. coli culture and staining

Escherichia coli (*E. coli*, ATCC 25922) cells were cultured at 37 °C for 14-15 hours , until they achieved an optical density (OD) of 0.5-0.6 (absorption peak: 600 nm). This OD number corresponds to a concentration of ~ 1.71×10^8 cells/mL or ~ 6.3×10^7 CFU/mL. *E. coli* cells were then stained with fluorescent dye for imaging. Briefly, 1 mL of *E. coli* sample was centrifuged at 2000 g for 5 min. The supernatant was then replaced by fresh PBS buffer. We added 4 μL of the BacLight dye into PBS-based *E.*

coli solution, followed by vortexing for 10 - 15 s. The stained *E. coli* cells were incubated at room temperature for 20 min and centrifuged again for 5 min, followed by the depletion of the supernatant. Finally, the *E. coli* cells were re-suspended in 500 μ L PBS, ready for on-chip experiments.

3.2.2 *C. reinhardtii* cell culture

Bacteria-free *C. reinhardtii* cells and Chlamydomonas culture media were acquired from Carolina Biological Supply (Burlington, NC). The medium inoculated with *C. reinhardtii* cells was vortexed for 5 min to ensure uniform cell distribution. After that, *C. reinhardtii* cells were transferred to a separate vial which was previously sterilized with 100% ethanol and washed thoroughly with DI water. The *C. reinhardtii* cells were stored under a white fluorescent light (~ 40 W/cm²) at room temperature with the cap of the vial loosened to maintain air flow but avoid contamination.

3.2.3 *C. reinhardtii* cell trapping

We pumped 200 μ L of *C. reinhardtii* cells into the nano-sieve device by using a syringe pump (WPI SP220I) with a flow rate ranging from 4 - 8 μ L/min. The filtered supernatant was collected in an Eppendorf tube and the auto-fluorescence intensity was measured immediately using a Spectrofluorometer. The signal difference between the stock solution and the filtered supernatant was used to indicate the capture efficiency. The nano-sieve channel was also imaged under an Amscope XD-RFL microscope (Irvine, CA) at 4x magnification to determine the overall deposition profile of the *C. reinhardtii* cells. The concentrated area of the deposited *C. reinhardtii* cells was imaged at 40x magnification for a more useful local density comparison.

3.2.4 *Spectrofluorometric Characterization*

The fluorescent intensity of initial solution and waste solution from both 5 μm and 100 nm particles was measured by using a JASCO FP-8500 spectrofluorometer with the excitation wavelength of 480 nm. 300 μL of *C. reinhardtii* cells were transferred into a 1 mL Eppendorf tube and vortexed for 30 s to further distribute the cells throughout the media. Then, 100 μL of the cells from the tube were transferred to a cuvette and used JASCO FP-8500 Spectrofluorometer to check the fluorescence intensity of the stock solution. The raw data was then exported for plotting the quantitative chart, so that evaluating the capture efficiency by comparing the intensity peaks between initial solution and waste solution.

3.2.5 *SEM imaging*

The fabricated nano-sieve channel was imaged using a scanning electron microscopy (SEM, Tescan Mira3). A thin metal film (~ 5 nm) was coated on the surface of the sample by using an SPI-ModuleTM Sputter Coater. For high resolution imaging, the applied voltage was set at 20 kV.

3.3 Experimental results

In this study, a fabrication flow regarding the double-photolithography patterning, as shown in **Figure 3.3**, was applied to fabricate a nano-sieve channel, meanwhile eliminating the PDMS roof collapsing during the channel sealing process. The **Figure 3.4(a-i)** presents the channel coated by a PR layer of ~ 1 μm in thickness. And **Figure 3.4(a-ii)** shows the channel not coated by a specific PR layer, easily leading to PMDS collapsing after plasma treatment, which permanently causes the channel blocking. A successfully fabricated “nano-sieve” channel with 200 nm in thickness (**Figure 3.4(b)**) was used to study the

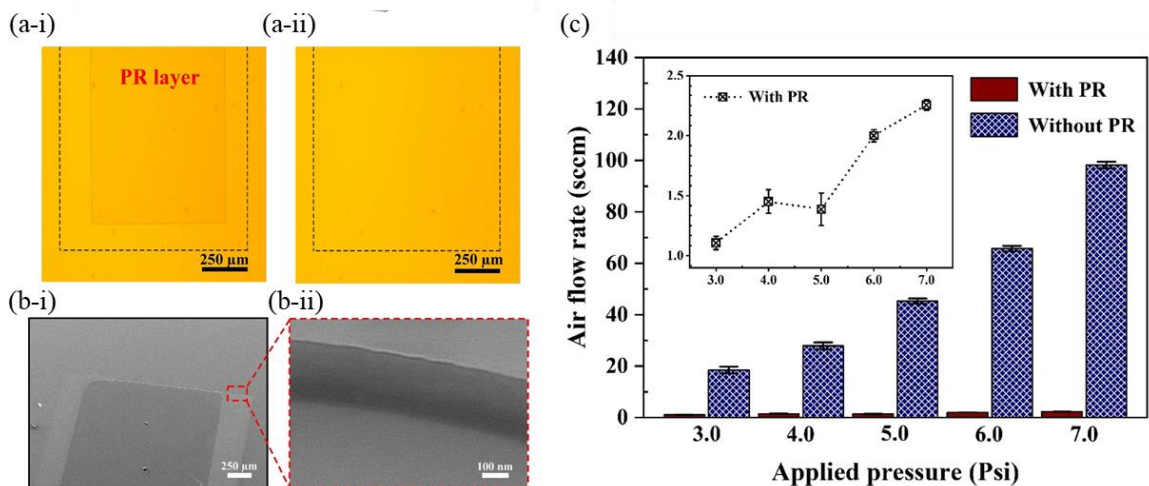


Figure 3.4 (a) Microscope images of the sacrificial PR layer before (a-i) and after (a-ii) the acetone washing. (b) SEM images display the sacrificial PR layer in the channel with low magnification (b-i) and the channel height with high magnification. (c) The measured air flow rate versus the applied pressure in the nano-sieve channel with (red bars) and without (blue patterned bars) PR layer. The inset shows more details of the measurement regarding air flow rate. Reprinted from [99].

microparticle trapping controlled by hydrodynamic deformation of PDMS roof. A pressure-controlled system integrated with air flow sensor was used to monitor the air fluxion in the “nano-sieve” channel with and without a sacrificial PR layer, respectively. As presented in **Figure 3.4(c)**, the applied air pressure was set from 3.0 to 7.0 Psi with the interval of 1.0 Psi. The air flow measurements were expressed by the unit of sccm (standard cubic centimeters per minute). The “nano-sieve” channel fabricated without PR shows the measured rate of air flow (blue patterned bar) ranged from ~20 to ~100 sccm. It is significantly higher than the rate of air flow (red bar) measured from the PR-patterned channel that exhibits an extremely low rate (only from ~ 1.1 to ~2.3 sccm). This data presents that the channel blocking caused by PDMS collapsing during channel sealing procedure can build up a very high flow resistance. Thus, the “nano-sieve” channel can be

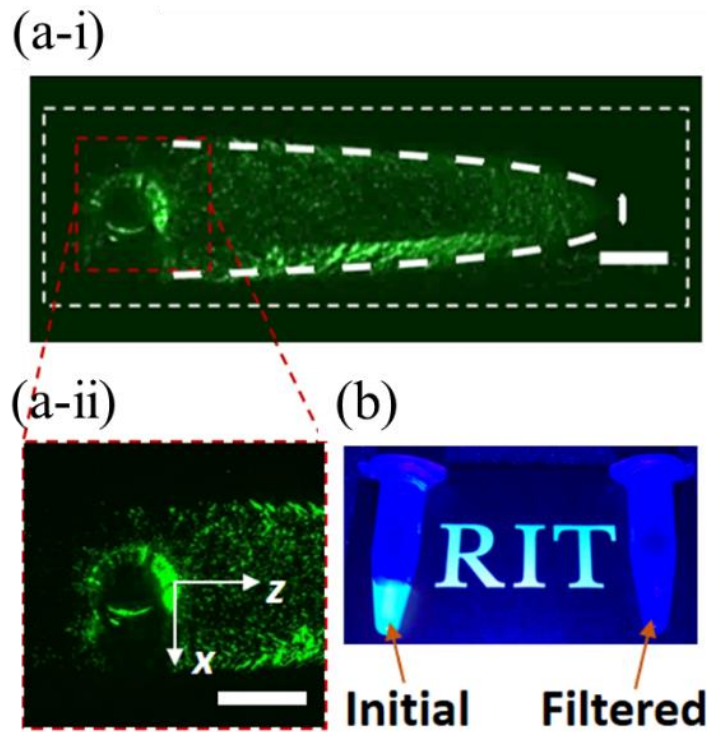


Figure 3.5 (a) Fluorescent particles trapped in the channel with a parabolic pattern (a-i) toward the outlet. The inlet area: highly-concentrated particles were deposited (a-ii). Scale bar: 1 mm. (b) Fluorescent particles solution before (*left*) and after (*after*) filtration. Reprinted from [79].

successfully fabricated by a double-photolithography patterning method for the testing of microfluidic hydrodynamics.

3.3.1 *Microparticles and nanoparticles trapping and releasing*

A series of experiments were performed to build and validate our fluid–solid deformation model. For example, fluorescent microparticles with the diameter of 5 μm and concentration $\sim 9 \times 10^6$ particles/mL were pumped into the micro- and nanofluidic device at various flow rates. Under a flow rate of 20 $\mu\text{L}/\text{min}$, $\sim 99\%$ of the microparticles are trapped within the device as shown in **Figure 3.5(a)**. Most microparticles are concentrated

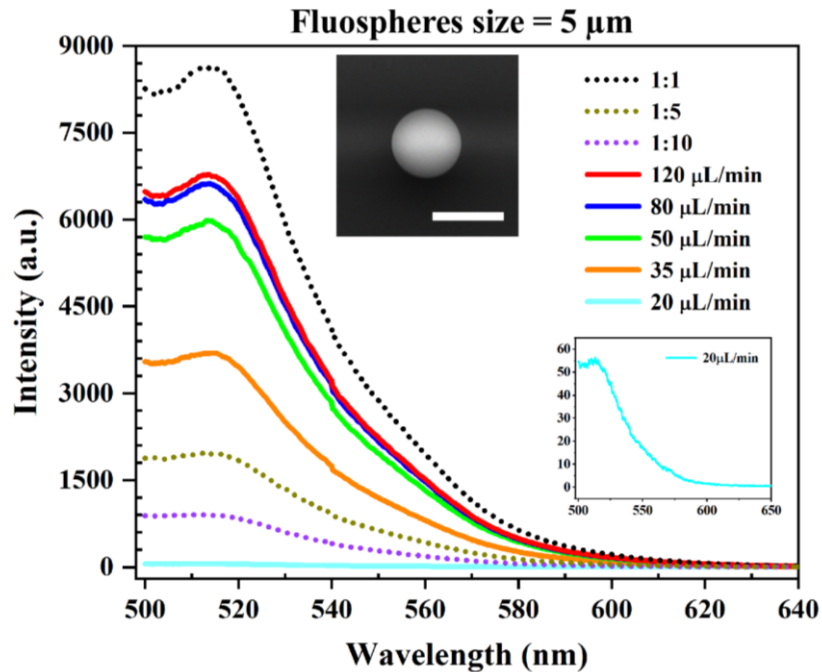


Figure 3.6 The measurement of fluorescent intensity from the filtered supernatant as a function of various flow rates. Inset: SEM image shows dried microparticles applied with the diameter of 5 μm (scale bar: 5 μm). Reprinted from [79].

at the inlet region of the nano-sieve (inset), and the migration of microparticles into the channel is observed due to the PDMS deformation and inertial forces. Before introduced into the device, the microparticles are suspended in deionized (DI) water, leading to uniform fluorescence emission (left), as illustrated in **Figure 3.5(b)**. However, the filtered supernatant changes to a transparent color (right), thus indicating the efficient trapping of microparticles by the device.

We measured the fluorescence intensity of 800 μL microparticles (diameter $\sim 5 \mu\text{m}$) with concentrations of 9×10^6 particles/mL (1:1), 1.8×10^6 particles/mL (1:5), and 9×10^5 particles/mL (1:10) by a JASCO FP-8500 spectrofluorometer at excitation peak of 480 nm. Each 800 μL microparticles aliquot (1:1) was pumped into the nano-sieve device using a syringe pump (Harvard Apparatus) with a flow rate ranging from 20 to

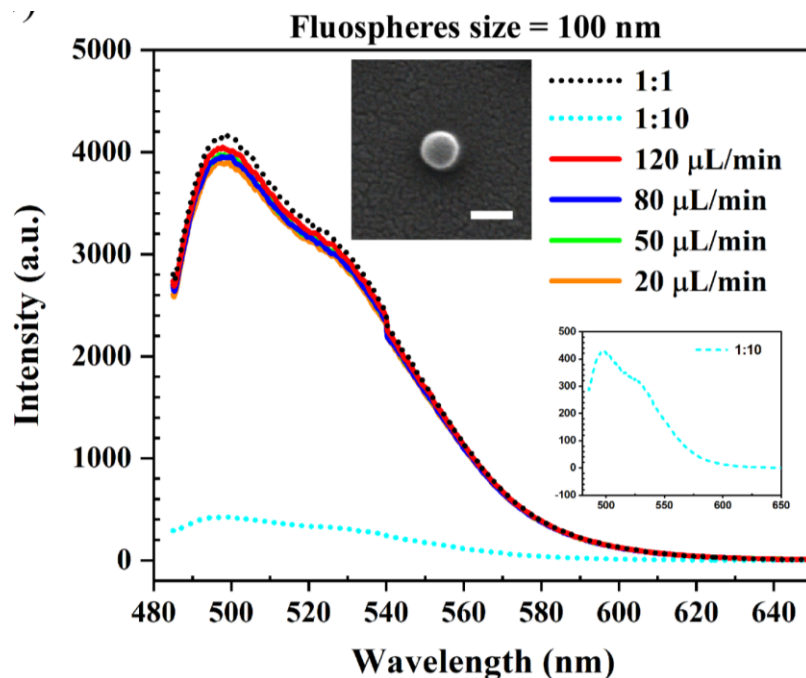


Figure 3.7 The measurement of fluorescent intensity from the filtered supernatant as a function of various flow rates. Inset: SEM image shows dried nanoparticles applied with the diameter of 100 nm (scale bar: 100 nm). Reprinted from [79].

120 $\mu\text{L}/\text{min}$. The filtered supernatants were collected and then measured by the spectrofluorometer. As shown in **Figure 3.6**, when a flow rate of 20 $\mu\text{L}/\text{min}$ is applied, the peak intensity of the supernatant at ~ 518 nm was only ~ 55 counts. This demonstrates that almost all the microparticles were trapped in the fluidic chamber. However, the measured fluorescence intensity increases with the increased flow rates, thus demonstrating an increased particle loss for a significantly deformed device.

To prove that the filtering phenomenon is determined by the nano-sieve deformation and trapping instead of the particle clogging or absorption, we pumped 800 μL aliquots with nanoparticles (diameter ~ 100 nm) with a concentration of 5.5×10^{11} particles/mL (1:1) into the nano-sieve device at different flow rates in the range of

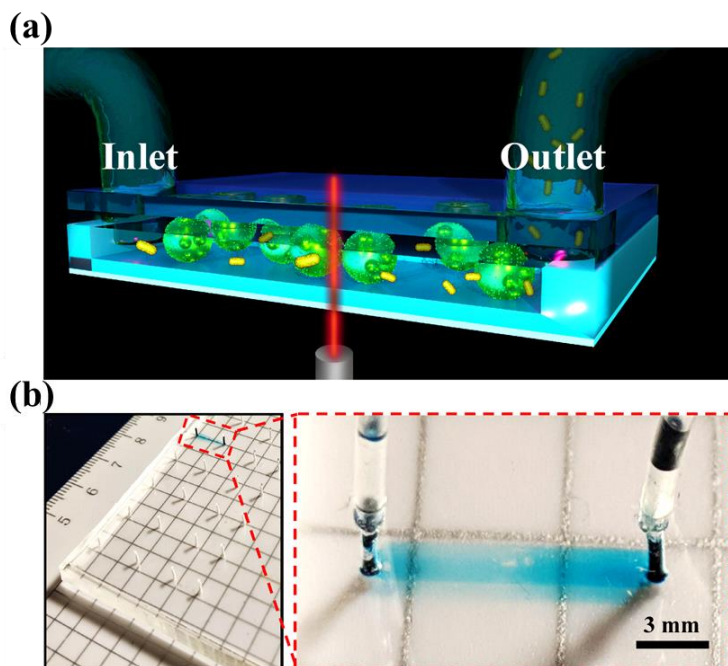


Figure 3.8 Schematic of experimental design for nano-sieve device trapping *C. reinhardtii* cells; (B) The optical micrograph exhibiting the practical device (left); the blue food dye is filled within the entire channel (right). Reprinted from [99].

20 to 120 $\mu\text{L}/\text{min}$, and measured the fluorescence signal of the supernatants. As shown in **Figure 3.7**, the peak intensity of the filtered supernatants remains at $\sim 4,000$ counts, regardless of the flow rate. Because the channel depth is $1\ \mu\text{m}$, the $100\ \text{nm}$ diameter of the fluorescent nanoparticles can easily pass through the nano-sieve device without trapping.

3.3.2 *Soft cells separation*

The schematic of the experimental design is shown in **Figure 3.8(a)**. *C. reinhardtii* cells were pumped into a shallow and wide nano-sieve channel with a low height of $\sim 200\ \text{nm}$, which is specially designed for soft cells separation. Since the diameter of the *C. reinhardtii* cells is $\sim 10\ \mu\text{m}$, they were trapped in the shallow channel as a monolayer, allowing cell media to be flowed toward the outlet. The micrograph of the

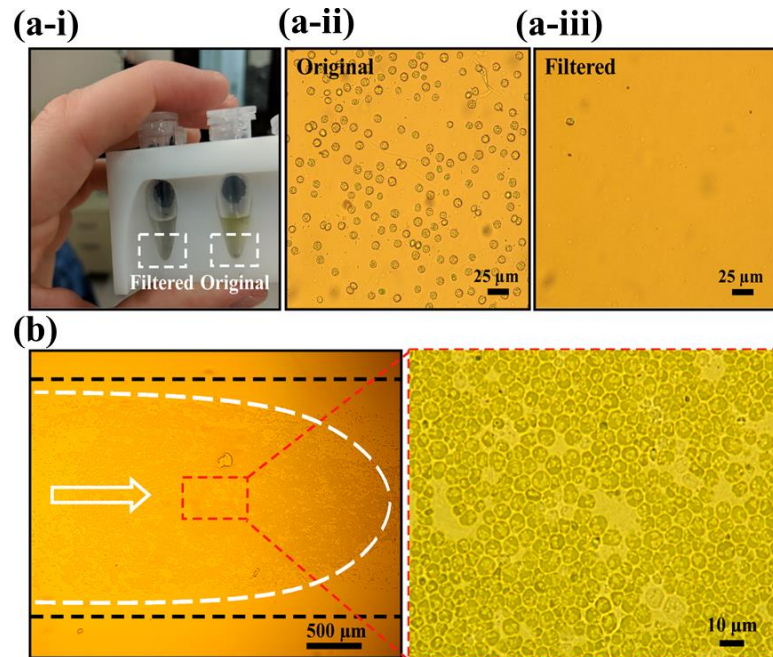


Figure 3.9 (a-i) The filtered solution and original solution collected in the centrifuge tube. The microscope images show the density of cells before (a-ii) and after (a-iii) the filtering process. (b) The *C. reinhardtii* cells trapped within the nano-sieve channel. The white arrow indicates the flow direction. The white dashed parabola shows the profile of the trapped cells. The enlarged region shows the dense *C. reinhardtii* cells. Reprinted from [99].

nano-sieve device is shown in **Figure 3.8(b)**. Each channel has dimensions of 2 mm by 12 mm, which enables the patterning of ~30 channels on a single wafer for high throughput experiments. Before experiments, channels were filled with blue food dye to confirm there were no leaks. As shown in **Figure 3.9(a-i)**, before on-chip experiments, original *C. reinhardtii* cells show light green color (white dashed box). On the other hand, the collected supernatant solution from the nano-sieve outlet shows transparent color, with insignificant change in solution volume. A brightfield microscope was used to image the original solution and filtered supernatant, which are presented in **Figure 3.9(a-ii)** and **Figure 3.9(a-iii)**, respectively. Compared with original solution, the filtered solution has very few cells, demonstrating that the nano-

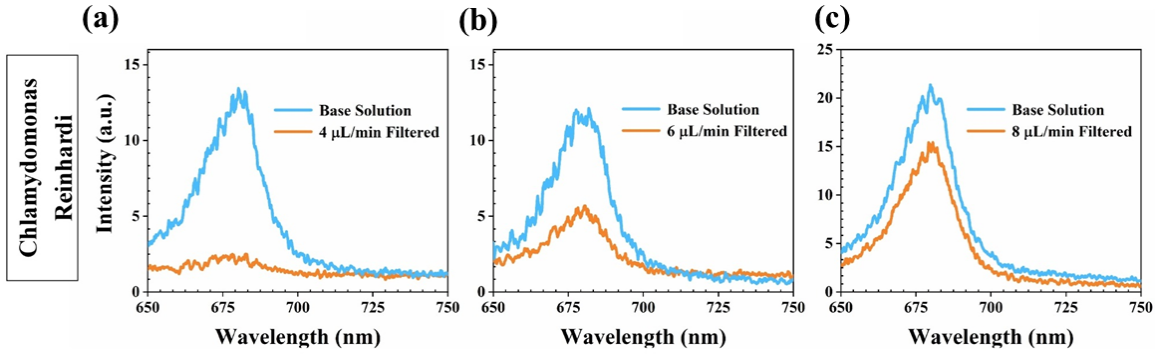


Figure 3.10 (A) The *C. reinhardtii* cells capture efficiency as a function of various applied flow rates of (a) 4 $\mu\text{L}/\text{min}$; (b) 6 $\mu\text{L}/\text{min}$; (c) 8 $\mu\text{L}/\text{min}$, respectively. Reprinted from [99].

sieve device can efficiently trap *C. reinhardtii* cells. The *C. reinhardtii* cells trapped within the nano-sieve device were also imaged. As shown in **Figure 3.9(b)**, the *C. reinhardtii* cells are uniformly patterned with a parabolic profile on their deposition boundary (dashed white line), which is in agreement with a previously investigated theoretical model for channel deformation [79].

The auto-fluorescence spectrum of the *C. reinhardtii* solution (before and after being pumped through the nano-sieve) in terms of the applied flow rate is shown in **Figure 3.10**. The auto-fluorescence intensities of original and supernatant solution were compared by using a spectrofluorometer with an excitation wavelength of 488 nm. With a flow rate of 4 $\mu\text{L}/\text{min}$, most of the *C. reinhardtii* cells were trapped in the nano-sieve device as the fluorescence intensity dropped from ~ 13 to ~ 3 counts (**Figure 3.10(a)**). The cell capture efficiency decreases by increased flow rate. For example, with a flow rate of 6 $\mu\text{L}/\text{min}$, the fluorescence intensity dropped from ~ 13 to ~ 5 counts, indicating some of cell leaking (**Figure 3.10(b)**). At a flow rate of 8 $\mu\text{L}/\text{min}$, the

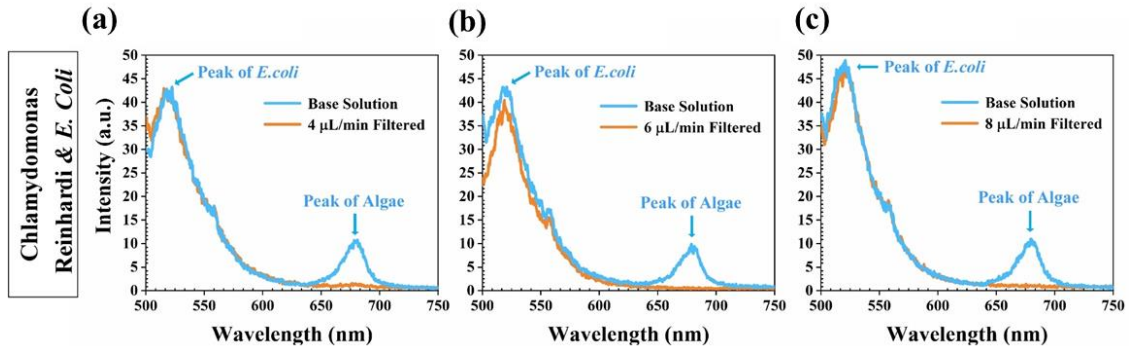


Figure 3.11 The mixture of *E. coli* and *C. reinhardtii* cell separated by nano-sieve device, under the applied flow rate from (a) 4 $\mu\text{L}/\text{min}$; (b) 6 $\mu\text{L}/\text{min}$; (c) 8 $\mu\text{L}/\text{min}$, respectively. The blue curve represents original solution, and the orange curve shows the filtered supernatant. Reprinted from [99].

supernatant intensity reached to 15 counts that is comparable with the stock solution (**Figure 3.10(c)**), demonstrating most of the cells were flowed out from the outlet.

The nano-sieve device can also be used to separate microalgae and bacteria. A labeled *E. coli* and *C. reinhardtii* cell mixture was pumped into the nano-sieve device. As shown in **Figure 3.11**, the mixture solution shows two distinct fluorescence peaks: the labeled *E. coli* cells emit at 520 nm and the *C. reinhardtii* cells emit at 680 nm. After on-chip experiments, almost all the *E. coli* cells passed through the nano-sieve with a flow rate ranging from 4 to 8 $\mu\text{L}/\text{min}$ (**Figure 3.11(a)** to **Figure 3.11(c)**), as the peak of measured intensity of base solution is very close to the one of collected supernatant. However, the *C. reinhardtii* cells were trapped in the device by comparing with the supernatant showing no significant fluorescence peak at 680 nm.

3.4 Discussion

Our cell trapping approach depends on a wide but shallow nano-sieve channel and is achieved by continuously flowing the microparticles and the cells into the channel without

clogging and leaking issues. Moreover, we can adjust the height and deformation of such a channel, making it possible to separate and study different types of cells, such as various sizes. **Figure 3.9(b)** demonstrates that the trapped *C. reinhardtii* cells have larger fringe in size than the cells in the cell media, indicating deformation caused by the flexible PDMS roof. Therefore, our nano-sieve is capable of quantitatively investigating cell mechanics by only tuning the PDMS deformation [100], [101]. This setup also can find application in examining the metabolic and physiological responses of trapped microalgae cells to external chemical or mechanical stimuli [102], [103].

One of the main challenges of the fabrication of the shallow nano-sieve device is the bonding between the PDMS roof and the glass substrate. A positive PR layer was used as a sacrificial layer to cover the etched nano-sieve channel. Thus, oxygen plasma treatment only generated the hydroxyl functional group on the substrate outside of the etched channel. After baking to fully seal the channel, a solvent such as acetone was used to easily dissolve the sacrificial layer. By using this simple and direct approach, the nano-sieves are able to be patterned with an extremely low aspect ratio of 1:10,000 (height: width) without the issue of collapsing PDMS roof. As shown in **Figure 3.4(c)**, without roof collapsing, the entire channel is completely open for the applied air to pass through, as the measured air flow in the channel is as low as ~2.3 sccm, indicating an extremely low resistance built in the channel. On the other hand, roof collapsing after plasma bonding leads to the closure of the channel. Consequently, the measured air flow rate is as high as ~100 sccm. This high resistance presented in the blocked channel is responsible for the high air flow rate measured by the detector of the pressure control system. Furthermore, this type of extremely low aspect ratio nano-device can be further used for microparticle and pathogen

separation and reconfigurable optofluidics [104], [105]. As many channels can be patterned on a single chip, the channels can all be tested in parallel to increase the throughput. While throughput can be increased in this manner, the overall volume of cells that can be trapped is limited due to the small volume of the nano-sieve itself. Once an individual nano-sieve traps too many cells causing the sieve to clog, there is a chance that the pressure built up in the channel can force all materials trapped in the sieve to be removed and proceed into the supernatant. The flow rate through a single channel is also limited to several $\mu\text{L}/\text{min}$ making single channel trapping a slow process. These are limitation at the single channel level that can be addressed by using multiple channels for higher volume trapping at greater rates.

To explore microalgae as the next generation biofuel, it is important to keep microalgae population viable over a long period [106]. Microalgae populations can be adversely affected by bacteria populations and other forms of biological contaminants. For example, certain microbes can damage the microalgae cell wall and prevent its growth [107]–[109]. The deformable nano-sieve device can efficiently separate microalgae from bacteria, enabling controlled movement or trapping of microalgae while mitigating the presence of contaminants. Even though other microfluidic methods have been introduced for microalgae and bacteria separation, they typically require complicated microchannel design and characterizations of the fluid elasticity [110], [111]. Methods for the physical separation of much larger cells have taken advantage of the size difference of cells quite effectively, but not at the scale presented in this work [112], [113]. These devices also have more complicated geometries involving more lengthy fabrication processes compared to the nano-sieve to achieve the needs described in those works. In this nano-sieve, the

separation is achieved by fine-tuning the flow rate and hydrodynamic deformation of the device. As shown in **Figure 3.11**, almost all the contaminant bacteria cells were flowed toward the waste reservoir, without the loss of microalgae. However, micrographs taken before and after the mixed *C. reinhardtii* and *E. coli* solutions indicate that the amount of *C. reinhardtii* cells trapped in the channel was lower than solutions containing only *C. reinhardtii*, even though a significant amount of *C. reinhardtii* cells were still visible in the channel. This indicates that a portion of the *C. reinhardtii* cells were lysed when pumped through the channel with *E. coli* cells. This could have been caused by differences in size, shape, and velocity between *E. coli* cells and *C. reinhardtii* cells flowing through the channels. This may have resulted in the *C. reinhardtii* cells being speared by the *E. Coli* cells, since *E. Coli* cells are rod-like while *C. reinhardtii* cells are spherical. Alternatively, the *C. reinhardtii* and *E. Coli* solution could have been more densely packed due to the additional *E. Coli* causing the *C. reinhardtii* to have less room for deformation. Understanding this phenomenon is not the intention of this work but it is an interesting observation.

3.5 Conclusion

In this chapter, it is demonstrated that a super shallow nano-sieve device with the aspect ratio of 1:10,000 was successfully created for experimentally measuring the capture efficiency of microparticles and nanoparticles, by comparing the fluorescence intensity of solutions with the initial particles and filtered supernatants. Highly size-selective trapping (~99%) was achieved while applying 5 μm microparticles under the applied flow rate of 20 $\mu\text{L}/\text{min}$. It is observed that a significant decrease of capture efficiency was related to the hydrodynamically induced deformation of microfluidic device due to the increased

flow rate. Under a flow rate of 120 $\mu\text{L}/\text{min}$, almost 80% of trapped particles were released and collected. The unique properties of the nano-sieve device can be used to release, concentrate, and collect the target molecules from the original samples for downstream analysis. Furthermore, this directly addresses the clogging issues that are of specific concern in filtration applications. On the other hand, it can be summarized that this novel nano-sieve device was introduced to efficiently and simply separate microalgae/bacteria at the sing-cell level, by using hydrodynamically controlled deformation. Taking advantage of deformable microfluidics, *C. reinhardtii* cells were trapped in the nano-device and subsequently separated from *E. coli* cells. In addition, the utilization of a sacrificial layer avoided channel collapsing and leaking issues while minimizing the flow resistance for the separation process. This fabrication process allows for the generation of many channels on the same chip to increase the overall testing throughput.

Chapter 4. A Three-dimensional (3-D) Bead-stacked Nanodevice for Rapidly Capturing and Retrieving Bacteria from Blood Plasma

Reprinted with the permission from “Chen, X., Miller, A., Cao, S., Gan, Y., Zhang, J., He, Q., Wang, R.Q., Yong, X., Qin, P., Lapizco-Encinas, B.H. and Du, K., 2020. Rapid escherichia coli trapping and retrieval from bodily fluids via a three-dimensional bead-stacked nanodevice. ACS applied materials & interfaces, 12(7), pp.7888-7896.” Copyright {2020} American Chemical Society.

This chapter introduces a novel micro- and nanofluidic device with the stacked magnetic beads, which was developed to effectively and rapidly capture, concentrate, and retrieve *E. coli* from the bacterial suspension in PBS and pig plasma. The small voids between the magnetic beads are used to physically isolate the bacteria through the device. We used computational fluid dynamics (CFD), 3-D optical coherence tomography (OCT) technology, and machine learning to probe and explain the beads stacking in a small 3-D space under various flow rates. A combination of beads with different sizes is utilized to achieve a high capture efficiency (~86%) with a flow rate of 50 $\mu\text{L}/\text{min}$. Leveraging the high deformability of this device, the *E. coli* sample can be retrieved from the designated bacterial suspension by applying a higher flow rate, followed by rapid magnetic separation. This unique function is also utilized to concentrate the *E. coli* from the original bacterial suspension. An on-chip concentration factor of $\sim 11\times$ is achieved. Importantly, this multiplexed, miniaturized, inexpensive, and transparent device is easy to fabricate and operate, making it ideal for pathogen separation in both laboratory and POC settings.

4.1 Introduction

Microorganisms such as *Escherichia coli* (*E. coli*) can cause fecal contamination in recreational and drinking water and pose a high risk of disease transmission. Between 2003 and 2012, 390 outbreaks of *E. coli* infections in the United States were reported, which resulted in nearly 176,000 distinct illnesses, more than 2,000 hospitalizations, and 33 deaths [114], [115]. While *E. coli* infection can be treated with common antibiotics, some strains of this bacteria have developed resistance to antibiotics, leading to longer recovery times and even death. As the development of new antibiotics is slow and challenging, ARBs are gradually becoming one of the leading public health concerns. Currently, around 700,000 people are killed each year due to antibiotic-resistant infections. Projected analysis indicates that if no action is taken to reverse this trend, the global mortality rate caused by ARB could rise to 10 million each year worldwide, leading to an annual loss of 100 trillion USD [15], [116].

Typically, the phenotypic assays have been long used as a gold standard for identifying the bacteria species and antibiotic resistant profile. However, these tests require a long-time period (at least 12 - 24 hours) from sample acquisition to assay results [117]. The study of rapidly and effectively identifying the ARB necessitates bacteria isolation, purification, and concentration from the clinical samples (e.g., saliva, urine, and whole blood), then followed by molecular analysis such as polymer chain reaction (PCR) [118], [119], enzyme-linked immunosorbent assay (ELISA) [120], [121], cell plating [122], [123], and microscopy [124], [125]. For instance, PCR approaches can offer the multiplexing assays and high sensitivity for rapid characterization of specific target bacteria. However,

it is difficult to detect the targets in the medium of blood by PCR analysis, as blood consists of complex components, including red blood cells, white blood cells, and platelets, to decrease the efficacy of the amplification process. ELISA microarrays can separate target bacteria via immunoaffinity of antibodies [126], but the activity of applied antibody could be limited by impurity of bodily fluids, leading to the low capture efficiency of target bacteria [127].

Additionally, membrane-based filtration has been broadly used due to the advantages of cost-effectiveness, simplicity, and rapidity [128]. The captured target bacteria, however, is essential to be retrieved from the membrane by repeated buffer washing. This diluted bacteria sample needs technological development in analytical chemistry to lower the detection limit in turn. Therefore, the method for retrieving target bacteria in a small volume is required to increase the concentration of sample for detection. Moreover, the filtration based on multiple membranes is required to deal with blood samples, however, which could suffer from the clogging issue by the blood cells [129], [130]. Cell leakage is another challenge as the bacteria can deform to pass through the pores. In recent years, microfluidics-based approaches, such as inertial force separation,[131], [132] hydrodynamic separation,[133], [134] electrophoresis,[135], [136] and acoustics separation,[137], [138] have been developed to efficiently separate and detect pathogens; however, all of these methods have limitations and require either sophisticated microfluidic designs or complicated instruments. Therefore, physical barriers such as “T-junction” [139], [140] and micro-obstacle arrays [141], [142] were introduced to capture the cells from bodily fluids; yet, the sizes of most of the bacteria ranged between 0.5 to 5 μm , making the fabrication process challenging.[143]

We previously developed a deformable nano-sieve device for the rapid and size-selective separation of microplastics. Deformation of this device was regulated by flow rate; thus, allowing efficient particle trapping and releasing. Therefore, by exploiting the highly efficient particle trapping of the nano-sieve, stacking of the beads is achieved by hydrodynamic flow at various flow rates, and the liquid-flow profile of the stack is imaged by optical coherence tomography [79]. Then, a novel machine learning method is applied to automatically reconstruct the 3-D topology within the device.[144] Our system can isolate and concentrate *E. coli* cells from either the bacterial suspension or pig plasma by physically capturing the bacteria in the beads assay. Remarkably, the captured bacteria are easily released from the device with flow rate induced channel deformation, followed by bead isolation with a magnet. An on-chip concentration factor of $\sim 11\times$ is achieved by concentrating the bacteria in 100 μL buffer from a 1,300 μL original sample. Utilization of this method allows for the rapid collection of the intact bacteria from patient samples for down-stream molecular diagnosis and imaging. More importantly, multiple nano-sieve devices can be patterned on a small chip by using standard microfabrication techniques and operated by a small syringe pump, leading to a simple, inexpensive, and multiplexed instrument for bacteria sample preparation, intended for POC settings.

4.2 Materials and methods

Polydimethylsiloxane (SYLGARDTM 184) was purchased from Krayden Inc., CO, USA. Glass wafer (D263, 550 μm , double side polished) was received from University Wafer, MA, USA. Magnetic beads with a diameter of 5 μm and 10 μm were ordered from Alpha Nanotech Inc, Vancouver, Canada. Magnetic beads with a diameter of 2.8 μm were purchased from Thermo Fisher Scientific, MA, USA. PBS (1 \times without calcium and

magnesium, PH 7.4 ± 0.1) was purchased from Corning Inc, NY, USA. The fluorescent dye (*BacLight*TM Green Bacterial Stain, excitation/emission: 480/525) was obtained from Thermo Fisher Scientific, MA, USA. The plasma solution (P2891-10 mL) was purchased from Sigma Aldrich, MO, USA, which was diluted by the ratio of 1:10, before running experiments.

4.2.1 Nano-sieve device fabrication

A thin layer of TEOS was deposited onto a cleaned glass wafer with a thickness of 200 nm by using Plasma Enhanced Chemical Vapor Deposition. Then, positive resist (PR: AZ Mir 701) was spin-coated onto the TEOS layer with a thickness of $\sim 1 \mu\text{m}$. Standard lithography was used to pattern the nano-sieve, followed by the development process with CD-26 developer. Buffered oxide etching (BOE) was used to etch the TEOS layer, with an etching rate of $\sim 2.72 \text{ nm/s}$ for 75 seconds. Following that, PR was completely removed using the acetone solution, followed by isopropyl alcohol (IPA) rinsing for 15-20 seconds and then nitrogen drying. A sacrificial layer of PR was patterned in the etched channel via standard lithography. PDMS base and curing agent were mixed at a ratio of 10:1 and then cured in an oven at $85 \text{ }^\circ\text{C}$ for 50 minutes. PDMS was casted to a final thickness of $\sim 5 \text{ mm}$. The inlet and outlet holes were punched using a biopsy punch (diameter = 1 mm). Eventually, the PDMS was fused onto the fabricated glass substrate via an oxygen plasma treatment (Electro-Technic Products).

4.2.2 Cell culture and labeling

Escherichia coli (*E. coli*, ATCC 25922) cells were cultured for 14-15 hours in LB broth at $37 \text{ }^\circ\text{C}$ in a shaker incubator, until they reached an optical density (OD) of 0.5-0.6 measured at 600 nm, which corresponded to an approximate cell concentration of

Table 4.1 Conversion of *E. coli* cell number from cells/mL to CFU/mL [104].

Number of colonies	Dilution of factor	Volume of culture plated (mL)	Initial concentration (CFU/mL)	Initial concentration (cells/mL)	Factor of division
1,000	10,000	0.1	1.00×10^8	2.70×10^8	2.70
Formula [145] of calculation	CFU/mL= (number of colonies × dilution factor) / volume of culture plate				

$\sim 1.71 \times 10^8$ cells/mL. *E. coli* cells exhibited a prolate shape and were $2.38 \pm 0.32 \mu\text{m}$ long and $1.20 \pm 0.21 \mu\text{m}$ wide. The cells were then stained with fluorescent dye to enable visualization. Briefly, a sample of 1 mL of cell culture was centrifuged in a microcentrifuge (VWR Galaxy Mini C1213) at 2000g for 5 minutes; then, the supernatant was discarded. The fresh PBS was applied in order to rinse and re-suspend the condensed cells. Subsequently, 4 μL of the *BacLight* dye was added into 1 mL of the PBS-based bacteria solution for staining the *E. coli* cells; then, the sample solution was vortexed for 10-15 seconds. The stained cells were incubated at room temperature for approximately 20 minutes, followed by centrifugation at 2000g for 5 minutes. Afterward, the supernatant was discarded, and the pellet of cells was rinsed again using fresh PBS to remove the excess dye. Finally, the cells were re-suspended in 0.5 mL of fresh PBS and ready for use in the experiment. Cell concentration expressed as CFU was determined by performing a series of dilutions of overnight liquid culture (OD = 0.92, $\sim 2.71 \times 10^8$ cells/mL). This culture was diluted 1:10 stock/mL four consecutive times. The most diluted culture (0.0001 stock/mL) was then plated on a solid LB agar petri dish and incubated for 24 hours at 37 °C. Following growth overnight, the number

of colonies was counted visually, and the resulting concentration was estimated as 1.00×10^8 CFU/mL (Refer to **Table 4.1**).

4.2.3 *Bead stacking and bacteria-trapping*

A syringe pump (WPI, SP220I Syringe Pump) was used to inject magnetic beads into the nano-sieve channel. Subsequently, the bacteria solution was pumped into the channel using a syringe pump at various flow rates. The filtered waste was collected in a centrifuge tube. Afterward, fresh PBS was applied to wash the magnetic beads and bacteria out of the nano-sieve channel, then collected in another centrifuge tube that was held on a magnetic rack. The nano-sieve channel remained viable throughout the entire study, and no fluid leakage occurred from the inlet/outlet.

4.2.4 *CFD modeling*

The Eulerian multiphase model in FLUENT 19.2 was used to simulate the transport of the beads through the nano-sieve. Water flow was assumed as laminar flow since the maximum Reynolds number was less than 30. Velocity inlet and pressure outlet boundary conditions were applied to the inlet and outlet. The diameter and density of the beads used in the simulation were $10 \mu\text{m}$ and 2500 kg/m^3 , respectively.

4.2.5 *Tomography scanning*

Volumetric topology was evaluated with an optical coherence tomography system (OCT, Thorlab, Ganymede). This system used a near-infrared light source (790 nm to 990 nm) to illuminate the bead sample. Volumetric structural information was reconstructed through the processes involved in background subtraction, λ domain to k

domain conversion, apodization, and inverse Fourier Transform. It was a label-free process, which covered a region of $3 \times 6 \times 1.94 \text{ mm}^3$.

4.2.6 *Segmentation via machine learning*

In order to quantitatively measure the volume of beads in each flow rate, we devised an unsupervised machine learning tool for segmentation. Specifically, we integrated k-mean clustering with the morphological operations, to automatically extract the boundary of the bead stack in 3-D space. K-mean clustering[146] learns the structural similarity within two clusters (groups) of pixels, background, and beads. Within the intensity space, Euclidean distance between the two groups of pixels was iteratively learned by adaptive justification, which determined if an unknown pixel belonged to the beads or not. The segmented boundary was further enhanced when morphological operations were applied to eliminate the noisy pixels at the edge of the beads.

4.2.7 *Spectrofluorometric characterization*

A spectrofluorometer (JASCO FP-8500) was used to measure the fluorescence intensity of the stained cells. The excitation wavelength was set at 480 nm, and the sensitivity was set at level “high” to measure all of the samples in this study. Spectral analysis software (Spectra Manager, JASCO corporation) was used to collect data from the spectrofluorometer.

4.2.8 *Fluorescence microscopy imaging*

The magnetic beads and bacteria samples were imaged with a high-speed camera (AxioCam MRc, Zeiss) mounted on the microscope (AmScope). The fluorescence power source and GFP filter kit were used to visualize the *E.coli* bacteria, which was

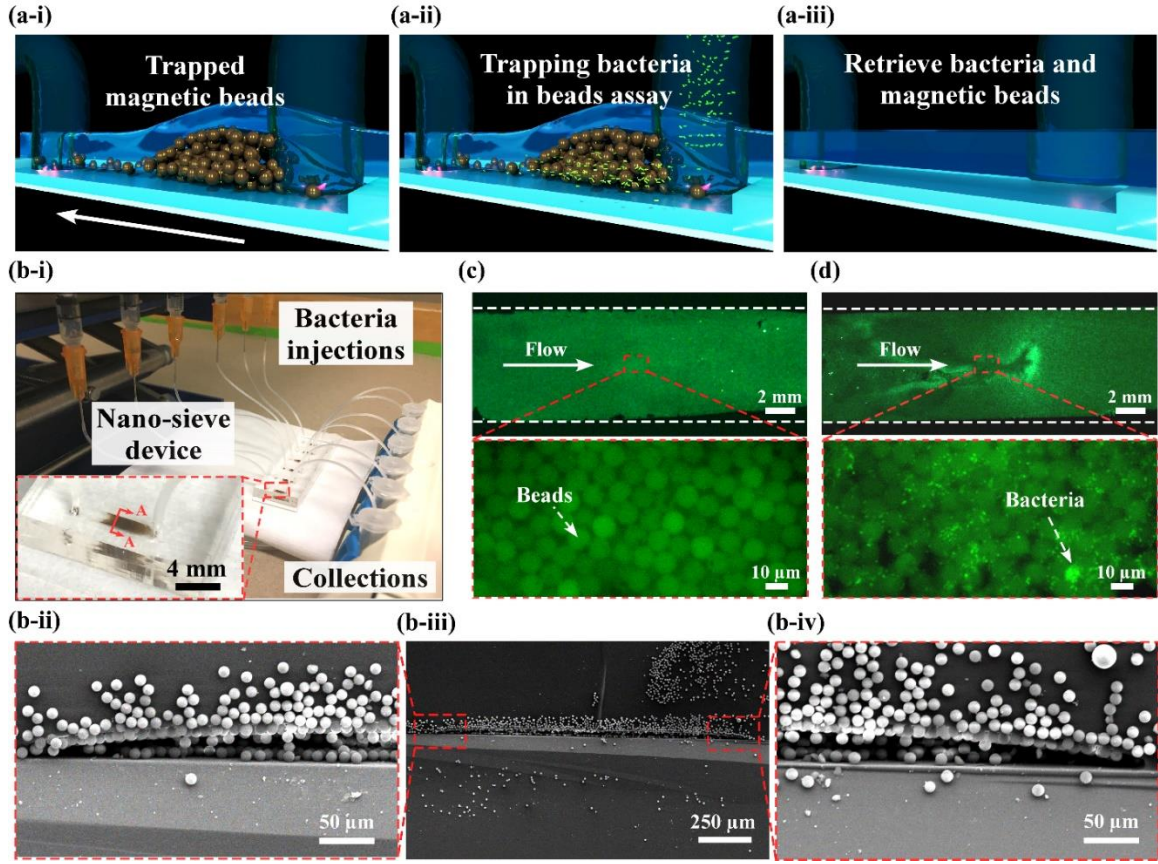


Figure 4.1 (a) Illustration of the magnetic beads stacked nano-sieve device for bacteria isolation: (a-i) beads trapped in the nano-sieve; (a-ii) pumping bacteria into the nano-sieve; (a-iii) bacteria retrieval via high flow rate buffer washing. (b) Magnetic beads trapping: (b-i) Experimental setup. Inset: photograph of beads stacked nano-sieve device. SEM images of the beads stacked nano-sieve channel: (b-ii) Left (high-magnification); (b-iii) Middle (low-magnification); (b-iv) Right (high-magnification). Fluorescence microscope image of the channel before (c) and after (d) bacteria-trapping. The white arrow indicates the flow direction. Reprinted from [104].

stained with a fluorescent dye. The lens magnification was set at $2.5\times$ and $100\times$, with an exposure time of 100 ms.

4.2.9 Scanning electron microscopy (SEM)

SEM (Tescan Mira3) was used to image the magnetic beads in the nano-sieve channel. Samples were mounted onto the specific holder using the copper taper. Then, ~ 200 nm of metal film was coated on the sample by using a sputter coater (SPI-Module™ Sputter Coater). For SEM imaging, the voltage was set at 20 kV.

4.3 Experimental results

Our method of bacterial isolation and retrieval is presented in **Figure 4.1(a)**. Magnetic beads with a diameter ranging from 2.8 to 10 μm are pumped into the nano-sieve device at a flow rate of 50 $\mu\text{L}/\text{min}$. Beads with a large volume are stacked tightly within the 3-D space (**Figure 4.1(a-i)**). Then, the bacterial solution is pumped into the bead-stacked channel under the applied flow rate, and the bacteria are captured by bead assay as the buffer filters into the waste reservoir (**Figure 4.1(a-ii)**). As the bacteria continue to pass through the nano-sieve device, an accumulation of trapped cells occurs in the 3-D microstructure space. Finally, a small volume of fresh buffer at a high flow rate is applied to heave the nano-sieve and release the beads/bacteria mixture (**Figure 4.1(a-iii)**) to the assigned reservoir (Eppendorf tube).

The on-chip experiment setup is shown in **Figure 4.1(b-i)**. The magnetic beads were first deposited within the channel, and bacteria were pumped into the nano-sieve by a multi-channel syringe pump. A magnetic rack was then used to rapidly separate the mixture of released beads/bacteria. A scanning electron microscope (SEM) was used to characterize the bead stacking within the nano-sieve device (**Figure 4.1(b-ii) to Figure 4.1(b-iv)**). The beads are uniformly stacked and heaved the nano-sieve into an arch shape (**Figure 4.1(b-iii)**). We used fluorescence microscopy to image the entire nano-sieve channel before (**Figure 4.1(c)**) and after (**Figure 4.1(d)**) bacteria-trapping, where the stained bacteria are trapped within the interspaces of the beads assay.

The beads stacking process under a flow rate of 40 $\mu\text{L}/\text{min}$ is shown in **Figure 4.2**. Initially (0 second), the nano-sieve is empty (**Figure 4.2(a)**). Under the beads filling

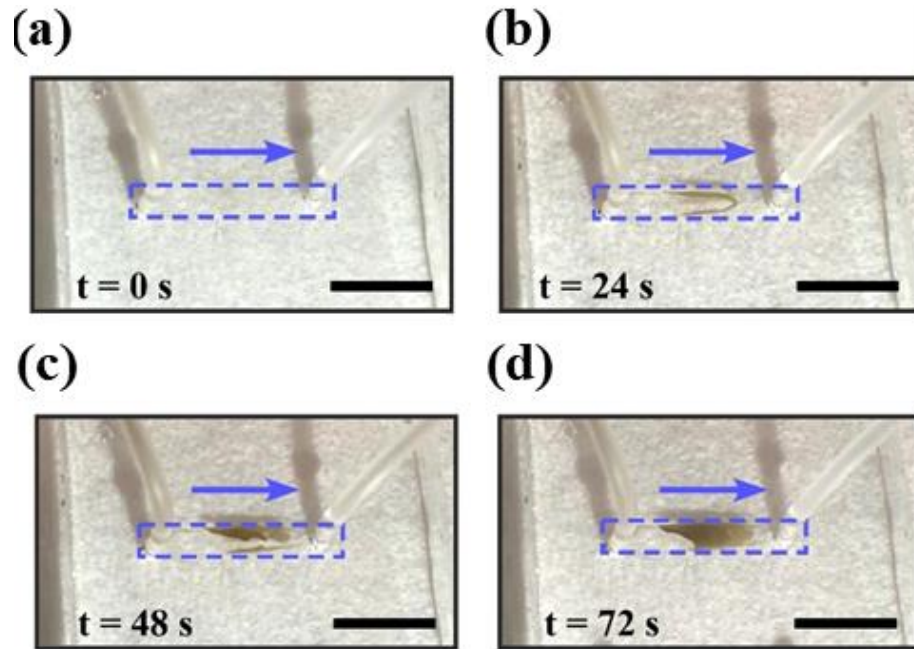


Figure 4.2 (a) Beads stacking process during 72 s with a flow rate of $40 \mu\text{L}/\text{min}$. The dashed purple box indicates the boundary of channel. The blue arrow indicates the flow direction. Scale bar: 4 mm. Reprinted from [104].

process (24 seconds), the beads begin to stack and form an arch shape (**Figure 4.2(b)**). However, as the pressure drop builds up in the nano-sieve (48 seconds), beads are pushed to the sides of the channel and burst out to the outlet from the central path of the channel (**Figure 4.2(c)**). This process also moves the beads pack closer to the outlet. As the channel deformation is much smaller at the outlet, it allows for beads to be filled (72 seconds) into the device without bursting, and a denser bead stacking in the 3-D space is achieved (**Figure 4.2(d)**). In order to understand this time-dependent bead-filling process, we also developed a computational fluid dynamics (CFD) model to study the magnetic bead transport in the deformed nano-sieve. We assumed that the deformation of the PDMS roof is dominated by pumping pressure and that the effect of the stacked beads and heaving of the roof is negligible. **Figure 4.3** depicts the flow rate of $20 \mu\text{L}/\text{min}$, the highest flow

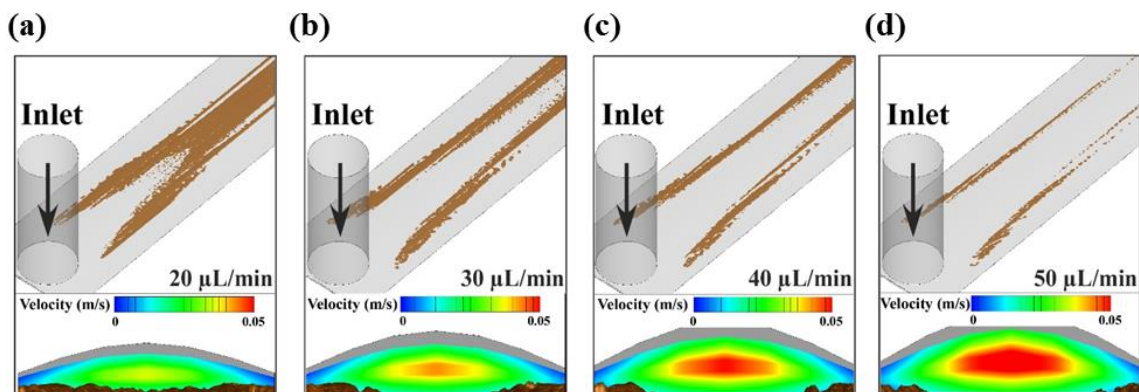


Figure 4.3 The simulated results from computational fluid dynamics (CFD). Top: CFD calculation of nano-sieve deformation and beads flow pattern; bottom: flow velocity with a flow rate of (i) 20 $\mu\text{L}/\text{min}$; (ii) 30 $\mu\text{L}/\text{min}$; (iii) 40 $\mu\text{L}/\text{min}$; (iv) 50 $\mu\text{L}/\text{min}$. Reprinted from [104].

velocity in the channel is 0.035 m/s, and the maximum height in the channel is 19 μm at the middle cross-sectional (Y-Z) plane. The velocity at the centroid of the channel increases with the increased flow rate (**Figure 4.3(a) to Figure 4.3(d)**). At a flow rate of 50 $\mu\text{L}/\text{min}$, the highest flow rate is 0.055 m/s, and the maximum height is 30 μm at the middle cross-sectional plane. This high flow rate and large deformation of the channel cause the beads to move to the sides of the channel and to the outlet reservoir. This result matches our experimental observation and explains the initial bead stacking and burst process, as shown in **Figure 4.2(a) to Figure 4.2(c)**.

Following the initial burst, the beads move closer to the outlet. Moreover, the inflow of beads starts to reconstruct the 3-D space, which is further used for bacteria-trapping. We used 3-D tomography technology to scan the entire channel after the bead stacking and applied machine learning tools to analyze the topology-related data (**Figure 4.4**). The scanning results and quantitative measures of the microbead array are depicted in **Figure 4.4(a)**. An overlay of the 3-D mask (in pink) and the raw data are found to be dependent

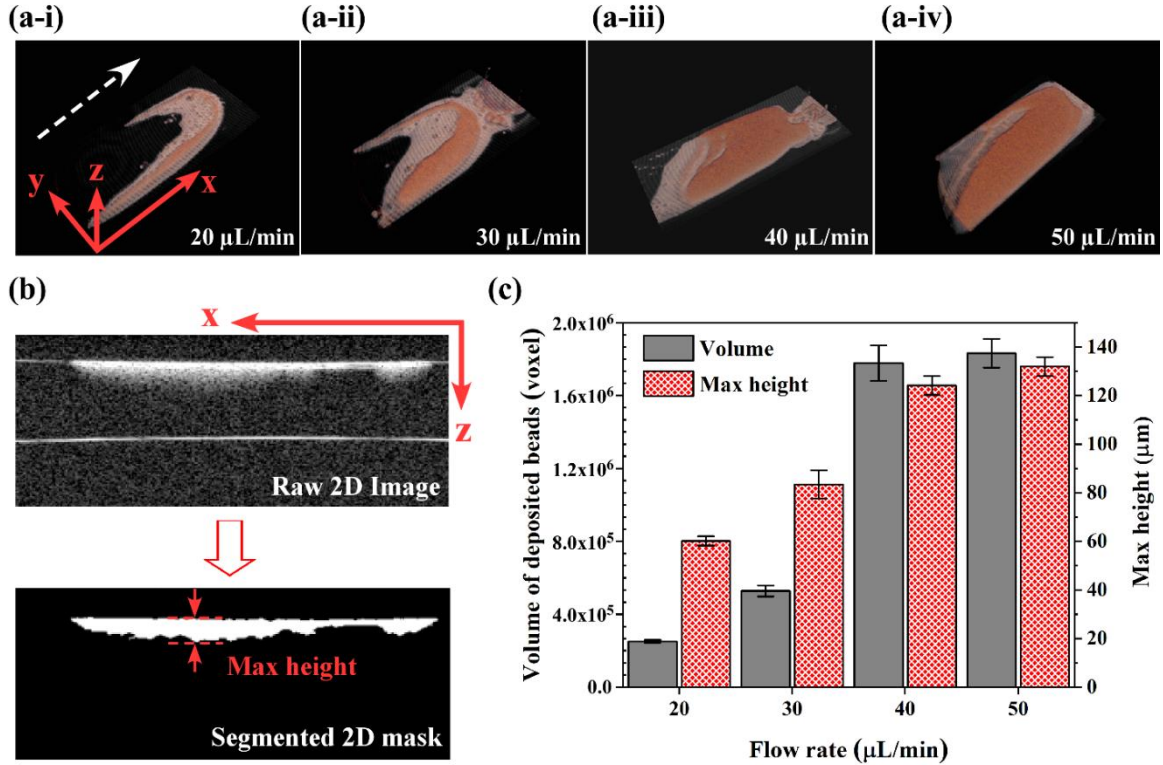


Figure 4.4 (a) Optical coherence tomography scan of the beads stacked nano-sieve with the flow rate ranging from 20 - 50 $\mu\text{L}/\text{min}$. (b) Cross-section view of beads stacking: raw 2D image (top) and segmented 2D mask (bottom). (c) Experimentally measured volume of the deposited beads and maximum height in the channel after beads stacking. Reprinted from [104].

on the flow rate ranging from 20 to 50 $\mu\text{L}/\text{min}$. Inspired by the machine learning-based segmentation task in 2D-cell microscopy image[147] and 2D-material visualization,[148] we generated a 3-D mask using a novel segmentation method, which was a combination of an unsupervised machine learning method, K-mean clustering,[146] and morphological operation.[149] A typical example in a cross-sectional plane is depicted in **Figure 4.4(b)**. The white region corresponds to bead stacking, and the black region corresponds to the background and the coverslip. The maximum height of the bead stack was measured from the mask. For each volume, 3-D topology was generated by aligning 2D masks in 3-D space. The volume of deposited beads and the maximum height versus flow rates are presented in **Figure 4.4(c)**. With a flow rate of 20 $\mu\text{L}/\text{min}$, the total volume and the

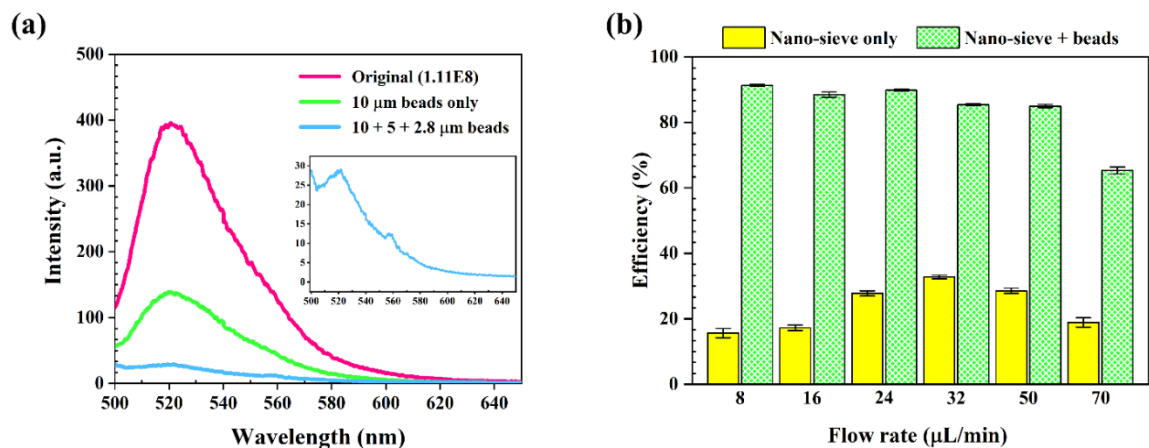


Figure 4.5 (a) Uncorrected emission curve of filtered solution from nano-sieve with a flow rate of 8 $\mu\text{L}/\text{min}$: Original solution (pink); Stacked with only 10 μm beads (green); Stacked with mixed beads with sizes of 2.8 μm , 5 μm , and 10 μm (blue). The emission peaks are centered at $\sim 520\text{ nm}$. (b) Bacteria-trapping efficiency versus flow rate of nano-sieve only (yellow) and beads mixture stacked nano-sieve (patterned green). Reprinted from [104].

maximum height in the channel were $\sim 2.50 \times 10^5$ voxel and $\sim 60\ \mu\text{m}$, respectively. We found that the total volume and maximum height show an uptrend that corresponded to an increased flow rate. For example, with a high flow rate of 50 $\mu\text{L}/\text{min}$, the volume and maximum height were increased to $\sim 1.83 \times 10^6$ voxel and $\sim 132\ \mu\text{m}$, respectively. As the original channel height was only 200 nm, a $\sim 650\times$ increase in channel height was observed without showing channel failure.

Figure 4.5 presents the trapping efficiency and retrieval factor of the bacteria in a nano-sieve device. Two hundred microliters of the stained bacteria sample (concentration: 1.11×10^8 CFU/mL) were pumped into the beads-stacked nano-sieve device, and the fluorescence signal of the filtered supernatant was measured by using a spectrofluorometer at an excitation wavelength of 480 nm. By introducing 10 μm magnetic beads in the nano-sieve, the measured relative fluorescence intensity of the filtered supernatant is ~ 140 counts, demonstrating that most of the bacteria ($\sim 65\%$) are trapped in the nano-sieve device (**Figure 4.5(a)**). Alternatively, the measured fluorescence intensity of the supernatant was

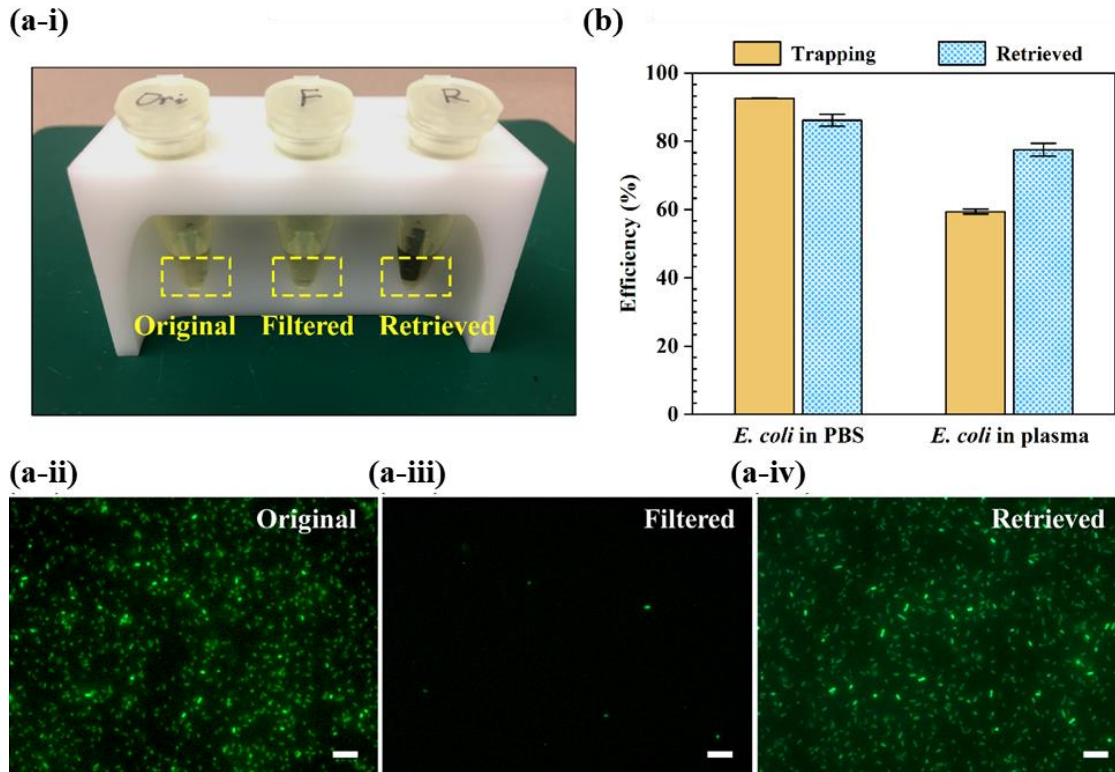


Figure 4.6 (a-i) Photograph of the bacteria samples: Original (left); Filtered (middle); Retrieved (right). Fluorescence microscope image of original solution (a-ii), filtered solution (a-iii), and retrieved solution (a-iv). Scale bar: 10 μm . (b) Bacteria-trapping efficiency and retrieval efficiency from PBS (brown) and pig plasma (patterned blue). The applied flow rate is 8 $\mu\text{L}/\text{min}$. Error bars indicate standard deviation of the mean. Reprinted from [104].

only ~30 counts by introducing a bead mixture with various sizes (2.8 μm , 5 μm , and 10 μm in order), which indicated that almost all the bacteria (~92%) were captured in the nano-sieve device. The bacteria-trapping efficiency versus flow rate was then explored. As depicted in **Figure 4.5(b)**, without any stacked beads, the bacteria-trapping efficiency is between 18% - 38% at flow rates ranging from 8 to 70 $\mu\text{L}/\text{min}$. The addition of the beads mixture to the nano-sieve device significantly increases the trapping efficiency. The bacteria-trapping efficiency is above 86% at flow rates of 8 - 50 $\mu\text{L}/\text{min}$. At a flow rate of 70 $\mu\text{L}/\text{min}$, a bacteria-trapping efficiency of 64% is achieved, which is still 3 \times higher than that observed within the nano-sieve device without stacked beads. Following bacteria-

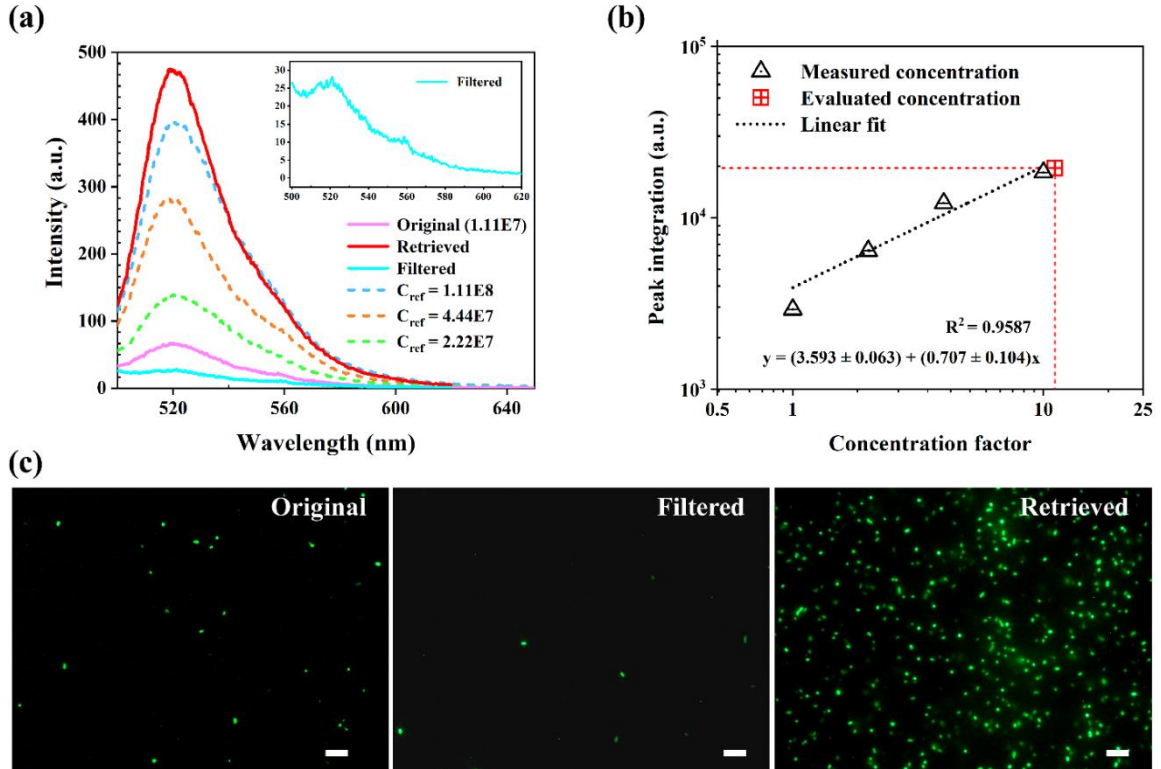


Figure 4.7 (a) Uncorrected emission curve of bacteria solution with various concentrations. The emission peak is centered at ~ 520 nm. The input bacteria concentration and volume are 1.11×10^7 CFU/mL and 1,300 μ L, respectively (solid pink line). The retrieved sample is in 100 μ L PBS (solid red line). Three other measured fluorescence intensities (colored dashed lines, marked as C_{ref}) indicate the stained bacteria stock solution with a concentration of 2.22×10^7 , 4.44×10^7 , and 1.11×10^8 CFU/mL, respectively. These references are used to calculate the concentration factor. Inset: Uncorrected emission curve of filtered solution. (b) Fluorescence intensity versus bacteria concentration. The estimated concentration factor is 13 and the evaluated concentration factor is ~ 11 . Error bars are standard error of the mean. (c) Fluorescence microscope image of original solution (left); filtered solution (middle); retrieved (right). Scale bar: 10 μ m. Reprinted from [104].

trapping, 200 μ L phosphate-buffered saline (PBS) was pumped into the nano-sieve device at a flow rate of ~ 900 μ L/min. This high flow rate induces significant deformation of the PDMS roof, thus releasing the beads and bacteria into an Eppendorf tube (**Figure 4.1(b)** and **Figure 4.6(a-i)**). A fluorescence microscope was used to image the original bacteria sample (**Figure 4.6(a-ii)**), filtered supernatant (**Figure 4.6(a-iii)**), and retrieved sample (**Figure 4.6(a-iv)**). Only a few bacterial cells were observed in the filtered supernatant, again proving negligible bacteria leaking. The retrieved bacteria solution (cells in the unit

area: 0.142 cells/ μm^2) has similar cell numbers to the original sample (cells in the unit area: 0.163 cells/ μm^2), indicating highly efficient bacterial retrieval. Our platform is capable of trapping and retrieving bacteria from various media, including bodily fluids. We also achieve a bacteria-trapping efficiency of ~60% and a retrieval rate of 80% from pig plasma at a flow rate of 8 $\mu\text{L}/\text{min}$ (**Figure 4.6(b)**).

The bead-stacked nano-sieve can be applied to concentrate bacteria samples when the original cell number with a low concentration is dealt with. To explore this, we pumped 1,300 μL bacteria with a concentration of 1.11×10^7 CFU/mL into the bead-stacked nano-sieve device. Then, we retrieved the bacteria by introducing 100 μL PBS buffer at a high flow rate of ~900 $\mu\text{L}/\text{min}$, to expect an on-chip concentration factor of 13 \times . As depicted in **Figure 4.7(a)**, the original sample with a concentration of 1.11×10^7 CFU/mL only shows ~60 counts. Notably, the retrieved sample shows fluorescence intensity of ~480 counts, indicating a dramatic increase in sample concentration. The integrated fluorescence signal of **Figure 4.7(a)** with a wavelength from 520-640 nm was plotted and is presented in **Figure 4.7(b)**, showing an excellent linear relationship. A ~11.2 \times on-chip concentration factor was achieved based on our experimental data, which closely matched the intended 13 \times on-chip concentration. This powerful on-chip concentration capability was further confirmed by fluorescence microscopy. The retrieved bacterial sample shows a much higher concentration than the original sample, when compared to the filtered supernatant, indicating an efficient on-chip concentration (**Figure 4.7(c)**).

4.4 Discussion

Antibiotic-resistant bacteria (ARB) have become a severe public health concern. Fortunately, this risk can be reduced via the correct use of prescriptions, and by avoiding

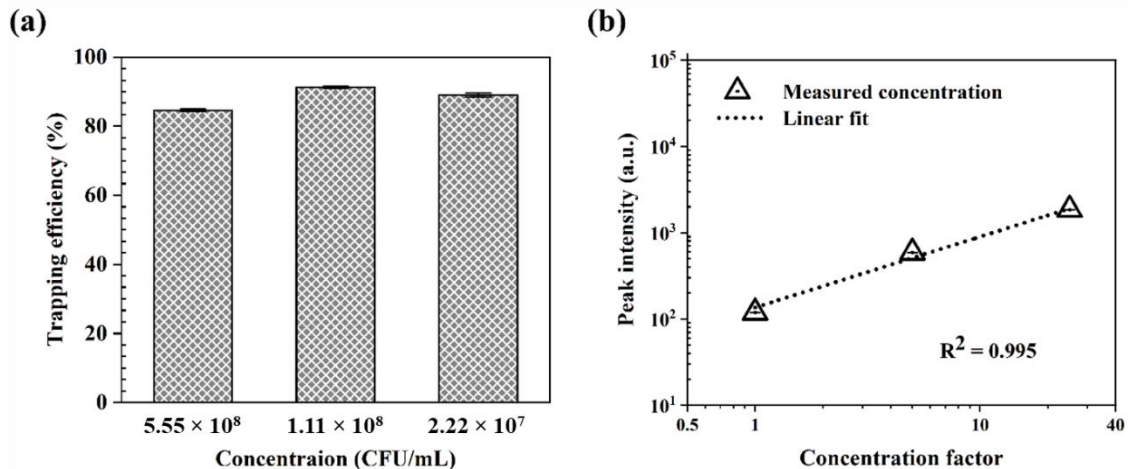


Figure 4.8 (a) The investigation on the trapping efficiency as a function of various *E. coli* bacteria concentrations, under a flow rate of $8 \mu\text{L}/\text{min}$. (b) The linearity of three concentrations tested (from high to low: 5.55×10^8 , 1.11×10^8 , and 2.22×10^7 CFU/mL). Reprinted from [104].

unnecessary prescriptions, and over-prescription of antibiotics.[150], [151] In this regard, rapid isolation of the target bacteria from various samples is an essential step toward the identification of antibiotic resistance and providing early-treatment.[152] Reported here is the development of a magnetic beads-stacked nano-sieve device to separate, concentrate, and retrieve bacteria from both the buffer solution and pig plasma samples. Leveraging the deformation capability of PDMS, our novel system is able to stack microbeads in a large 3-D space to capture microorganisms from the various media. The bacteria can be trapped in the voids of the microbeads stack without altering their properties. Our system is simple to build and cost-effective as it does not require expensive, complicated, and time-consuming nanolithography. Thus, this novel method should be ideal for high throughput, multiplexing, and inexpensive clinical applications. Capture efficiency remained as high as 86%, even by applying a high flow rate of $50 \mu\text{L}/\text{min}$, which indicated that the system could process a larger sample volume in a shorter amount of time. Additionally, the

trapping efficiency is remaining high (>85%) regardless of the bacteria concentration, further demonstrating the robustness of our system (as shown in **Figure 4.8**).

Unlike conventional membrane-based filtration, which is challenging to recover captured pathogens [153], our system is able to retrieve the captured bacteria into different bacterial suspensions, designed for lysis-free diagnostics [154]. Even though several approaches based on immunoaffinity separation have been widely used and show high target specificity, they require expensive and delicate antibodies to bind with the surface antigens [155], [156]. In addition, immunoaffinity typically has a low capture efficiency and cannot detect the presence of pathogens when the cell number is low, and it also requires time-consuming sample preparation, which is not suitable for POC applications [157]. Our approach entirely relies on physical separation, which is robust and does not interfere with the host cellular materials. Following rapid sample retrieval and separation, the samples are ready to be used for genotype analysis (e.g., PCR [158], [159]) and standard phenotype analysis (e.g., cell plating [160], [161]). Furthermore, unlike other microfluidic-based approaches that necessitate the use of complicated instruments for operation [133], [135]–[138], [162]–[164], our approach only requires a small syringe pump and the miniaturized nano-sieve device; thus, it could be used for both lab-based or POC diagnosis.

A unique design that incorporates tightly stacked magnetic beads to trap the bacteria was employed, and the efficiency of bacteria-trapping depended on the configuration of the beads stacking. Instead of using complicated micro- and nanofabrication to physically isolate the bacteria [165], [166], our approach simply relies on bead stacking at various flow rates and does not require expensive and time-consuming nanolithography processes [167], [168]. As the beads are pushed to the outlet of the channel, they begin to stack in the

3-D space (**Figure 4.2(a)-(d)**). The channel height reaches to $\sim 132 \mu\text{m}$ at $50 \mu\text{L}/\text{min}$, which is $\sim 650\times$ higher than the original channel height ($\sim 200 \text{ nm}$). This sizeable 3-D space created by bead stacking provides numerous voids for bacteria-trapping. This is crucial for bacteria-trapping, especially for on-chip concentration, as more voids within the bead array are required to capture bacteria. Moreover, tension caused by deformation of the PDMS roof is responsible for locking the bead array into position. Even with a flow rate at $50 \mu\text{L}/\text{min}$, we did not observe beads leaking from the nano-sieve, enabling the great capability of processing a large sample volume.

We found that the bead size is also an essential factor for efficient bacteria-trapping. As shown in **Figure 4.5**, mixing $2.8 \mu\text{m}$ and $5 \mu\text{m}$ beads with the $10 \mu\text{m}$ beads significantly improves the capture efficiency. Since *E. coli* has a dimension less than $2 \mu\text{m}$ and has great deformability [169], [170], it can pass through the small voids created by large beads, at a higher flow rate. Thus, we first applied the $10 \mu\text{m}$ beads into the nano-sieve to occupy the 3-D space, followed by the application of smaller beads. The tightly stacked smaller bead array has smaller voids, thus enhancing the bacteria-trapping efficiency. We observed a slight reduction in capture efficiency at a flow rate of $70 \mu\text{L}/\text{min}$ due to bead leaking caused by the larger hydrodynamic deformation. This problem could be easily resolved by designing a multi-channel nano-sieve device to reduce the deformation and beads leaking, which means each channel can collaborate with lower flow rate but finally reaching a high flow rate for the total volume of applied samples.

One of the main advantages of microfluidics is the miniaturized size, enabling multi-device operation on a small scale and reducing the consumption of applied samples.[171], [172] Leveraging the small size of our nano-sieve device ($2 \text{ mm} \times 8 \text{ mm}$), it is possible to

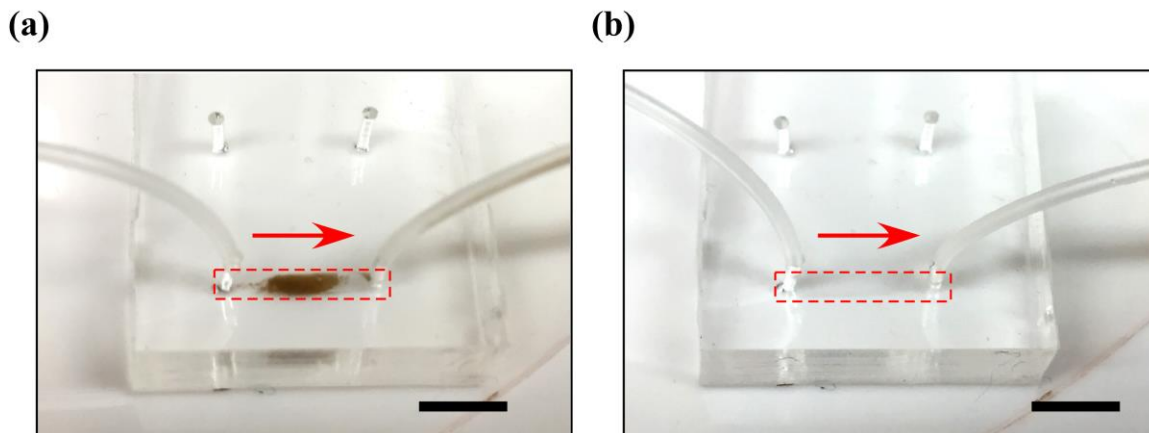


Figure 4.9 The washing process for retrieving the bacterial and magnetic beads from nano-sieve channel. (a) The trapped beads and bacteria; (b) The washed channel by PBS. Scale bar: 4 mm. Reprinted from [104].

pattern hundreds of the nano-sieves on a 4-inch wafer scale for high throughput multiplexing detection. This could also be used to screen multi-resistant organisms by applying many different antibiotics to the isolated samples. The small size of the nano-sieve device also enables us to work with sample volumes ranging from nanoliters to milliliters; thus, it is compatible with either a finger prick test or a blood draw.

The microbial load of ARB could be as low as $\sim 10 - 100$ CFU/mL in the bodily fluids [173]; thus, concentrating the target is always necessary to reach the detection threshold. By introducing $1,300 \mu\text{L}$ of the *E. coli* sample into the nano-sieve device and then retrieving the bacteria in $100 \mu\text{L}$ of the buffer (see the retrieval process in **Figure 4.9**), we demonstrated an on-chip concentration factor of $\sim 11\times$, which was evaluated by the linearity of the bacterial concentration (1.11×10^7 CFU/mL to 1.11×10^8 CFU/mL). Thus, our system is a useful platform to deal with low concentration samples and could be applied to extend the detection limit. The on-chip concentration factor could be further increased by the application of a larger volume of initial sample and by lowering the volume of fresh buffer solution used for retrieval. By using our novel approach, bacteria could be easily

separated, concentrated, and retrieved into any buffer solution and would be available for a direct molecular diagnostic testing of suspects in a POC setting.

4.5 Conclusion

Aiming to produce a rapid and reliable ARB separation and detection method, our work developed the first miniaturized system for the physical separation and concentration of bacteria from the buffer solutions and blood plasma. This was achieved via 3-D stacking of the nonfunctional magnetic microbeads in a confined nano-sieve device with numerous voids at the interface, which were characterized by optical tomography, fluid dynamics simulation, and machine learning reconstruction. We demonstrated that this system exhibits a very high bacterial capture efficiency and is capable of on-chip aggregation when dealing with lower concentration samples. The bacteria are simply retrieved and concentrated in the designated buffer without altering the properties of bacteria themselves. We believe that our system can be used for a wide spectrum of medical and technological applications, including rapid diagnosis of antibiotic-resistant bacteria in bodily fluids, such as plasma or whole blood.

Chapter 5. Understanding the 3-D Microbeads Stacking in Deformable Nano-sieve for Efficient Plasma Separation and Blood Cell Retrieval

*Reprinted with the permission from “Chen, X., Zhang, S., Gan, Y., Liu, R., Wang, R.Q. and Du, K., 2022. Understanding microbeads stacking in deformable Nano-Sieve for Efficient plasma separation and blood cell retrieval. **Journal of colloid and interface science**, 606, pp.1609-1616.”*

Efficient separation of blood cells and plasma is key for numerous molecular diagnosis and therapeutics applications. Despite various microfluidics-based separation strategies having been developed, there is still a need for a simple, reliable, and multiplexing separation device that can process a large volume of blood. Here we show a microbead-packed deformable microfluidic system that can efficiently separate highly purified plasma from whole blood, as well as retrieve blocked blood cells from the device. To support and rationalize the experimental validation of the proposed device, a highly accurate model is constructed to help understand the link between the mechanical properties of the microfluidics, flow rate, and microbeads packing/leaking based on the microscope imaging and the optical coherence tomography (OCT) scanning. This deformable nano-sieve device is expected to offer a new solution for centrifuge-free diagnosis and treatment of bloodborne diseases and contribute to the design of next-generation deformable microfluidics for separation applications.

5.1 Introduction

Blood is a multi-phase biological fluid that can be analyzed for assessing the fundamental functions of the human body, like homeostasis [174], nutrient transportation [175], regulation of body temperature and pH [176], circulation of oxygen [177], and immune cell count throughout the body [178]. Cells and protein-enriched plasma are two major components in blood. The cell suspension consists of white blood cells, red blood cell (RBCs), and platelets. The analysis of physical properties of cell components in blood can be used for the diagnosis of several cell-based diseases, such as cancer [179], [180], sepsis [181], [182], sickle-cell anemia [183], [184], and malaria [185], [186]. Human plasma is a clear and straw-colored liquid (54.3% by volume of whole blood) comprised of various proteins (e.g., fibrinogen, globulin, and albumin) and several inorganic compounds [187]. Efficiently separating plasma from whole blood is a key factor in molecular diagnostics and therapeutics. For instance, testing the relative proportions of biological substances from the plasma, e.g., cholesterol and glucose, can be used to evaluate the health condition and function of internal organs in the human body [178]. The quantitative analysis of specific protein biomarkers in plasma can be used to diagnose diseases such as genetic abnormalities [188], [189], paraproteinemias [190], [191], and hemoglobinopathies [192], [193]. Therefore, extracting highly purified plasma from whole blood is important to the precise assessment and diagnosis of those diseases.

Conventionally, extracting human plasma from whole blood in laboratories and clinics relies on centrifugation process, requiring expensive and bulky instrumentations, skilled technician, and time-consuming protocols. The throughput is low as only a few samples can be processed at the same time. On the other hand, various microfluidic platforms have

been introduced to separate plasma from whole blood. For example, well-defined weir structures with a gap size of 0.5 μm have been demonstrated to continuously separate plasma in a cross-flow configuration [194]. The small gap can block the cell components and allows the cell-free plasma to flow through the microfluidic channel. Similarly, transverse-flow microfilters with the same gap size were reported to efficiently separate plasma [195]. Moorthy et al. developed a novel filter with porous structures in a microchannel by an emulsion photo polymerization process [196]. However, the fabrication and integration of sub-micron features into microfluidic devices are challenging. The small fluidic passage also limits the filtration speed. Due to the high fluidic resistance, blood needs to be extensively diluted (typically 1:20), further delaying the processing time. Recently, an alternative method based on a microbead-stacked microchannel has been developed [197]. This microbead-based filter impeded RBCs transportation and permitted the cell-free plasma to flow through the microbead array by capillary force without dilution. However, the slow capillary action in these systems can only work with a low flow rate (0.03-0.6 $\mu\text{L}/\text{min}$ [198], [199] and is not suitable when dealing with a large volume of blood. Therefore, developing a miniaturized and simple microfluidic device that can be used for multiplexing and rapid plasma separation from whole blood is urgently needed for various biomedical applications [200].

Deformable microfluidics with a very low channel height have been introduced recently to capture and pack various types of micro-and nanofeatures [96], [201], [202]. To understand the complicated deformation process, Christov *et al.* developed a theoretical model to establish the relationship between flow rate and microfluidic deformation, which corresponds well with the experimental results [80]. We further extended this model and

applied it to the design of deformable microfluidics and demonstrated good overlap with experimental observations [79]. However, these models only concentrate on the change of flow properties and less is known on how change in the structural properties of the structures will impact the nano-sieve performance, leading to questions about whether these models are useful in this scope.

This chapter details a deformable microbead-stacked nano-sieve system for efficient plasma separation from whole blood, operating at a high flow rate. The deformable nature of the nano-sieve enables RBCs retrieval by a simple hydrodynamic deformation. Furthermore, we study the stability of microbeads-stacked micropattern within the nano-sieve channel via fluorescence microscopy, optical coherence tomography (OCT), microfluidics, mechanical testing for material characterization, and computational fluidic calculation, building and modelling a reliable system for the successful plasma extraction. By varying the mechanical properties of the nano-sieve, a new model is established to better explain the fluid-structure interaction. This plasma extraction system capable of RBCs retrieval could be widely used for many clinical applications either in hospitals or POC settings.

5.2 Materials and methods

5.2.1 *Materials*

Polydimethylsiloxane (PDMS, Sylgard[®]184) was obtained from Krayden Inc., CO, USA. Glass wafer (D263, thickness: 550 μm) was purchased from University Wafer, MA, USA. Silica magnetic beads (diameter: 10 μm) were received from Alpha Nanotech Inc., Vancouver, Canada. Phosphate buffered saline (PBS) solution (1 \times

without calcium and magnesium, pH 7.4 ± 0.1) was ordered from Corning Inc., NY, USA. Fresh human blood with EDTA was obtained from *StemCell* Technology Inc., Vancouver, Canada.

5.2.2 Preparation of PDMS

For mechanical testing, PDMS curing agent and base were mixed in different weight ratios of 1:5, 1:10, and 1:20, respectively, and then degassed in a vacuum chamber for 2 hours before molding. The steel mold was fabricated following the Type IV specimen standard in ASTM D638. After pouring the PDMS mixture into the metal mold, it was left in the vacuum furnace at room temperature for 5 hours to eliminate any air bubbles caused by stirring mixing. The mixture was then cured in an oven at 65°C for 12 hours. PDMS can shrink when moved from higher to lower temperatures [203]. Thus, the PDMS replica was completely cooled in ambient environment for 24 hours to eliminate the influence of shrinkage on the strain measurement and the device fabrication.

5.2.3 Hardness testing

The PDMS sample was subjected to Shore A scale hardness measurement in accordance with the ASTM D2240-15 using a FstDgte Shore A durometer. To assure the constant test rate and parallel contact of the durometer to the specimen, the durometer was mounted on a Chatillon® TCD1221 digital force tester. A cuboid sample with a thickness of 10 mm was fabricated by using different mixing ratios. Fifteen different points were tested on a single sample with at least 6 mm apart from each point, as recommended by the ASTM standard.

5.2.4 *Nano-sieve device fabrication*

A 200 nm tetraethyl orthosilicate (TEOS) layer was deposited on a glass wafer and the nano-sieve geometry was patterned by standard photolithography (length: 10 mm; width: 2 mm). Buffered oxide etching (BOE) was used to etch through the TEOS layer. The channel was filled with positive photoresist (AZ-701) with a thickness of $\sim 1 \mu\text{m}$ as a sacrificial layer. A PDMS slab (thickness: 5 mm) was bonded over the TEOS layer with oxygen plasma bonding (Electro-Technic Product, BD-20AC Corona Treater). The device was then baked at $100 \text{ }^\circ\text{C}$ on a hotplate for 2 hours. The inlet and outlet were created by a biopsy punch (diameter: 1 mm). Finally, acetone was injected into the nano-sieve channel to completely remove the positive photoresist, followed by deionized water cleaning.

5.2.5 *Microbeads stacking and characterization*

For each experiment, $30 \mu\text{L}$ of the silica magnetic microbeads ($\sim 7.6 \times 10^7$ beads/mL) were introduced into the nano-sieve channel by a syringe pump at a flow rate ranging from 20 to $60 \mu\text{L}/\text{min}$. A fluorescence microscope (AmScope, $10\times$) equipped with a high-speed camera (AxioCam MRc, Zeiss) was used to capture the microbeads pattern in the nano-sieve channel and the outlet reservoir.

5.2.6 *OCT scanning and processing*

Nano-sieve channels were imaged via an OCT system, which is a label-free, volumetric imaging modality with an axial resolution of $3 \mu\text{m}$ and a lateral resolution of $4 \mu\text{m}$, all in air. The field of view of OCT system is $3 \times 6 \times 1.94 \text{ mm}^3$. The imaging system utilizes a raster scanning pattern and works at a line rate of 25 kHz. To evaluate the topology of the nano-sieve channels, the volumetric dataset was processed by a K-

means clustering algorithm to segment the nano-sieve region from the background [204]. The maximum height and volume were measured in the segmented regions and grouped according to their flow rates.

5.2.7 Plasma separation and RBCs retrieval

Before on-chip experiments, whole blood sample containing RBCs was imaged with 20× magnification by a bright-field microscope (AmScope). For plasma separation, 5 μL whole blood was first diluted to 45 μL with 40 μL PBS buffer and then introduced into the nano-sieve channel with a flow rate of 5 $\mu\text{L}/\text{min}$. After plasma collection, a high flow rate (~ 900 $\mu\text{L}/\text{min}$) was applied to deform the nano-sieve and retrieve the microbeads and RBCs in a new Eppendorf tube. Finally, a neodymium magnet was used to isolate the microbeads and RBCs. The cell density of the retrieved sample was calculated by using the commercially available ImageJ program.

5.3 Experimental results

Our approach of separating human plasma from whole blood samples is presented in **Figure 5.1(a)**. The magnetic beads with a diameter of 10 μm were pumped into the nano-sieve channel to construct a 3-D microbeads array. Diluted whole blood was then injected into the microbeads-stacked nano-sieve for the separation process. The deformed PDMS slab holds the microbeads in the nano-sieve and cannot be removed with a flow rate under 60 $\mu\text{L}/\text{min}$. As shown in **Figure 5.1(b)**, patterned by standard microfabrication, several nano-sieve channels can be operated simultaneously for multiplexing plasma separation. The detailed procedure for plasma separation from whole blood is shown in **Figure 5.2**. Initially, the microbeads are packed within the nano-sieve channel with a specific flow rate

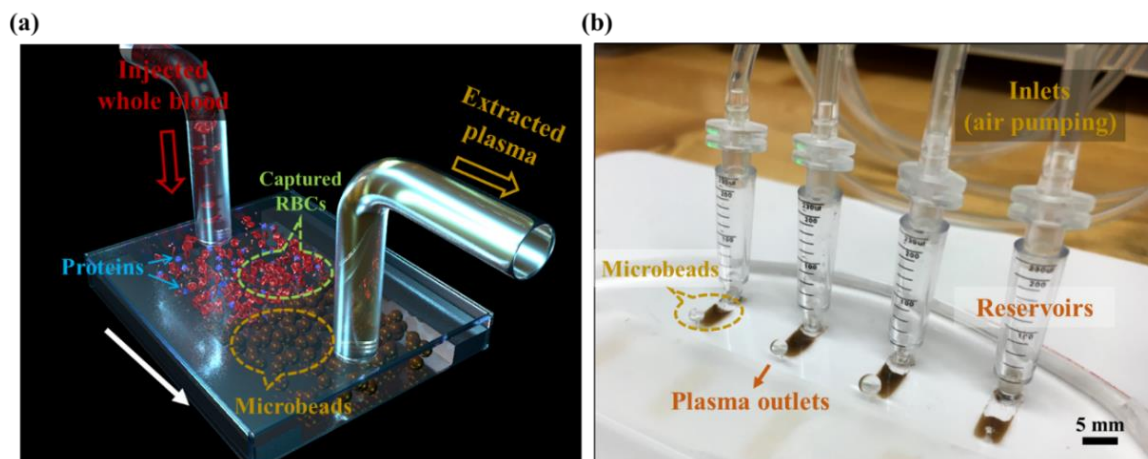


Figure 5.1 (a) Schematic of the microbeads packed nano-sieve device for the separation of blood cells and plasma. (b) Micrograph of the multiplexing nano-sieve system for plasma separation and RBCs retrieval. Reprinted from [205].

(**Figure 5.2(a)**). The diluted whole blood sample is injected into the microbeads-packed nano-sieve (**Figure 5.2(b)**) with a flow rate of $5 \mu\text{L}/\text{min}$. After collecting the extracted plasma, fresh PBS is introduced with a high flow rate to deform the nano-sieve and retrieve the RBCs and microbeads into a new Eppendorf tube (**Figure 5.2(c)**). Finally, an external magnet is used for separating the microbeads from the retrieving RBCs (**Figure 5.2(d)**).

To understand the microbeads patterning process and maximize the patterning capacity, we studied the microbeads patterning with both fluorescence microscope and OCT. As shown in **Figure 5.3**, for 1:5 PDMS samples, most of the microbeads are contained in the nano-sieve without leaking issues. At a low flow rate, the microbeads are pushed to the sides of the nano-sieve (**Figure 5.3(a-i)**) due to the pressure drop built in the nano-sieve channel [204]. Increasing the flow rate causes the microbeads to accumulate to the middle of the channel (**Figure 5.3(a-ii)** and **Figure 5.3(a-iii)**). Similarly, for 1:10 PDMS samples, the microbeads are distributed to the sides of the nano-sieve at a low flow rate (**Figure**

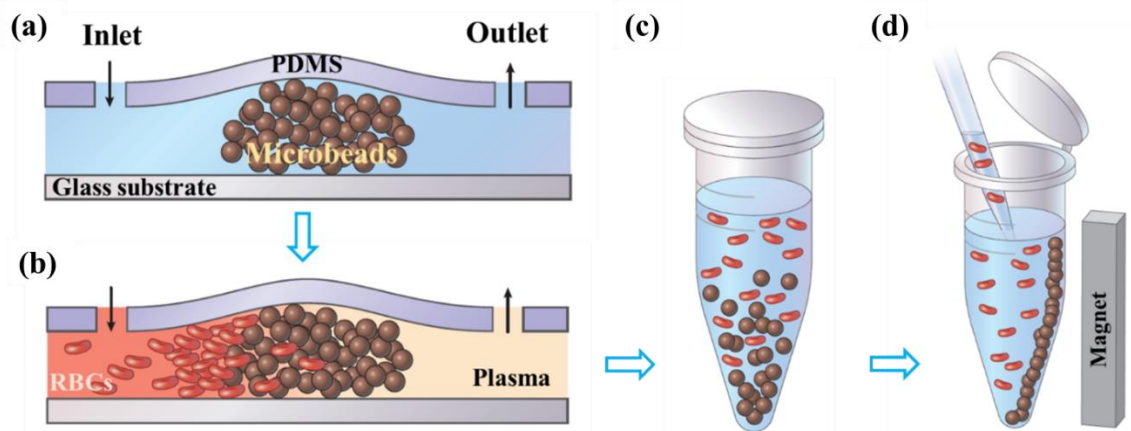


Figure 5.2 The experimental procedure for separating plasma and retrieving RBCs from whole blood. (a) Beads stacking in the channel; (b) RBCs separation; (c) RBCs and microbeads collection; (d) RBCs extraction. Reprinted from [205].

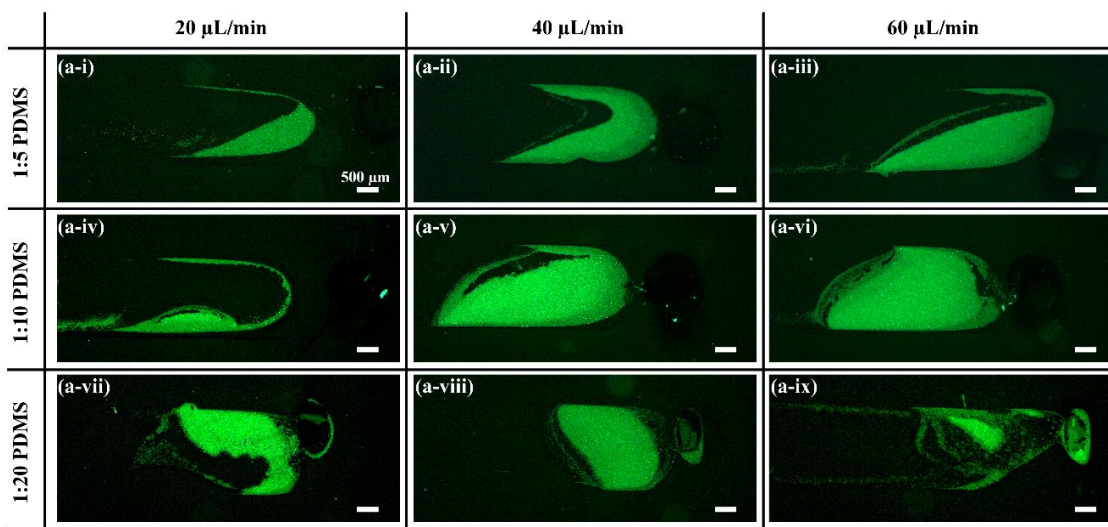


Figure 5.3 (a) Fluorescence microscope images of the packed microbeads in nano-sieve at various flow rates (20-60 $\mu\text{L}/\text{min}$) and PDMS curing agent/base ratio (1:5 to 1:20). Reprinted from [205].

5.3(a-iv)) and tend to accumulate to the middle of the channel at higher flow rates without leaking issues (**Figure 5.3(a-v)** and **Figure 5.3(a-vi)**). However, as for 1:20 PDMS samples, irregular patterns and significant microbeads leaking are observed even at a low flow rate (**Figure 5.3(a-vii)**). Increasing the flow rate results in severe amounts of microbeads leaking to the outlet reservoir (**Figure 5.3(a-viii)** and **Figure 5.3(a-ix)**). This

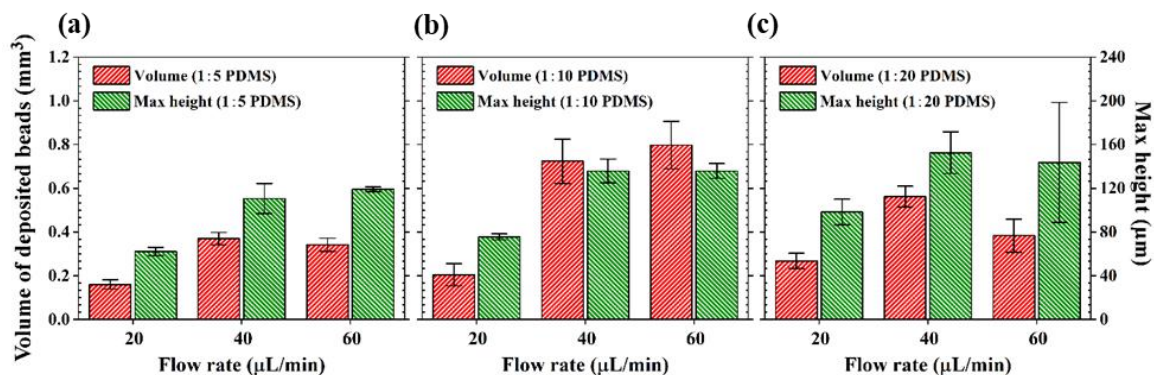


Figure 5.4 Measured volume and maximum height of the microbeads packed nano-sieve by OCT with curing agent/base ratio of: (a) 1:5; (b) 1:10; and (c) 1:20. Reprinted from [205].

observation agrees with the measurements from OCT scanning. As shown in **Figure 5.4(a)** and **Figure 5.4(b)**, a significant increase of volume and maximum height from 20 to 40 $\mu\text{L}/\text{min}$ are observed for both 1:5 and 1:10 PDMS samples. Further increasing the flow rate to 60 $\mu\text{L}/\text{min}$ does not increase the volume and maximum height, agreeing with the microscope images. The measured volume for 1:10 PDMS sample is ~ 2 times larger than 1:5 PDMS sample, indicating a larger cross-section plane for fluidic passage and more voids created by a larger volume of stacked beads. On the other hand, for 1:20 PDMS samples, a distinct drop in microbeads volume at a high flow rate of 60 $\mu\text{L}/\text{min}$ is observed, indicating a significant loss of microbeads (**Figure 5.4(c)**).

The measured hardness of 1:10 sample is slightly higher than the 1:5 sample and is ~ 2.5 times higher than the 1:20 sample, suggesting a significant drop of hardness when increasing the mixing ratio from 1:10 to 1:20, as shown in **Figure 5.5(a)**. Since the deformable nano-sieve device works within a small deformation range, we use the Shore hardness test to estimate the Young's modulus,

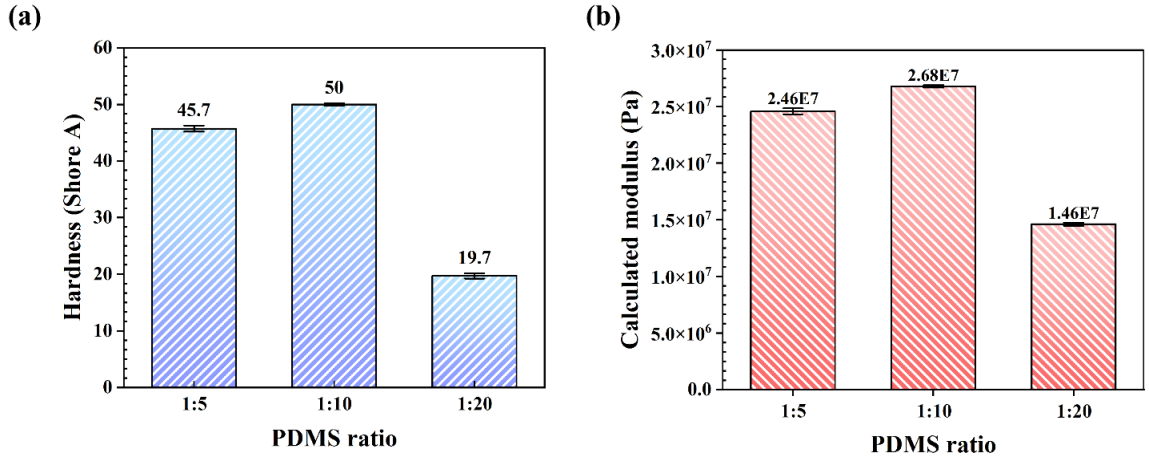


Figure 5.5 Measured mechanical properties of PDMS with a curing agent/base ratio ranging from 1:5 to 1:20: (a) Hardness. (b) Calculated elastic modulus. Reprinted from [205].

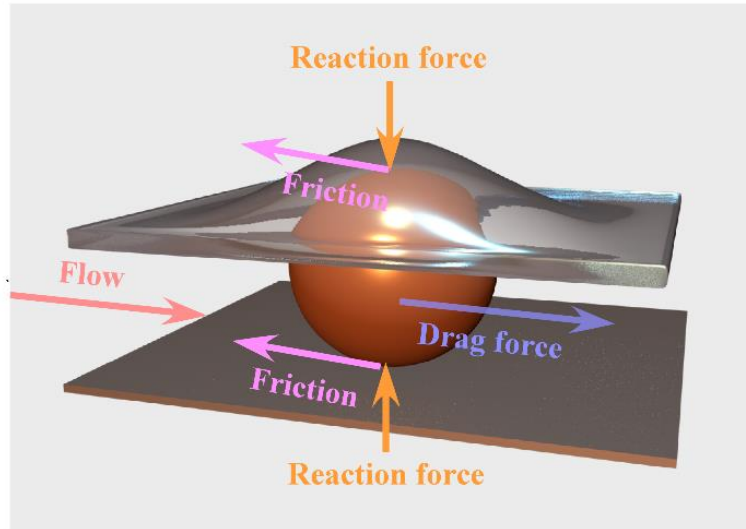


Figure 5.6 Force analysis of a single microbead sandwiched between two deformable surfaces. Reprinted from [205].

$$E = \left[\frac{S}{e^{100}} \right]^2 \quad (5.1)$$

where S is the Shore durometer and E is the Young's modulus [206]. The calculated modulus data is posted in **Figure 5.5(b)**.

With the mechanical properties, we then constructed a theoretical model to understand the microbeads trapping and leaking. The force balance of a single microbead under high flow rate through the channel is shown in **Figure 5.6**. The problem is simplified as a microsphere being trapped between two deformable surfaces. Reaction forces normal to the surfaces and toward the particles are applied at the level of

$$F_N = \frac{1}{3}E^*D^{\frac{1}{2}}(D - H)^{\frac{3}{2}} \quad (5.2)$$

where F_N is the reaction force in the normal direction

$$E^* = \frac{E}{2(1-\nu^2)} \quad (5.3)$$

E is the elastic modulus, ν is the Poisson's ratio, D is the microbead diameter, and H is the original height of the gap between two surfaces. The maximum possible friction force, F_R , is obtained using the formula

$$F_R = 2\mu F_N = \frac{2\mu}{3}E^*D^{\frac{1}{2}}(D - H)^{\frac{3}{2}} \quad (5.4)$$

where μ is the coefficient of friction. While the flow drags the sphere toward to the outlet, the drag force, F_D , is modeled using

$$F_D = 3\pi\rho\nu Du \quad (5.5)$$

where ρ is the density of the fluid, ν is the fluid viscosity, and the cross-section average flow velocity is

$$u = \frac{Q}{HWf(E^*)} \quad (5.6)$$

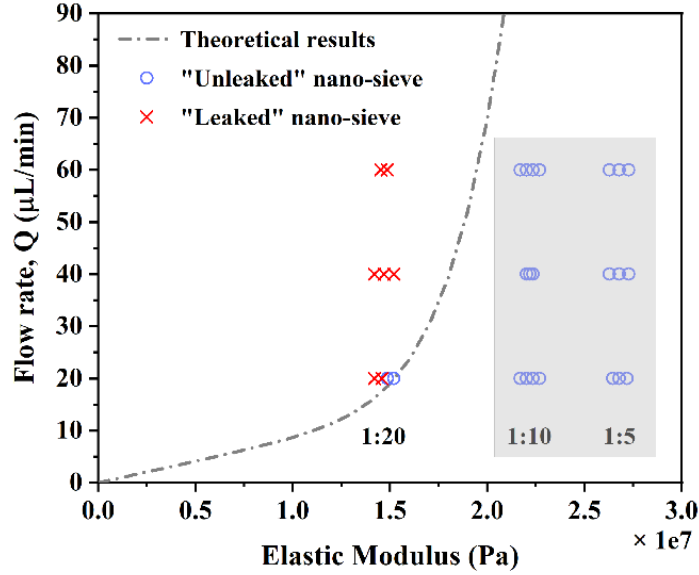


Figure 5.7 “Leaked” (red) versus “unleaked” nano-sieve (blue) at various flow rates observed under a fluorescence microscope. The grey dashed line is the “leaking” boundary based on the theoretical prediction, agreeing with the experimental results. Reprinted from [205].

which is a function of the total discharge Q , the gap height H before deformation, the gap width W , and the elastic modulus E . The function $f(E^*)$, indicating the ratio of the deformed cross-sectional area to the original, is incorporated to take account of the deformation of the channel. At the two extremes, if the Young’s modulus is infinitely large, the gap will be enlarged to the uniform height of particle diameter D , while if the material is infinitely soft, the gap will be the original height of H . Here, we use a fitting model,

$$f(E^*) = 1 + \left(\frac{D}{H} - 1\right)\{erf[S(E^* - E_0)] + 1\} \quad (5.7)$$

to capture the trend that the average gap height increases with greater elastic modulus transitioning from H to D . The error function is used to capture the transition with a fitting coefficient S and E_0 to match the deformation rate and flexibility. In this theoretical model, we thus hypothesize that microbeads will be leaked if the drag force is greater than the

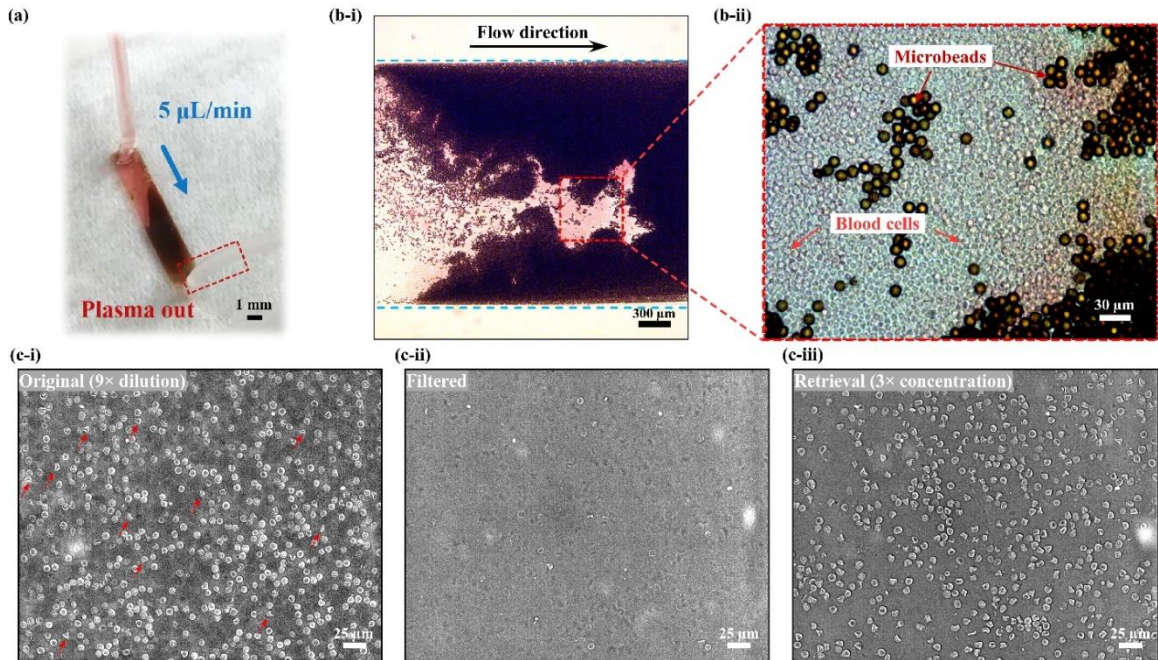


Figure 5.8 (a) Optical micrograph of a working nano-sieve for the isolation of plasma. The fluids at the outlet are more transparent as blood cells are removed. (b) Bright-field microscope image showing the microbeads pattern and captured RBCs: (i) low magnification; (ii) high magnification. (c) Microscope image of (i) original whole blood showing a high concentration of RBCs; (ii) Filtered plasma solution without RBCs. (iii) Retrieved RBCs from the nano-sieve. Reprinted from [205].

maximum friction ($F_D > F_R$) and no leakage occurs if the drag is less than the highest possible friction ($F_D < F_R$). With the fitting coefficients of $S = 10^{-7}$ and $E_0 = 3.3 \times 10^7$ Pa, the theoretical model can precisely predict the boundary (dashed line) between leakage and no leakage cases, as shown in **Figure 5.7** (“×”: leakage; “○”: no leakage). In addition, the current model explains the mixed results observed for 1:20 PDMS sample at a flow rate of 20 $\mu\text{L}/\text{min}$.

The 1:10 sample shows the highest hardness and most reliable capability of beads stacking, thus employed in the further study. The mechanical properties of PDMS may be further improved by doping with nanomaterials [207]. A micrograph of the separation

process is shown in **Figure 5.8 (a)**. The whole blood with a red color enters the nano-sieve and the RBCs are trapped by the microbeads array, allowing the human plasma to pass through the voids of the microbeads. The separated human plasma has a light-yellow color, as shown in the outlet tubing. **Figure 5.8(b)** shows the RBCs clogged nano-sieve under a bright-field microscope. The blood cells are randomly mixed with the microbeads in the nano-sieve and most of them are blocked at the microfluidic inlet. To characterize the plasma separation efficiency, the original blood sample and the filtered sample are shown in **Figure 5.8(c-i)** and **Figure 5.8(c-ii)**, respectively. The original sample has a high concentration of RBCs, including several cone shaped RBCs (red arrows). On the other hand, the filtered sample shows only a few individual cells, indicating a high plasma separation capability. As shown in **Figure 5.8(c-iii)**, by applying a $3\times$ on-chip concentration (input: $45\ \mu\text{L}$; retrieve: $15\ \mu\text{L}$), a cell density of $(4.5 \pm 0.37) \times 10^7$ cells/mL was achieved for the retrieved sample, which is comparable to the cell density of the original sample. Additionally, we observed more cone shaped RBCs in the retrieved sample, which may be caused by the highly confined beads array and the high flow rate during the separation process [208], [209].

5.4 Discussion

In this work, we experimentally measured the mechanical properties of PDMS with various mixing ratios. Combining with OCT scanning, we developed a computational fluidic system to understand how the mechanical properties of the deformable microfluidics and applied flow rate can affect the microbeads packing and leaking. This model successfully explains how the microbeads matrices are formed in the microfluidic channel, enhancing the overall performance of nano-sieve's plasma separation efficiency.

Efficient plasma separation [210], [211] is critical for numerous down-stream molecular analysis and diagnosis [180], [212]–[214]. The microbeads packed nano-sieve device is capable of plasma separation without using bulky and complicated instruments such as a centrifuge. Our design only requires a dilution factor of 1:9, which is much lower than the other reported microdevices for whole blood processing [196], [209]. In addition, we apply a 5 $\mu\text{L}/\text{min}$ flow rate for the plasma separation, which is ~ 10 -100 times faster than previously reported studies [198], [199]. Even though immunoassay-based RBCs removal strategy also demonstrates a high plasma separation efficiency [215], reagents such as antibodies are delicate and can degrade rapidly, making the device storage challenging in low resource settings. Our separation process solely relies on the silica microbeads stacking in a deformable microfluidic device and can be stored in ambient environment for a very long period of time, ideal for the sample preparation in POC settings.

This nano-sieve device can potentially be scaled up by increasing the channel width to reduce the pressure built in the channel. This will allow us to process a larger volume of diluted or undiluted whole blood. The decreased flow resistance will also allow a higher flow rate and faster processing time. Furthermore, ~ 100 individual nano-sieve devices can be patterned on a 150 mm wafer for multiplexing plasma separation, which is hard to achieve by membrane-based microfluidic devices [216].

We show that RBCs can be retrieved by simply increasing the flow rate and the deformation of the nano-sieve, which is superior to microstructure-based separation as the clogged RBCs cannot easily be removed from the functional structure [217]–[219]. The study of RBCs in patient sample can be used to understand and treat many bloodborne diseases such as sepsis [181], [182], sickle cell anemia [183], [184], and COVID-19 [220],

[221]. In the future, the geometry of each nano-sieve can be modulated to process a larger volume of blood sample for low concentration pathogen detection. Changing the size and spacing of the microbeads can also be used to separate and concentrate various types of cells and biomarkers, or even smaller particles such as viruses by packing nanospheres. For example, by varying the size of the packed microbeads, it is possible to separate leukocytes from the other two main components (erythrocytes and platelets) in whole blood due to the differences in size and deformability [222]. Furthermore, as the materials properties of the microbeads can be tuned, the nano-sieve can be used to study various cell mechanics problems [223], [224] with real-time microscopy imaging in a confined nano-environment.

Furthermore, our study is a meaningful attempt to test the fluid-structure interaction theory in the application of microfluidics from the viewpoint of structural and material properties [225]. The developed theoretical model can be used to guide the design of deformable microfluidics and the model closely resembling experimental results will inspire more detailed model development in the future.

5.5 Conclusion

We have successfully developed a deformable microfluidic system by packing the microbeads in a nano-sieve channel, which has been validated by fluorescence microscopy, OCT scanning, mechanical testing, and a theoretical computational fluidic model. Our plasma separation process does not require significant blood dilution and can process the blood sample in a rapid fashion. In addition, leveraging the deformation of the device, we show that the RBCs can be efficiently retrieved after the plasma separation. On the other hand, the theoretical model developed here can well predict the leaking of the microbeads at certain conditions and offer a guidance for the design of the next-generation separation

systems. In the future, computational fluidic dynamic modeling will be used to further understand the microbeads distribution in the nano-sieve. Our work holds a significant promise for the accurate assessment and diagnosis of bloodborne diseases at POC settings. Further study on scaling up the nano-sieve system with an enhanced capability of microbeads packing is under way to deal with a larger volume of blood without dilution for faster blood sample preparation.

**Chapter 6. Coupling a Molecular Diagnostics with Bacteria Concentration
by a Pneumatically-regulated Nano-sieve Device**

This chapter focuses on the development of microfluidic platform, i.e., nano-sieve, specifically designed for better securing the 3-D beads-stacked microstructure during the purification of antibiotic-resistant bacteria (e.g., MRSA) from whole blood, where red blood cells (RBCs) are firstly considered to be removed without losing the target bacteria. In this case, a fast and simple immunoassay was found to efficiently deplete the RBCs from bacteria-spiked blood samples. And the innovative pneumatic chamber was integrated onto the previous nano-sieve device for securing the beads stacking within the nano-sieve channel. The experimental results and validation studies were also conducted to assess the performance and feasibility of the developed microfluidic nano-sieve for processing the ARB purification from whole blood. By integrating with a molecular detection technique, i.e., RPA/CRISPR-Cas assay, a visible-based detection of a specific ARB can be achieved, and the detection limit is improved to identify MRSA with a concentration as low as $\sim 10^2$ CFU/mL.

6.1 Introduction

The global rise in antimicrobial-resistant bacteria (ARB) and their widespread dissemination pose a growing threat to human health. At present, antibiotic-resistant infections claim the lives of approximately 700,000 individuals annually on a global scale [226]. However, based on projected analyses, if no measures are taken to control antibiotic-resistant infections or develop new-generation antibiotics, the worldwide mortality rate could surge to 10 million per year by 2050 [17]. This alarming trend would result in a staggering economic loss of \$100 trillion each year [227]. Urgent action is imperative to curb antibiotic resistance and foster the development of innovative antibiotics to avert this potential crisis.

Among the multitude of ARB, Methicillin-resistant *Staphylococcus aureus* (MRSA) emerges as a notable pathogen that poses a significant and formidable challenge. A timely and accurate detection is of utmost importance, as it can facilitate the appropriate medical intervention, reduce the transmission of these pathogens, and minimize the risk of antimicrobial resistance. Typically, it is necessary to purify target bacteria, e.g., MRSA, from the given samples, such as whole blood. For example, the membrane-based method has been widely used for separating the bacteria owing to its simplicity, cost-efficiency, and rapidness [128]. However, it still remains a challenge when processing the blood sample, since the blood cells could clog the active membrane for the failure of bacteria separation. Another technical challenge is the retrieval of captured bacteria from the membrane with an extensive volume of iterative washing buffer, which would significantly dilute the retrieved samples with a lower concentration level [130], [216].

Alternatively, microfluidic platforms have been a dominant and reliable tool for ARB purification and concentration relying on various working mechanisms, such as inertial force [131], [132], hydrodynamics [133], [134], electrophoresis [135], [136], and acoustics [137], [138]. But these techniques strongly lean upon the complex design and fabrication process, or extra laboratory-based instruments, so that increasing delicate operations while applying this kind of microfluidic platform. Thus, there is a need to develop a simplified and direct fabrication process, while ensuring the functionality of this microfluidic platform to effectively separate the target bacteria. Moreover, microfluidic platforms can be seamlessly integrated with downstream analysis techniques, such as PCR and CRISPR-Cas assay, leading to a rapid and direct analysis of those purified bacteria.

The current diagnostic workflow for ARB is based on blood culture [14], which is labor-intensive and time-consuming. Molecular detections, e.g., polymerase chain reaction (PCR) require precise thermal cycles and advanced bulky equipment, which limit them for resource-limited point-of-care (POC) settings. CRISPR-Cas systems have been well established in the field of a highly specific and rapid diagnosis [58], [60], [228]–[230]. Among them, Cas12a is solely based on a complementary crRNA for targeting specific DNA sequences and uses a single domain of RuvC to cleave a target DNA [231]. Moreover, Cas12a features the collateral activity, allowing it to non-specifically cut neighboring single-stranded DNAs (ssDNA) after target binding [232]. To utilize this feature for target detection, ssDNA can be technically modified by adding a fluorophore-quencher. Once Cas12a is activated after target binding, the cleavage of ssDNA triggers the appearance of fluorescence signal [233]. CRISPR-Cas12a system can be applied at a temperature of 37 °C [234], [235], enabling it more suitable for POC detection compared to traditional PCR

assay. In addition, by combining the CRISPR-Cas system with an isothermal amplification approach, such as recombinase polymerase amplification (RPA) [236], rolling circle amplification (RCA) [237], or loop-mediated isothermal amplification (LAMP) [238], the specificity and sensitivity of CRISPR-Cas detection can be further improved in POC environments [239]. Notably, RPA could be an outstanding candidate to be compatible with the same temperature requirements as CRISPR assays, due to its rapidity and simplicity [240], [241].

In this study, a pneumatically-regulated multiplexed nano-sieve device collaborated with an immunomagnetic assay was introduced for efficiently purifying and highly concentrating the target bacteria directly from blood samples. The obtained bacteria were then identified by applying RPA/CRISPR-Cas assay for a visual-based detection. Exploiting the deformable characteristics of nano-sieve channel, an impressive concentration of ~15-fold has been reached by tuning the volume ratio of initial sample solution and retrieved bacteria solution, leading to an improvement in detection limit down to ~100 CFU/mL for a positive detection of MRSA. Importantly, this optimized approach can process the purification and detection of target bacteria, only within 4 hours under body temperature and room temperature, compared to time-consuming process based on current diagnostic workflow [14]. Therefore, coupling a rapid and precise molecular detection with the multi-channels purification could be a promising method for enhancing the sensitivity and specificity of MRSA detection.

6.2 Materials and methods

Polydimethylsiloxane (PDMS, Sylgard[®]184) was obtained from Krayden Inc., CO, USA. Glass wafer (D263, thickness: 550 μm) was purchased from University Wafer, MA, USA.

Silica magnetic beads (diameter: 5 μm and 10 μm , 10 mg/mL, 10 mL) were received from Alpha Nanotech Inc., Vancouver, Canada. Phosphate buffered saline (PBS) solution (1 \times without calcium and magnesium, pH 7.4 ± 0.1) was ordered from Corning Inc., NY, USA. Fresh human blood with EDTA was obtained from *STEMCELL* Technology Inc., Vancouver, Canada. The EasySep™ RBCs depletion reagent was purchased from *STEMCELL* Technology Inc., Vancouver, Canada.

6.2.1 Device fabrication

The innovation of fabricating an extremely thin nano-sieve channel, while preventing the collapse of PDMS roof, was reported in the previous study [99], [204]. In this study, the pneumatically-controlled nano-sieve consists of a channel-patterned glass substrate and a pneumatic-based PDMS topping. Briefly, a cleaned 6-inch glass wafer (University wafer, D263, 550 μm , double side polished) was coated by a thin layer of TEOS (PECVD, AME P5000) in a thickness of 200 nm. After spin-coating a 1 μm thick of positive photoresist (AZ Mir 701), a plastic photomask (Fineline Imaging, CO, USA) was used to pattern the channel onto the photoresist layer. After the buffer oxide etching (BOE), the nano-sieve channel was generated on the glass wafer. To fabricate a pneumatic chamber with the height of 2 mm and the width of 2 mm, a PDMS mixture (SYLGARD™ 184, Krayden Inc., CO, USA) with a 1:10 ratio of curing agent and base polymer was poured into a three-dimensional (3-D) printed mold (Fictiv, CA, USA). Followed by the PDMS curing process in an oven at 60 °C overnight, the cured PDMS chamber layer was punched by a 1 mm puncher (INTEGRA™ Miltex™), for the pneumatic manipulation by the air pump (Precigenome LLC, CA, USA). Then this chamber layer and a cured PDMS thin film (~200 μm thick) were bonded by the plasma

treatment (Electro-Technic Products, IL, USA). Then the bonded device was baked on a hot plate at 100 °C for 2 hours, to obtain a strong bonding. To finalize the functional device, the nano-sieve channels was sealed by the pneumatic layer via the plasma bonding process and baking process. Before using this device for running experiments, the inlet and outlet holes for each channel were punched by a 1 mm puncher, aiming to the connection between the device and the sample sources from a syringe (BD 1 mL, NJ, USA), through the microfluidic tubing (Scientific Commodities, Inc., BB31695-PE/3).

6.2.2 *Beads stacking deposition*

A strategy of creating the 3-D microstructure of stacked beads was applied to physically capture the target bacteria from the initial sample. In this study, the nano-sieve channel was first rinsed and cleaned by IPA solution. Before introducing the magnetic beads into the channel, the air pump was used for ensuring the pressure applied in the pneumatic layer consistently at 12 Psi. Then, a 50 µL of 10 µm magnetic beads (10 mg/mL, 1:5 dilution) was injected into the channel to form a “coarse filter” by employing a syringe pump with a flow rate of flow rate of 30 µL/min. The injection of another 50 µL of 5 µm magnetic beads (10 mg/mL, 1:5 dilution) into the channel was followed, to form a “fine filter” under a flow rate of 20 µL/min. Finally, this functionalized nano-sieve device is ready for separating the target bacteria from the introduced sample solution.

6.2.3 *Bacterial culture*

Methicillin-resistant *Staphylococcus aureus* (MRSA, ATCC 43300) was purchased from Fisher Scientific. Kanamycin-resistant *E. coli* 10798 was obtained from lab stock.

The bacteria were cultured in tryptic soy broth medium (MilliporeSigma) and maintained on the tryptic soy agar plate. After the overnight culture at 37 °C under 200 rpm in a shaker, 1 mL of bacterial solution was extracted and centrifuged at 8000 g for 5 minutes to form a complete pellet. The spin-down bacteria were resuspended in 1 mL of PBS for the further use. This process was repeated twice to completely remove culture media. The concentration of the bacterial cells was determined by counting the colony-forming unit (CFU) on standard TSA plates.

6.2.4 *Bacteria staining*

A 2 µL working solution of *BacLight* green dye (Thermo Fisher Scientific) was mixed with 1 mL PBS-based bacteria solution, and the mixture was incubated at room temperature for 20 mins by following the manufacturer's instruction. Then the solution was centrifuged at 8000 g for 5 minutes to discard the PBS that consists of extra dye. The bacteria were resuspended in 1 mL fresh PBS for the further use.

6.2.5 *RBCs depletion immunoassay*

A rapid and efficient immunomagnetic assay was chosen for removing RBCs from the bacteria-spiked blood sample. Briefly, the prepared bacteria solution with a desired concentration was first spiked into the whole blood. The bacteria-spiked whole blood (1000 µL) with 12 µL of Ethylene-diaminetetraacetic acid (EDTA) was reacted with 50 µL RBCs depletion reagent (STEMCELL Technologies Inc. EasySep™) in a 1.5 mL Eppendorf tube. The mixed sample was placed on the magnetic rack for the incubation for 5 minutes at room temperature, aiming to remove most of RBCs from the original sample. The supernatant was then transferred to a new 1.5 mL Eppendorf tube, and reacted with another 50 µL RBCs depletion reagent. The whole sample was

placed on the magnetic rack for 5 minutes at room temperature again, to further remove the RBCs remaining in the original sample. The supernatant was finally transferred to a new 1.5 mL tube that was placed on the magnetic rack for 5 minutes at room temperature, to obtain a clear plasma solution for further experiments.

6.2.6 *Bacteria capture and concentration*

The 600 μL of prepared sample solutions, in which the bacteria with a certain concentration were spiked in 1:4 diluted plasma solution, were first loaded into several 1 mm sterile syringes. A multi-channel syringe pump was used to simultaneously inject the sample solutions into the functionalized nano-sieve channels through the microfluidic tubing, under a flow rate of 4 $\mu\text{L}/\text{min}$. After the separation process, the pneumatic pressure was terminated. Then a 30 μL of fresh phosphate buffer saline (PBS) solution was employed for washing the whole channel to retrieve magnetic beads and the captured bacteria out to the collection tube. An external magnet was used for a simply and directly extracting the bacteria-involved PBS solution, available for the further RPA/CRISPR-Cas detection. The concentration factor in this case is predicted to be 20-fold.

6.2.7 *Fluorescence microscopy imaging*

With the completion of bacteria separation, 10 μL of each retrieved samples and initial samples were dropped onto a glass slide for measuring cell density. A high-speed camera equipped onto the fluorescence microscopy was used to capture the fluorescent images, which was then analyzed by using Leica LAS X software.

Table 6.1 List of synthetic oligos sequence used in this study.

Name	Sequence (5'-3')
crRNA 1	UAAUUUCUACUAAGUGUGAGAUAGUUCUGCAGUACCGGAUUUG
Target 1	CAAATCCGGTACTGCAGAACT
F1	GATTAACCCAGTACAGATCCTTTCAATCTA
R1	ATAGCCATCATCATGTTTGGATTATCTTTATC
F2	TATGCAACAAGTCGTAAATAAAACACATAAAG
R2	TCATATGATATAAACCACCCAATTTGTCTGCC
crRNA 2	UAAUUUCUACUAAGUGUGAGUAGUAGCAGCUCGAAUUAG
Target 2	CTAGAGTAGCACTCGAATTAG
F3	AAACAAGCAATAGAATCATCAGATAACATTT
R3	TATAGATTGAAAGGATCTGTACTGGGTTAAT
F4	AAACAAGCAATAGAATCATCAGATAACATTT
R4	AAGGATCTGTACTGGGTTAATCAGTATTTTC
ssDNA-FQ Probe	/56-FAM/TTATT/3IABkFQ

6.2.8 *Nucleic acid preparation*

The bacterial lysis and DNA purification were proceeded at room temperature within 30 minutes. The lysozyme (Thermo Fisher) was added with a concentration of 20 mg/mL, to make a lysis buffer (20 mM Tris-HCl, 2 mM EDTA, and 1.2% Triton X-100). Then the enzymatic lysis buffer (18 μ L) was added to the bacteria solution (10 μ L) and the mixture was incubated for 10 minutes. Next, 2 μ L of proteinase K (Thermo Fisher) was added and incubated for 5 minutes. As for DNA purification, the protocol was slightly modified from the manufacturer's instruction. AMPure XP beads (Beckman Coulter) were mixed with the lysate and incubated for 5 minutes. The magnet was used to separate the beads from the mixture in 2 minutes. 70 μ L of 5 M

Guanidinium chloride (MilliporeSigma) was subsequently added to wash the beads twice, followed by the DNA elution with 20 μ L of nuclease-free water (Thermo Fisher).

6.2.9 RPA amplification and CRISPR-Cas12a detection

TwistAmp® Basic kit was obtained from TwistDx™. The RPA primers, crRNA, AsCas12a, and fluorophore–quencher probes were purchased from Integrated DNA Technologies, and detailed information on the synthetic oligonucleotides are listed in **Table 6.1**. The RPA primer sets were designed using PrimerQuest™ Tool. NEBuffer™ r2.1 was purchased from New England Biolabs.

By following the manufacturer's instruction, A mixture of 29.5 μ L of rehydration buffer, 11.2 μ L of nuclease-free water, and 2.4 μ L each of forward and reverse primers (10 μ M) were added to the enzyme pellet, then mixing with 2 μ L of purified DNA and 2.5 μ L of MgOAc (280 mM) to reach a total volume of 50 μ L, followed by the incubation at 37 °C for 20 minutes. After the incubation, 2 μ L of RPA amplicons were added to a pre-assembled CRISPR-Cas12a mixture consisting of 50 nM of AsCas12a, 62.5 nM of crRNA , 10 \times buffer, and 2.5 μ M of ssDNA-FQ probe, finally leading to a reaction volume of 20 μ L. This reaction solution was incubated at 37 °C in 30 min. After the incubation, the mixture was excited under a blue light (excitation wavelength at 465 nm) from the transilluminator (SmartBlue, NEB-E4100) for a naked-eye observation. Finally, 20 μ L of nuclease-free water was added to 5 μ L of the mixture, which was then characterized by the imaging reader (Agilent BioTek Cytation 5).

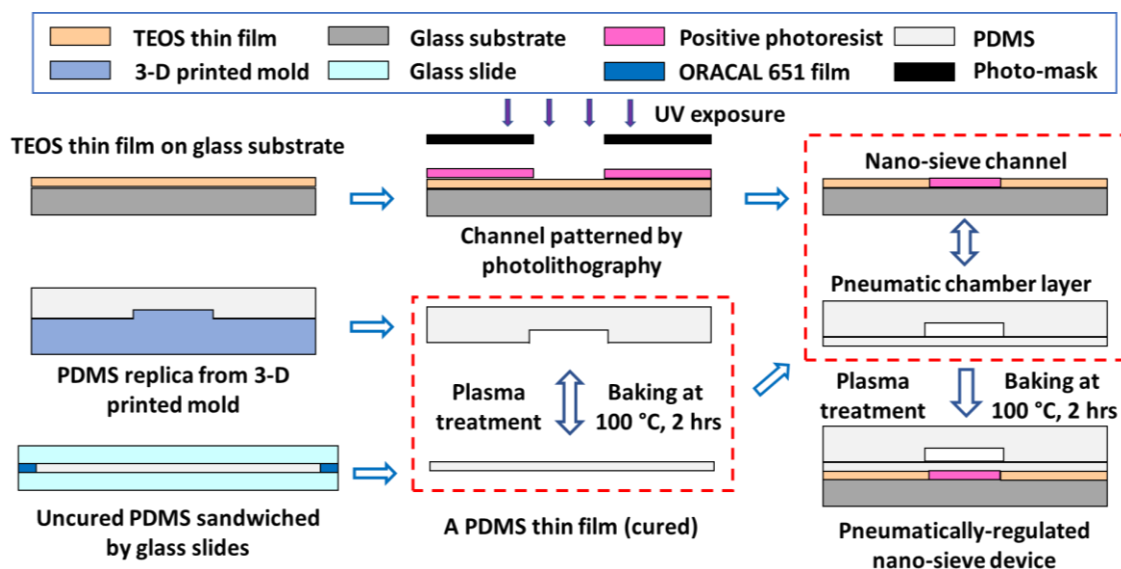


Figure 6.1 The process flow of fabricating a pneumatically-controlled nano-sieve device, including the creation of nano-sieve channel (*Top row*), the PDMS pneumatic chamber (*Middle row*), and a PDMS thin film (*Bottom row*).

6.3 Results and Discussion

In this study, we developed a pneumatically regulated nano-sieve device, incorporating with RPA/CRISPR-Cas method, for rapidly purifying and efficiently identifying the target bacteria (e.g., MRSA) from whole blood samples. As shown in **Figure 6.1**, the fabrication flow starts with a 200 nm thick layer of TEOS deposition onto a pre-cleaned glass wafer. Followed by spin-coating a layer of positive photoresist, a pattern of nano-sieve channel was defined onto the photoresist layer by photolithography technique, then transferred onto the TEOS layer by BOE process. The patterned channel was created, finally covered by a thin layer of positive photoresist as a sacrificial support for PDMS-glass bonding. This coated photoresist can completely eliminate the PDMS roof collapsing, significantly optimizing the fabrication of nano-fluidic channels. On the other hand, the pneumatic chamber was fabricated by using a 3-D printed mold. The uncured PDMS was sandwiched

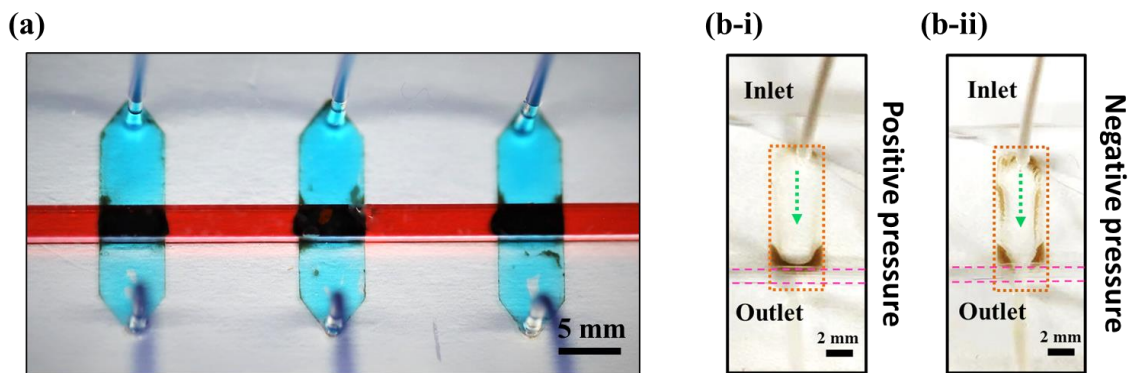


Figure 6.2 (a) The optical picture of an experimental multi-channel nano-sieve device filled with food dye. (b) The stacked beads array secured by the pneumatic layer with positive pressure (b-i) and the beads released by the pneumatic layer with negative pressure.

by glass slides to form a thin film, of which the thickness was determined by a support material of ORACAL film and was cured by baking it in the oven. Next, the pneumatic chamber and the cured PDMS thin film were bonded via the plasma treatment. The entire nano-sieve channels were completely sealed by bonding the pneumatic chamber layer and the patterned glass substrate via the plasma treatment. Both treatments (marked by the red dashed rectangles) were followed by the baking process on the hot plate to achieve the strong bonding in between.

In **Figure 6.2(a)**, a practical nano-sieve device was filled with blue food dye to present the multiple channels and red food dye to show the pneumatic layer, respectively, indicating the successfully sealed channel and pneumatic chamber. During the experimental tests, the magnetic beads were injected into the nano-sieve channel under the positive pneumatic pressure, so that realizing the well-established beads array within the channel for higher capture efficiency (**Figure 6.2(b-i)**). On the contrary, the beads release can be easily achieved under the negative pneumatic pressure (**Figure 6.2(b-ii)**).

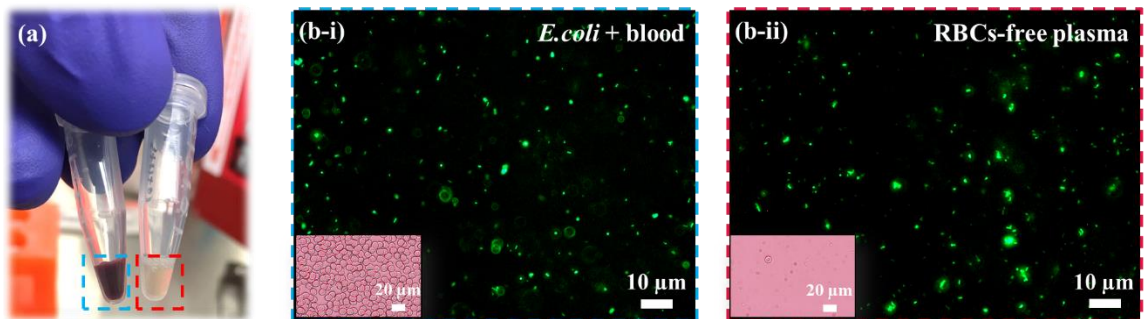


Figure 6.3 (a) Optical picture of *E.coli*-spiked whole blood before (left tube) and after (right tube) RBCs removal. (b) Fluorescence of the spiked bacteria before (b-i) and after (b-ii) removing RBCs from whole blood. The inserts show the comparison of RBCs density accordingly.

To verify that the RBCs depletion assay is specific to RBCs, the stained *E. coli* with a high concentration of 4.6×10^7 CFU/mL was spiked into whole blood and mixed with RBCs depletion reagent. After incubation, the red blood cells (RBCs) in bacteria-spiked blood sample were depleted with a solid phase immunoassay, thus obtaining plasma solution as shown in **Figure 6.3(a)**. The color of sample changed from red to light-amber color, indicating the successful removal of the RBCs. Then the fluorescence microscopy was used to image the stained bacteria that presented the green fluorescent signal. In **Figure 6.3(b-i)**, the bacteria concentration almost remained at a similar level after the procedure of RBCs depletion (**Figure 6.3(b-ii)**). Additionally, the inserts show that most of the RBCs are depleted during this process, which further confirmed only RBCs were specifically removed but spiked-bacteria were survived as expected.

After receiving RBCs-free *E.coli*-spiked plasma sample with a high concentration of 4.6×10^7 CFU/mL, a single channel of beads-stacked nano-sieve was applied for the bacteria purification under a slow flow rate of $1 \mu\text{L}/\text{min}$. As presented in **Figure 6.4**, the concentrated bacteria show very strong fluorescent signal under the fluorescent microscope, suggesting that most of the bacteria are trapped by microbeads stacking nano-sieve device

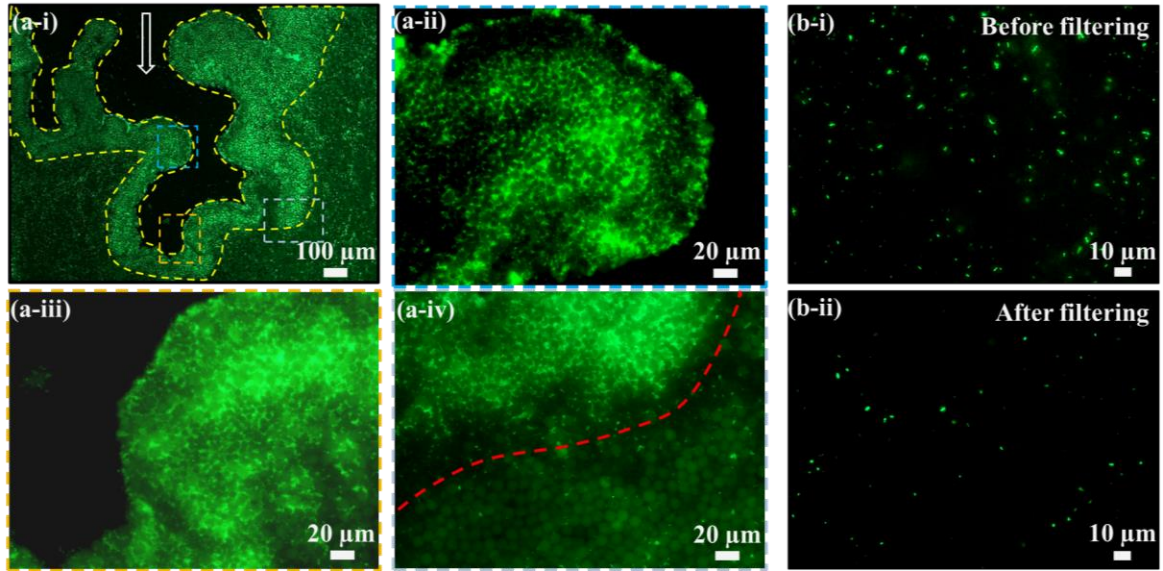


Figure 6.4 (a) Distribution of trapped bacteria under various low magnifications. The white arrow indicates the flow direction, and the yellow dashed line shows the region of 5 μm microbeads. The red dashed line is the interface of different sizes of microbeads. (b) Bacteria density before (b-i) and after (b-ii) nano-sieve filtering.

(**Figure 6.4(a-ii)** and **Figure 6.4(a-iii)**). By investigating the interface between 5 μm microbeads and 10 μm microbeads, it is noted that the smaller microbeads offer narrower voids among them to capture most of bacteria within the channel as expected. A trapping efficiency of 72.3% ($\pm 3.2\%$) is achieved by comparing the density of bacteria before (**Figure 6.4(b-i)**) and after (**Figure 6.4(b-ii)**) the capture procedure. Therefore, this pneumatically-regulated nano-sieve system with a mixture of various sized beads enables the desired capture for target bacteria from the pure and non-diluted blood sample.

Under the condition of dynamic microfluidics, the RBCs-free bacteria sample with a lower concentration of $\sim 10^5$ CFU/mL were clearly observed to reveal the dynamic on-chip enrichment of target bacteria, by continuously captured by the microbeads-stacked filtering system, as presented in **Figure 6.5**. The time-lapse images indicate the increased number of MRSA bacteria over time. At the time of 30 minutes, the distribution of captured MRSA

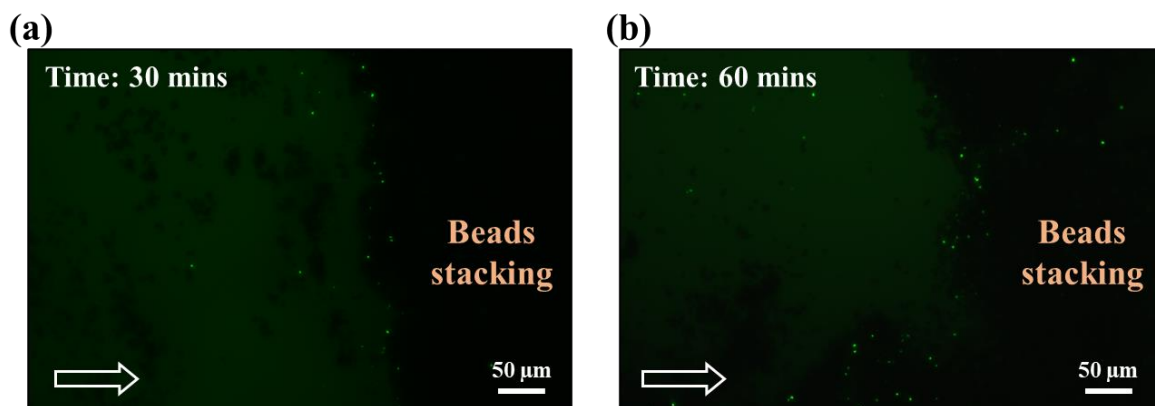


Figure 6.5 The time-lapse fluorescent images display the distribution of MRSA bacteria under the dynamic processing at the time of 30 minutes (a) and 60 minutes (b). The white arrow shows the flow direction. The green dots represent the MRSA bacteria stained by green dye.

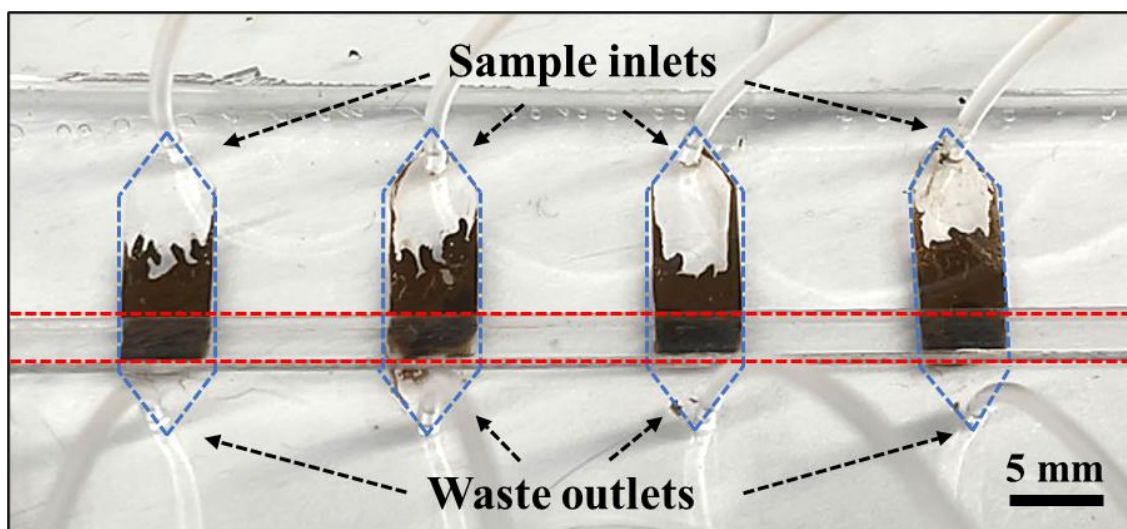


Figure 6.6 The optical picture of multi-channels (blue dashed lines) nano-sieve device with a pneumatically-controlled layer (red dashed lines). Each channel has a magnetic beads array with various size of 5 μm and 10 μm in order.

bacteria were monitored by a high-speed camera cooperated with the fluorescence microscopy. The target bacteria were moving from the inlet toward the array of magnetic beads, eventually confined by the voids between those beads (**Figure 6.5(a)**). As the purification process continues toward the time of 60 minutes, more target bacteria were

Table 6.2 Concentration factor after the bacterial retrieval by nano-sieve device.

Channel #	Inlet Concentration (CFU/mL)	Outlet Concentration (CFU/mL)	Experimental Concentration Factor	Theoretical Concentration Factor
1	4.00×10^2	$(6.00 \pm 2.94) \times 10^4$	15.00	20.00
2	5.93×10^3	$(8.47 \pm 1.07) \times 10^4$	14.27	20.00
3	7.43×10^4	$(8.37 \pm 1.40) \times 10^5$	11.26	20.00
4	3.43×10^5	$(4.07 \pm 0.60) \times 10^6$	11.84	20.00
5	3.80×10^6	$(4.07 \pm 0.60) \times 10^7$	10.79	20.00

captured by the beads array as shown in (**Figure 6.5(b)**). It is also observed that some bacteria were moving further towards the outlet area, but still confined by the voids between beads in a large volume of beads stacking (**Figure 6.6**). Therefore, it is noted that the target bacteria can be efficiently captured by this reliable pneumatically-regulated nano-sieve, to significantly minimize the bacterial leaking.

To evaluate the concentration factors after the retrieval process, the multi-channels of the developed nano-sieve device, as shown in **Figure 6.6**, were employed to purify and concentrate the RBCs-free MRSA samples with various concentrations from 10^6 to 10^2 CFU/mL (**Table 6.2**). As described, the $10 \mu\text{m}$ magnetic beads were first pumped into the cleaned channel under a flow rate of $30 \mu\text{L}/\text{min}$, while the pneumatic layer is active for securing the beads structure and preventing the beads leaking. Next, the $5 \mu\text{m}$ magnetic beads was injected into the channel and closely approaching to $10 \mu\text{m}$ beads-stacking to

Bacterial lysis and DNA Purification

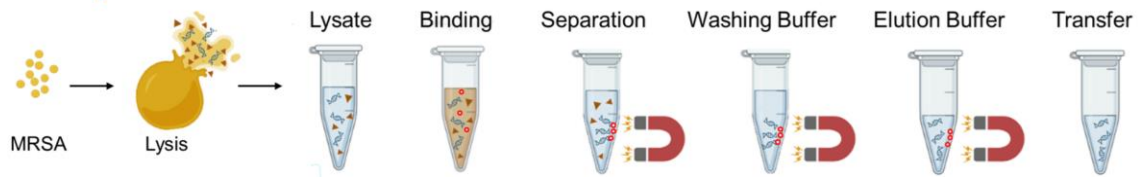


Figure 6.7 The procedure of bacterial lysis and DNA purification by using the functional magnetic beads.

generate a dual-layer filtering system, which can significantly improve the capture efficiency when dealing with the small size of bacteria in our case [99]. The separated fluids can be collected from the waste outlets, and the captured MRSA bacteria can be obtained for the evaluation of concentration factors regarding a series of samples with the concentration from high to low level.

Following the successful concentration of MRSA from multiplexing nano-sieve device, we employed the standard plate count method to assess the concentration capability of the device. **Table 6.2** presents the achieved concentration factors for various inlet concentrations using the nano-sieve device. The concentration factor was determined by dividing the inlet concentration by the outlet concentration. We introduced a total of 600 μL of MRSA sample solution into the nano-sieve channel, while 30 μL of PBS was used to retrieve the MRSA bacteria, resulting in a theoretical concentration factor of 20. However, as the MRSA concentration increased. The experimental concentration factor showed a slight decreasing trend. One possible explanation for this is that at higher MRSA concentration, some bacteria might have leaked out through the waste outlets. This suggests that the nano-sieve is more suitable for concentrating low-concentration bacteria sample, aligning with our objective of enhancing the detection limit.

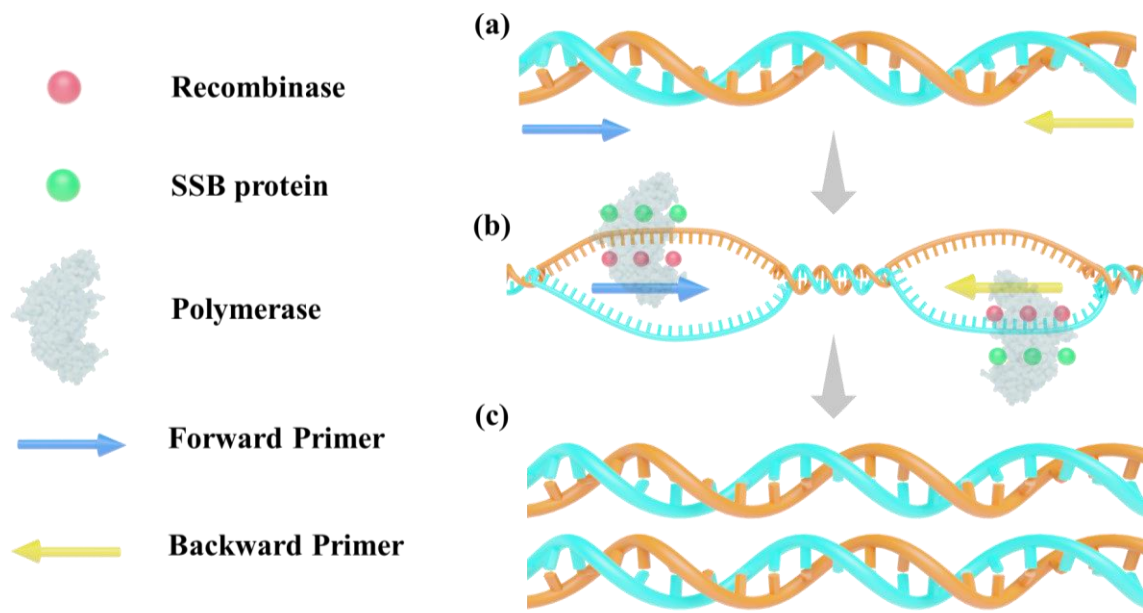


Figure 6.8 The schematic presents the mechanism of RPA amplification process, including (a) primers binding; (b) recombinase-mediated strand displacement and Primer extension; (c) amplification and strand displacement.

To determine the on-chip detection limit by using RPA/CRISPR-Cas, the captured MRSA bacteria were highly retrieved from the nano-sieve channel under the negative pneumatic pressure, by applying a small volume of fresh PBS buffer. Then MRSA bacteria lysis and DNA purification, as shown in **Figure 6.7**, was executed to obtain the target DNA from bacteria for the further RPA/CRISPR-Cas assay. Briefly, the lysate comprising the DNA from MRSA bacteria was reacted with the introduced magnetic beads, so that DNA molecules binding onto the surface of beads through electrostatic interactions and molecular crowding. After trapping the DNA-bound magnetic beads by using external magnet, the proteins and membrane debris were efficiently separated and removed. By washing the DNA with guanidinium chloride to solubilize the DNA-protein interactions, the purified DNA was eluted by using nuclease-free water. The RPA procedure (**Figure 6.8**) was followed to achieve isothermal amplification of the target DNA, based on the

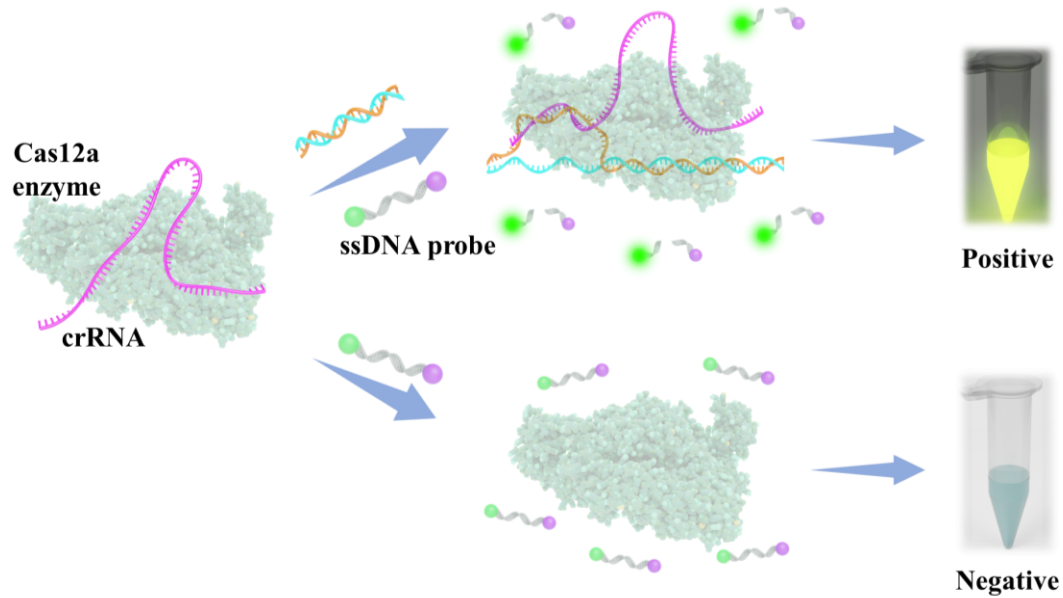


Figure 6.9 The schematic shows the mechanism of CRISPR-Cas12a system to cleave the target DNA and ssDNA with fluorophore-quencher molecules for a visual detection. The ssDNA probe is linked with fluorophore-quencher molecules. The crRNA means a guided RNA that is designed to be complementary for the target DNA sequence.

activities among the single-stranded DNA-binding (SSB) proteins, DNA polymerases, and recombinases. This process starts with primer binding that specifically recognizes and binds to the target DNA sequences. A recombinase enzyme then facilitates the strand displacement of the double-stranded DNA, to create a displacement loop structure. Subsequently, DNA polymerase enzyme starts to synthesize a complementary DNA strand using the displaced target strand as a template. As the primer extension proceeds, the displaced strand from the target continues to form new displacement loops, eventually leading to the amplification by synthesizing new DNA strands. After introducing RPA amplicons into the CRISPR-Cas12 system, as shown in **Figure 6.9**, in a positive sample, when the Cas12-crRNA complex reacts with the complementary target DNA, the nuclease activity can be activated, enabling the DNA targeting and editing. Once a sequence that matches the crRNA is found, the Cas12 protein binds to the target DNA sequence at a

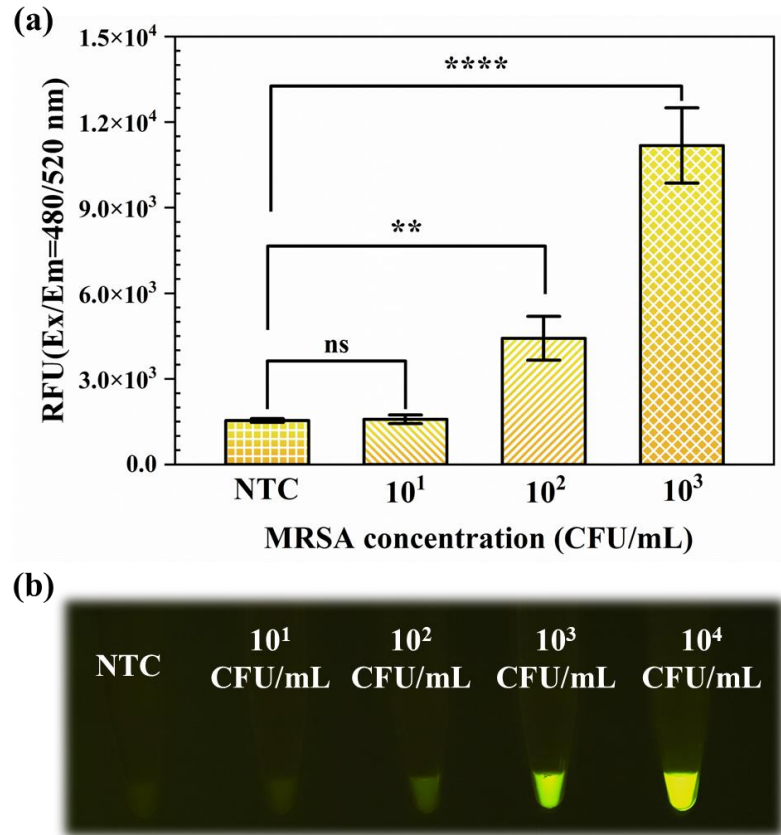


Figure 6.10 (a) The quantitative data plotted by introducing the fluorescence intensity versus various bacterial concentration from 10^3 to 10^1 CFU/mL. "NTC" refers to no template control. The data are represented as mean \pm standard deviation (n=3). For statistical analysis, ns, not significant = $p > 0.05$; * = $0.01 < p \leq 0.05$; ** = $0.001 < p \leq 0.01$; **** = $p \leq 0.0001$. (b) The endpoint image displays the visual detection by presenting the yellow-green fluorescence signal under the ultraviolet light.

specific site, as well as cleaving nearby non-target DNA strands (i.e., ssDNA exhibited in **Figure 6.9**) by a collateral cleavage activity. Therefore, the fluorescent signal from the fluorophore separated from the quencher is released and can be visualized by naked eye under the ultraviolet (UV) light. In a negative sample, the nuclease activity of Cas12a remains inactivated due to the absence of ssDNA, preventing the release of fluorophore from the probe linked with fluorophore-quencher molecule. So there is no fluorescence signal detected from the negative sample as shown in **Figure 6.9**.

After the multiplexing purification of the initial MRSA bacteria samples with various concentration from 10^3 to 10 CFU/mL, the RPA/CRISPR-Cas assay, as described above (**Figure 6.7, Figure 6.8, and Figure 6.9**), was applied for identifying those retrieved bacteria from the nano-sieve by quantitatively measuring fluorescence intensity using the plate reader and visually detecting the fluorescence signal using a transilluminator at the excitation wavelength of 465 nm. As seen in **Figure 6.10(a)**, the measured fluorescence intensities related to the no template control (NTC) and various bacterial concentrations in this case were plotted, corresponding to the endpoint images displaying the naked-eye results. The difference among the bacterial samples can be realized by employing one-way analysis of variance (ANOVA) analysis, compared with NTC sample. In **Figure 6.10(b)**, the positive sample can be easily differentiated from the negative groups by naked-eye from the concentration of 10^4 to 10 CFU/mL. It is stated that our experimental setup by integrating the pneumatically controlled nano-sieve with RPA/CRISPR-Cas assay achieved the detection limit of initial bacterial blood sample down to ~ 100 CFU/mL.

6.4 Discussion

The approach based on rapid purification and high concentration of pathogens from a large volume of bodily fluids would be critical to diagnose diseases, such as sepsis, at the early stage [137], [242]. By comparing with the surface chemistry technique, isolating pathogens by applying microfluidic devices with the physical manipulation could be much flexible and compatible to the bacterial samples with lower concentration, meanwhile minimizing contamination issues. Our functionalized nano-sieve system is cooperating with a 3-D beads-stacking, which can provide the accurate manipulation of capture efficiency by applied flow rates [104] and the optimized pneumatic chamber to counterbalance the

hydrodynamic pressure under the microfluidic flows [243]. In addition, this flexible pneumatic layer can significantly immobilize the bead-stacked microstructure with the positive pressure applied during the purification process, and execute an easier target release by setting the negative pressure during the retrieval process. In the future, the development of 3-D spaced beads array and the retrieval procedure could be more beneficial to a higher capture efficiency and concentration factor of target bacteria, respectively, aiming to improve the detection limit by combining with our optimized molecular detection technique.

While our current research introduced the MRSA-spiked blood samples, the future work could be engaged in investigating clinical samples to validate the availability of our approach in the field of biomedical research and clinical diagnostics of bacteremia, such as sepsis. So far, our system had been simultaneously tested up to six samples. However, introducing more channels in a 6-inch glass wafer during the device fabrication process, we can achieve the simultaneous detection of hundreds of clinical samples using a sample equipment setup comprising a multi-channel pump, pipetting system, heat block, magnet, transilluminator, and other necessary components. Therefore, this microfluidic device could enable a multiplexing purification and retrieval for various pathogens from different samples [229], [244]. Additionally, while our RPA/CRISPR-Cas assay is currently performed in tubes after bacterial concentration by nano-sieve and is still requiring manual pipetting, our future work would integrate a well-developed microfluidic platform with this molecular detection technique for operating an on-chip real-time detection of target pathogens, potentially reducing the processing time for the positive results. At this point,

we could also develop the operation process by introducing the one-pot reaction based on RPA and CRISPR assay [245], [246].

6.5 Conclusion

In summary, we have proposed a miniaturized and multi-functional nano-sieve platform integrated with a pneumatical chamber for a rapid purification and high concentration of MRSA bacteria from RBCs-free samples. Our developed fabrication process is simplified, time-saving, and cost-efficient, but generating multiple channels in one 6-inch wafer. This approach leads to an efficient capture of MRSA via the precise control of the applied flow rate, resulting in a significant concentration of captured bacteria (~15-fold). The developed nano-sieve integrated with RPA/CRISPR-Cas12 assay significantly improves the detection sensitivity, resulting in a lower on-chip detection limit of 100 CFU/mL compared to the off-chip limit of 10^4 CFU/mL. Importantly, this sensitive detection method was completed in less than 4 hours under body temperature (~37 °C) conditions, without using the centrifugation. The scalability of the nano-sieve device allows for the simultaneous processing of multiple clinical samples and multiplexing detection of different pathogens. By developing MRSA detection technique for the enhancement of its sensitivity and specificity, our approach shows potential in improving patient outcomes and addressing the challenges posed by ARB infections.

Chapter 7. Conclusion and Future Opportunities

*Part of the content in this chapter reprinted with the permission of “Korensky, G., **Chen, X.**, Bao, M., Miller, A., Lapizco-Encinas, B., Park, M. and Du, K., 2021. Single *Chlamydomonas reinhardtii* cell separation from bacterial cells and auto-fluorescence tracking with a nanosieve device. **Electrophoresis**, 42(1-2), pp.95-102” and “Nanaware, A., Kranbuhl, T., Ching, J., Chen, J.S., **Chen, X.**, Tu, Q. and Du, K., 2022. Pneumatic controlled nanosieve for efficient capture and release of nanoparticles. **Journal of Vacuum Science & Technology B**, 40(6).”*

Sepsis, a condition characterized by life-threatening dysfunction of organs, typically arises from a response of the body to bacterial infection [247]. In order to mitigate the mortality rates associated with sepsis and alleviate the burden on healthcare systems, it is crucial to achieve early detection of sepsis. Delays in administering appropriate antibiotics by even an hour could lead to a 7.6% increase in mortality for patients suffering from severe sepsis and septic shock [10], [248]. To accomplish this, there is a pressing need for rapid (within a few hours), highly sensitive, specific (down to ~1 CFU/mL for each specific bacterial strain), and multiplexed methods of detecting sepsis-causing bacteria in blood samples obtained from patients [249]. In this dissertation, it has demonstrated that a novel microfluidic platform functionalized by a 3-D beads-stacked microstructure and a pneumatically controllable chamber was successfully generated to rapidly and efficiently purify the target bacteria, such as MRSA, from laboratory-based blood sample. By incorporating with a molecular detection technique, i.e., PRA/CRISPR-Cas system, the low-concentration targets from blood sample can be fully isolated, highly concentrated, and specifically identified, potentially for detecting sepsis-causing bacteria in patients' blood samples in near future. This chapter summarizes the present research on an efficient purification and detection of ARB from whole blood by combining an optimized nanosieve device with a developed RPA/CRISPR-Cas assay. This chapter also highlights the key contributions and future opportunities.

7.1 Research summary

By combining microfluidics with advanced molecular detection techniques, this study seeks to enable the development of novel diagnostic tools that can address the urgent need for rapid and accurate identification of antibiotic-resistant bacterial strains. The field of microfluidics empowers the manipulation of fluids, with either small or large volumes, granting precise command over fluid flow and analysis. Leveraging the inherent benefits of microfluidics, such as high throughput and compatibility with automation, renders it an optimal platform for tackling the obstacles involved in simultaneous purification and detection of multiple bacterial targets. On the other hand, molecular diagnostic technology has gained extensive utilization in bacteria identification due to its multitude of advantages over traditional methods, including exceptional accuracy and specificity in targeting specific and unique DNA sequences associated with the bacteria of interest. Additionally, molecular methods offer the advantage of optimized processing times, often within a few hours, as compared to culture-based methods. Therefore, the integration of microfluidic platform and molecular detection technique could be a promising method for the aim of early detection of sepsis, so that potentially improving the survival of those infectious patients.

In Chapter 1 of this dissertation, the current condition of bloodstream infections (BSI) and the current technologies for diagnosing BSI, such as sepsis, has been reviewed, leading to the motivation and the objectives to design, fabricate, and develop a robust microfluidic platform, i.e., nano-sieve, for rapidly and efficiently purifying the target bacteria from the desired samples, by combining with a reliable molecular detection technique, i.e.,

RPA/CRISRP-Cas assay, for specifically and sensitively identifying the target bacteria within a short time.

The details of Chapter 2 mainly focus on the validation of theoretical model related to a super shallow nano-sieve channel based on an idea of deformable microfluidics. An experimental measurement of the trapping efficiency of fluorescent microparticles was subsequently conducted using the manufactured nano-sieve, which served to verify the accuracy of the model. Building upon this, the established model was employed to gain insights into channel deformation at varying flow rates, thereby enabling further optimization of nano-sieve microfluidics. The calculated capture efficiency closely matched the experimental data, demonstrating the reliability of the model. Consequently, this robust model can effectively predict changes in trapping efficiency across different flow rates and channel heights. Furthermore, general guidelines were developed for the advancement of deformable microfluidics in isolating and releasing micro- and nano-particles with diverse channel heights and flow rates.

The following Chapter 3 further demonstrates the development of fabricating an extremely thin nano-sieve channel with an aspect ratio of 1:10,000, down to ~200 nm in depth. The exceptional characteristics of this nano-sieve device offer the opportunity to better concentrate, release, and harvest molecular targets from original samples, facilitating downstream analysis. Moreover, this advancement directly tackles the prevalent problem of clogging encountered in filtration applications. Therefore, the innovative nano-sieve device was developed to efficiently and easily separate microalgae and bacteria at the single-cell level by leveraging hydrodynamically controlled deformation. In addition, by

incorporating a sacrificial layer, the device effectively prevents channel collapse and leakage, while minimizing flow resistance during the separation process.

A significant improvement in a 3-D beads-stacked microstructure within the well-established nano-sieve channel was exhibited in Chapter 4. In our pursuit of developing a fast and reliable method for the separation and detection of ARB, this research has successfully created a miniaturized system. This innovative system enables the physical separation and concentration of bacteria from buffer solutions and blood plasma. This breakthrough was achieved through the 3-D stacking of nonfunctional magnetic microbeads within a confined nano-sieve device that features numerous voids at the interface, which were also thoroughly investigated using optical coherence tomography (OCT), computational fluid dynamics (CFD) simulation, and machine learning reconstruction. Our findings demonstrate that this system exhibits an exceptionally high efficiency in capturing bacteria, and it can aggregate bacteria on-chip when dealing with samples of lower concentrations. Importantly, the bacteria can be easily retrieved and concentrated in a designated buffer without altering their properties.

Chapter 5 presents a significant progress in developing the deformable microfluidic system that utilizes a nano-sieve channel packed with magnetic microbeads. The efficacy of this system has been confirmed through various validation methods, including fluorescence microscopy, OCT scanning, mechanical testing, and a computational fluidic model. Our developed theoretical model also accurately predicts the leakage of microbeads under specific conditions, providing valuable insights for designing next-generation separation systems. Notably, our plasma separation process based on the improved beads stacking only requires minimal blood dilution and can rapidly process blood samples.

Furthermore, by leveraging the deformable nature of the device, we have successfully demonstrated efficient retrieval of RBCs after plasma separation, while a small volume of blood sample has been tested in this study.

To further develop a rapid and reliable system to purify and detect the targets, the idea of integrating the microfluidic platform with a molecular detection technique was proposed in Chapter 6. We have introduced a miniaturized and versatile nano-sieve platform that incorporates a pneumatical chamber, enabling rapid purification by well-secured beads array and high concentration of MRSA bacteria from RBCs-free samples. Our fabrication process is streamlined, time-efficient, and cost-effective, allowing for the creation of multiple channels on a single 6-inch wafer. By precisely controlling the applied flow rate, our approach ensures effective capture of MRSA bacteria, leading to a substantial concentration of the captured bacteria. Furthermore, the integration of the developed nano-sieve with the RPA/CRISPR-Cas assay represents a substantial advancement in detection sensitivity. The positive results can be easily realized by naked eye, leading to a rapid and direct detection method for target bacteria.

In summary, a microfluidic-based deformable nano-sieve device was designed and fabricated, then further developed and optimized for the bacterial purification process from desired sample solutions. The performance of 3-D beads stacking was also investigated via optical coherence tomography (OCT), computational fluid dynamics (CFD), and machine learning reconstruction. Improvement of this nano-sieve system was achieved by introducing a pneumatic chamber to make 3-D beads-stacked microstructure more reliable without leaking issue, further optimizing the capture efficiency and retrieval process. The

developed molecular detection technique was also explored in detail, to highlight a reliable and promising approach for rapid and efficient bacterial purification and identification.

7.2 Key contributions

This dissertation is aimed at the generation and development of a microfluidic-based deformable nano-sieve device for highly efficient purification of target bacteria from whole blood, and at the integration of a molecular detection technique to achieve a fast but reliable on-chip identification of those purified bacteria that are concentrated by nano-sieve.

In Chapter 2 and Chapter 3, a simple but functional nano-sieve device was successfully created through a cost-effective and easily-operated fabrication process. The fluorescent microparticles were applied to evaluate the performance of trapping efficiency of such a nano-sieve device. Almost all the microparticles (~99% from quantitative data) were captured by the hydrodynamically deformed nano-sieve channel (1 μm in thickness) under a high flow rate of 20 $\mu\text{L}/\text{min}$. It was also found that increased flow rate can raise the roof of compliant channel induced by a hydrodynamic deformation, so that easily releasing the trapped microparticles for downstream analysis. Moreover, a theoretical model was established to reveal the capture efficiency as a function of the dimensions of channel and the size of applied microparticles. This investigation could support and nationalize the experimental findings, so that predicting the capture efficiency of microparticles with a nano-sieve device, under the condition of various dimensions and flow rates. Additionally, an optimized fabrication process can be employed to generate a thinner nano-sieve channel with an aspect ratio of 1:10,000 via the application of the sacrificial material within the channel. This approach significantly prevents the technical issues of PDMS roof collapse

during the fabrication of nanofluidic channel. By using the rigid microparticles and soft cells, the capability of such a nano-sieve device has been evaluated for the separation and concentration, and release of various targets. Therefore, this breakthrough not only enables efficient separation but also addresses critical issues associated with filtration, making it a valuable tool in various applications. Moreover, this study could facilitate the optimization of next-generation deformable microfluidic platform for the efficient manipulation of building micro- and nanostructure [250], [251].

The following contribution afterward, described in Chapter 4, was to create a 3-D magnetic beads-stacked microstructure within this highly deformable nano-sieve channel, thus forming the voids between the applied beads for a size-selective capture of target bacteria. In this case, *E. coli*-spiked in PBS buffer solution and in blood plasma had been tested via such a developed filtering system with a combination of beads in various sizes, leading to an impressive capture efficiency of ~92%, compared to the capture efficiency of only ~18% while applying the filtering system without any beads array. Moreover, leveraging the high deformability of nano-sieve, an *E. coli* sample can be fully retrieved by applying a higher flow rate, collected in a fresh PBS-based buffer with a smaller volume. With this feature, an on-chip concentration factor of ~11-fold has been achieved by adjusting the volume of initial sample solution and retrieved solution. Significantly, this device possesses key attributes such as multiplexed capability, miniaturization, affordability, and transparency, rendering it simple to fabricate, operate, and detect. As a result, it proves to be an ideal solution for pathogen separation and concentration in both laboratory and point-of-care (POC) settings.

In Chapter 5, we also explored the capability of such a nano-sieve device to separate the plasma from whole blood and retrieve blood cells, as efficiently separating blood cells and plasma plays a crucial role in various molecular diagnosis and therapeutic applications. In this study, the microscope imaging, OCT scanning, and mechanical tests were used to investigate and understand the mechanical properties of the nano-sieve channel, flow rate, and microbeads packing/leaking, leading to support and rationalize the experimental validation. The development of this deformable nano-sieve device holds promise as a new solution for centrifuge-free diagnosis and treatment of bloodborne diseases. Additionally, it contributes to the advancement of next-generation deformable microfluidics for separation applications.

Last, the research discussed in Chapter 6 creates a reliable approach to rapidly and efficiently purify and identify the target bacteria from blood sample, by integrating a molecular detection technique to a pneumatically-regulated multiplexing nano-sieve device. The improvement of nano-sieve device indicates a more reliable filtering system, in which the 3-D beads stacking has much higher reliability to avoid the beads leaking issue and a simpler and easier retrieval of captured bacteria can be achieved by accurately tuning the pressure within the pneumatic chamber. By introducing the multi-channels for a multiplexing purification procedure, a rapid and effective bacterial separation from whole blood was also completed, and a ~15-fold concentration factor can be reached. Our developed nano-sieve, combined with the RPA/CRISPR-Cas12 assay, achieves a substantial enhancement in detection sensitivity. It enables a significantly lower on-chip detection limit of 100 CFU/mL, surpassing the off-chip limit of 10^4 CFU/mL. Notably, this highly sensitive detection method is accomplished in less than 4 hours under the body

temperature conditions (~37 °C), and not requiring the need of centrifugation. This breakthrough offers a rapid and efficient solution for the detection of target analytes, thereby holding immense potential for various diagnostic and research applications.

7.3 Future opportunities

The current research in this dissertation states a promising approach for a rapid and reliable purification and detection of ARB from whole blood, by combining a molecular detection technique with a pneumatically-regulated nano-sieve platform. The following directions could be followed up.

7.3.1 Develop a pneumatically-regulated nano-sieve for targeting biomolecules

The efficient isolation and retrieval of biomolecules are crucial for a wide range of biomedical applications, including molecular diagnostics [244], precision therapeutics [252], and mechanobiology [253]. Nanofiltration membranes with controllable selectivity have emerged as a promising approach due to the lower cost and ease of use. However, these membranes often require additional post-treatments to remove or retrieve the captured targets, which can be complicated and may alter the membrane properties [254]. Electrophoresis has also been developed for the separation of nanoparticles, nucleic acids, proteins, and cells. However, it relies on high DC voltage and is not directly applicable in complex biofluids, as it can disrupt the electrostatic forces in the solution. To overcome these challenges, micro- and nanofluidic systems have been developed in recent years, by offering high scalability and resolution. These systems provide an alternative approach for efficient isolation and retrieval of biomolecules without the requirements of extensive post-treatments or high voltage.

A simple confinement utilizing a convex lens and a flat substrate has been introduced to enhance the trapping efficiency of molecules for fluorescence sensing [255]. However, this approach only allows to form a single trapped region. On the other hand, top-down approaches have been utilized to create nanofluidic channels with intricate nanofeatures, such as dual height and staircase nanochannels, offering controllable geometries [256], [257]. Nevertheless, the fabrication and bonding processes for these chips pose challenges. More recently, Wunsch *et al.* developed a laterally nano-scaled displacement chip with periodic nanopillars, enabling the separation of exosomes from colloids, even as small as 20 nm in size [84]. This chip has also been used to manipulate and stretch lambda DNA within the 2D nanopatterns [258]. Additionally, Yu *et al.* demonstrated single-cell capture and single-DNA linearization using a pneumatic microchannel and nanoslit, laying the foundation for a fully integrated on-chip device for nucleic acid extraction and genome sequencing [96].

Recently, a nano-sieve platform was designed to effectively capture and retrieve microparticles by simply tuning the hydrodynamic pressure within the deformable nano-scaled channel [79]. By securing different sizes of magnetic microparticles, such a device has been developed to separate, concentrate, and retrieve micro-organisms and red blood cells from bodily fluids at a high flow rate, further leading to an on-chip sepsis diagnosis [199], [98]. However, the capacity of this nano-sieve could be improved by modifying the structure of channel itself, so that enabling the potential capture for the small nanoparticles.

As described in Chapter 6, a pneumatically-regulated nano-sieve has been successfully fabricated for better locking the 3-D beads-stacked microstructure, aiming

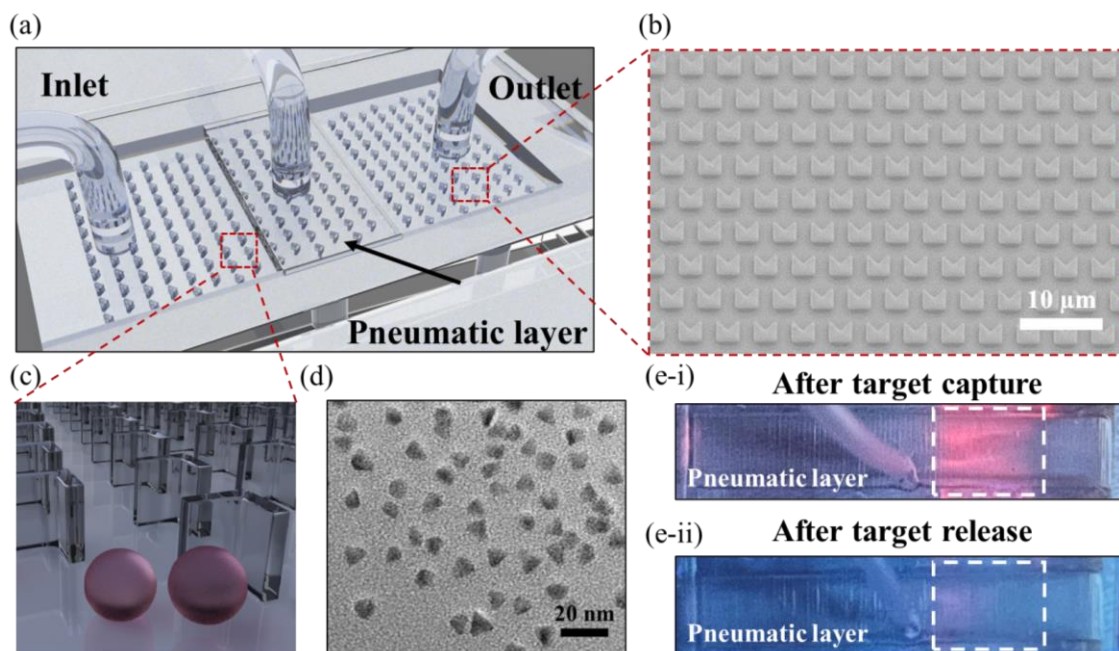


Figure 7.1 (a) Schematic of the pneumatic controlled nano-sieve device. (b) SEM image of the microgrooves inside the channel with a feature size of $5\ \mu\text{m}$. (c) Schematic of the microgrooves patterned on the glass substrate with the introduced nanoparticles. (d) TEM image of the applied quantum dots. (e) Photograph of the channel: after target capture (e-i) and after target release (e-ii). Reprinted from [243].

to capture the small-sized bacteria, such as MRSA, from whole blood. The addition of this pneumatic chamber can be easily precisely controlled by tuning the applied pressure, achieving the counterbalance of hydrodynamic pressure within the channel induced by high flow rate. On the other hand, guided by CFD, microgrooves with a feature size of $\sim 5\ \mu\text{m}$ were patterned on the bottom of nano-sieve channel, as shown in **Figure 7.1(a) and 7.1(b)**, exploring the performance of this new nano-sieve channel for highly efficient capture of nanoparticles, i.e., quantum dots with a diameter of $15\ \text{nm}$ (**Figure 7.1(d)**). By incorporating our numerical simulations and experimental findings, we have demonstrated that the presence of microgrooves reduces the flow rate in their vicinity, thereby enhancing the trapping efficiency of quantum dots.

Importantly, the captured targets can be easily retrieved for downstream analysis by simply deactivating the positive pneumatic pressure (**Figure 7.1(e)**).

Therefore, the future opportunity based on the employment of improved nano-sieve with patterned microgrooves could be extended to 1) the channel design with adaptable height and width, and microstructure shape; 2) the theoretical perspective and experimental observation for the mechanical properties, regarding the deformable PDMS roof and the pneumatic pressure by even higher flow rate, further optimizing the target capture and release; 3) established protocols of lysis and purification, which could be integrated into this kind of nano-sieve for the extraction of biomolecules.

7.3.2 Study microalgae cells with a nano-sieve device for next-generation biosensor

In recent years, there has been significant interest in microalgae due to their potential applications in food, feed additives, environmental monitoring, renewable energy, and cosmetics [106], [260]. Microalgal biofuel, for instance, offers a unique solution to develop the renewable energy, because of the numerous advantages of microalgae, such as high growth rate, co-products similar to conventional fuels followed by oil extraction, ability to remediate wastewater, independence from arable land, and capabilities of carbon dioxide fixation [261], [262].

To explore microalgae as a potential next-generation biofuel, it is crucial to maintain the viability of microalgae population over extended periods of time [106]. Biological contaminants, including bacteria populations, can have adverse effects on microalgae populations. Some microbes, for instance, can damage the microalgae cell wall and inhibit their growth [108], [109]. The deformable nano-sieve device can

efficiently isolate microalgae from bacteria, enabling the manipulation of microalgae while mitigating the presence of contaminants. Even though other microfluidic methods have been introduced for microalgae and bacteria separation, they typically require complicated microchannel design and characterizations of the fluid elasticity [110], [111]. Methods for the physical separation of much larger cells have taken advantage of the size difference of cells quite effectively, but not at the scale presented in this study [112], [113]. Those devices also have more complicated geometries involving more lengthy fabrication processes, compared to the fabrication of nano-sieve, described in those works. With the nano-sieve, the separation is achieved by fine-tuning the flow rate and hydrodynamic deformation. As shown in **Figure 3.11**, the majority of contaminant bacteria cells were efficiently washed into the waste reservoir without the loss of microalgae. However, micrographs taken before and after the mixed *C. reinhardtii* and *E. coli* solutions indicate that the amount of *C. reinhardtii* cells trapped in the channel was lower than solutions containing only *C. reinhardtii*, even though a significant amount of *C. reinhardtii* cells were still visible in the channel. This indicates that a portion of the *C. reinhardtii* cells could be lysed when pumped through the channel with *E. coli* cells. This could have been caused by differences in size, shape, and velocity between *E. coli* cells and *C. reinhardtii* cells flowing through the channels. This may have resulted in the *C. reinhardtii* cells being speared by the *E. Coli* cells since *E. Coli* cells are rod-like while *C. reinhardtii* cells are spherical. Alternatively, *C. reinhardtii* and *E. Coli* solution could have been more densely packed due to the additional *E. Coli* causing the *C. reinhardtii* to have less room for deformation.

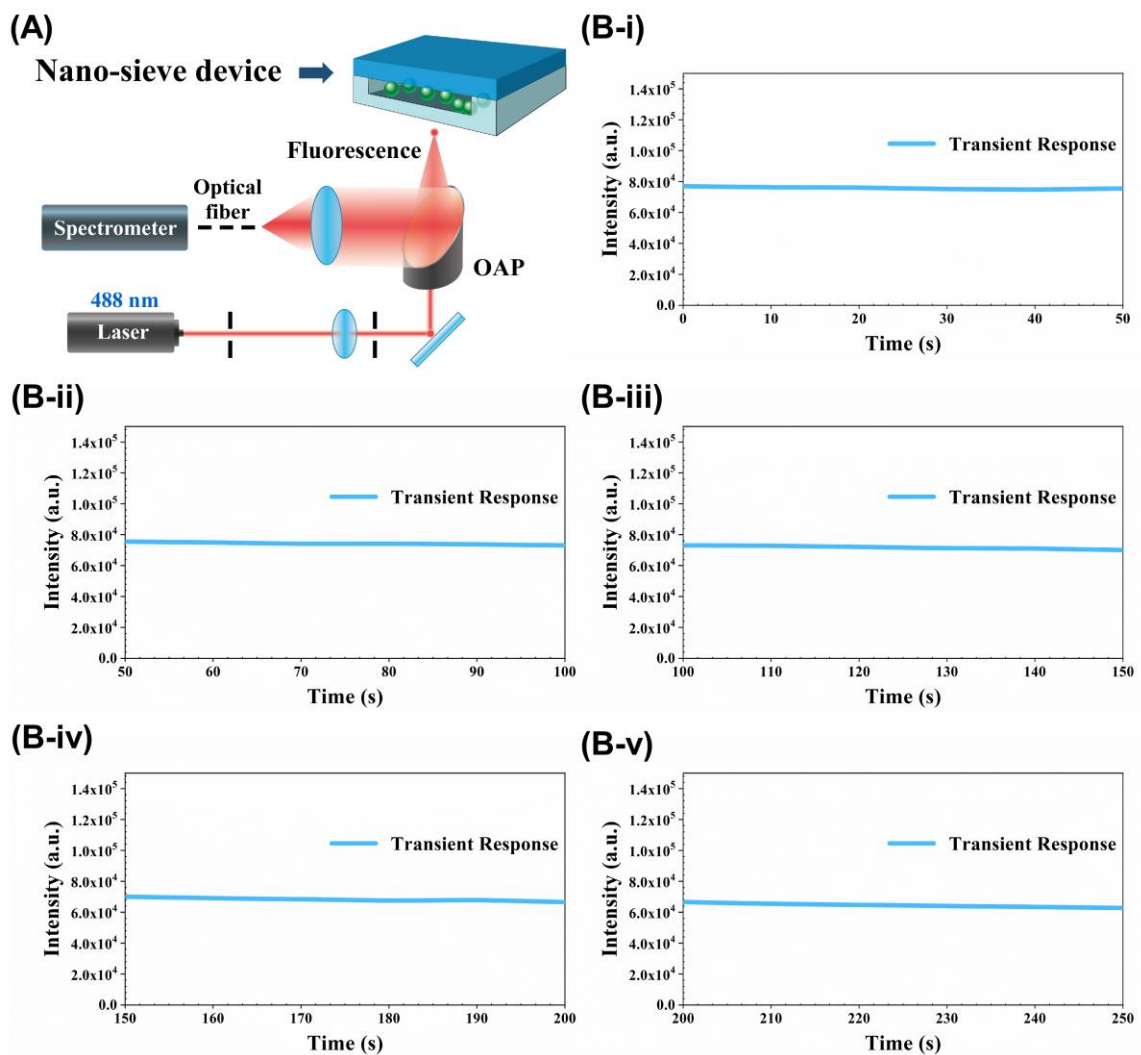


Figure 7.2 (A) The integrated fluorometer used to measure the auto-fluorescence signal from the trapped *C. reinhardtii* cells. (B) The auto-fluorescence intensity of *C. reinhardtii* cells under continuous excitation: (B-i) 0-50 s; (B-ii) 50-100 s; (B-iii) 100-150 s; (B-iv) 150-200 s; (B-v) 200-250 s. The background signal without *C. reinhardtii* cells is $\sim 1.9 \times 10^3$ a.u., which is over a full order of magnitude lower than the signal observed with *C. reinhardtii* cells. Reprinted from [99].

Understanding this phenomenon is not the intention of this work but it is an interesting observation.

In this study, we have taken the initial step towards establishing a reliable, inexpensive, and label-free separation and biosensing. Furthermore, stable sensing can

be implemented since, as shown in **Figure 7.2**, *C. reinhardtii* cells exhibited the ability for continuous laser excitation for minutes with minimal photobleaching issues. Many existing microalgae biosensors are facing challenges related to the stability of the fluorescence signal over time, and various immobilization techniques are being explored to address this limitation [106]. Large fluctuations in the auto-fluorescent signal of the *C. reinhardtii* cells could result in false-positive and false-negative results. Combining the small and sensitive fluorometer with *C. reinhardtii* cells trapped nano-sieve device, excellent auto-fluorescence stability of *C. reinhardtii* cells over a long period was demonstrated, which can be further used for rapid and label-free detection of aquatic pollutants [263]. This auto-fluorescence stability indicates the continued viability of the trapped cells. This proposed method can be employed for single-cell analysis in genomics, transcriptomics, and metabolomics without the need for complex serial dilution, micromanipulation, or dielectrophoretic sorting techniques.

Due to its minimal photo-bleaching issues, the proposed method shows promise as a label-free biosensor for environmental monitoring. Future research aims to enhance this method for generating a multiplexing and high-throughput bio- and chemical sensor [264].

Chapter 8. Bibliography

- [1] K. B. Laupland, H. Lee, D. B. Gregson, and B. J. Manns, “Cost of intensive care unit-acquired bloodstream infections,” *J. Hosp. Infect.*, vol. 63, no. 2, pp. 124–132, Jun. 2006, doi: 10.1016/j.jhin.2005.12.016.
- [2] S. S. Magill *et al.*, “Multistate Point-Prevalence Survey of Health Care–Associated Infections,” *N. Engl. J. Med.*, vol. 370, no. 13, pp. 1198–1208, Mar. 2014, doi: 10.1056/NEJMoa1306801.
- [3] H. Wisplinghoff, T. Bischoff, S. M. Tallent, H. Seifert, R. P. Wenzel, and M. B. Edmond, “Nosocomial Bloodstream Infections in US Hospitals: Analysis of 24,179 Cases from a Prospective Nationwide Surveillance Study,” p. 9.
- [4] K. B. Laupland, D. A. Zygun, H. D. Davies, D. L. Church, T. J. Louie, and C. J. Doig, “Population-based assessment of intensive care unit-acquired bloodstream infections in adults: Incidence, risk factors, and associated mortality rate,” *Crit. Care Med.*, vol. 30, no. 11, pp. 2462–2467, Nov. 2002.
- [5] M. Garrouste-Orgeas *et al.*, “Excess Risk of Death from Intensive Care Unit–Acquired Nosocomial Bloodstream Infections: A Reappraisal,” *Clin. Infect. Dis.*, vol. 42, no. 8, pp. 1118–1126, Apr. 2006, doi: 10.1086/500318.
- [6] J. R. Prowle *et al.*, “Acquired bloodstream infection in the intensive care unit: incidence and attributable mortality,” *Crit. Care*, vol. 15, no. 2, p. R100, 2011, doi: 10.1186/cc10114.
- [7] K. E. Rudd *et al.*, “Global, regional, and national sepsis incidence and mortality, 1990–2017: analysis for the Global Burden of Disease Study,” *The Lancet*, vol. 395, no. 10219, pp. 200–211, Jan. 2020, doi: 10.1016/S0140-6736(19)32989-7.
- [8] K. H. Goh *et al.*, “Artificial intelligence in sepsis early prediction and diagnosis using unstructured data in healthcare,” *Nat. Commun.*, vol. 12, no. 1, Art. no. 1, Jan. 2021, doi: 10.1038/s41467-021-20910-4.
- [9] M. J. Hall, S. N. Williams, C. J. DeFrances, and A. Golosinskiy, “Inpatient care for septicemia or sepsis: a challenge for patients and hospitals,” *NCHS Data Brief*, no. 62, pp. 1–8, Jun. 2011.
- [10] R. Frost, H. Newsham, S. Parmar, and A. Gonzalez-Ruiz, “Impact of delayed antimicrobial therapy in septic ITU patients,” *Crit. Care*, vol. 14, no. 2, p. P20, Sep. 2010, doi: 10.1186/cc9123.
- [11] L. J. Shallcross and D. S. C. Davies, “Antibiotic overuse: a key driver of antimicrobial resistance,” *Br. J. Gen. Pract.*, vol. 64, no. 629, pp. 604–605, Dec. 2014, doi: 10.3399/bjgp14X682561.
- [12] “Lack of antibiotics: are new antibiotics being developed? | BioMérieux,” *ANTIMICROBIAL RESISTANCE*. <https://amr.biomerieux.com/en/challenges/a-lack-of-antibiotics/> (accessed Mar. 30, 2021).
- [13] “WHO | Global priority list of antibiotic-resistant bacteria to guide research, discovery, and development of new antibiotics.” <https://www.who.int/medicines/publications/global-priority-list-antibiotic-resistant-bacteria/en/> (accessed Mar. 30, 2021).
- [14] A. Burklund and J. X. J. Zhang, “Microfluidics-based organism isolation from whole blood - an emerging tool for bloodstream infection diagnosis,” *Ann. Biomed. Eng.*, vol. 47, no. 7, pp. 1657–1674, Jul. 2019, doi: 10.1007/s10439-019-02256-7.
- [15] D. A. Goff, R. Kullar, K. A. Bauer, and T. M. File, “Eight Habits of Highly Effective Antimicrobial Stewardship Programs to Meet the Joint Commission Standards for Hospitals,” *Clin. Infect. Dis.*, vol. 64, no. 8, pp. 1134–1139, Apr. 2017, doi: 10.1093/cid/cix065.
- [16] J. Li, “Reviving Polymyxins: Achievements, Lessons and the Road Ahead,” in *Polymyxin Antibiotics: From Laboratory Bench to Bedside*, J. Li, R. L. Nation, and K. S. Kaye, Eds.,

- in *Advances in Experimental Medicine and Biology*. Cham: Springer International Publishing, 2019, pp. 1–8. doi: 10.1007/978-3-030-16373-0_1.
- [17] M. E. A. de Kraker, A. J. Stewardson, and S. Harbarth, “Will 10 Million People Die a Year due to Antimicrobial Resistance by 2050?,” *PLOS Med.*, vol. 13, no. 11, p. e1002184, Nov. 2016, doi: 10.1371/journal.pmed.1002184.
- [18] J. J. Kerremans *et al.*, “Rapid identification and antimicrobial susceptibility testing reduce antibiotic use and accelerate pathogen-directed antibiotic use,” *J. Antimicrob. Chemother.*, vol. 61, no. 2, pp. 428–435, Feb. 2008, doi: 10.1093/jac/dkm497.
- [19] A. van Belkum *et al.*, “Rapid Clinical Bacteriology and Its Future Impact,” *Ann. Lab. Med.*, vol. 33, no. 1, pp. 14–27, Jan. 2013, doi: 10.3343/alm.2013.33.1.14.
- [20] P. Yagupsky and F. S. Nolte, “Quantitative aspects of septicemia,” *Clin. Microbiol. Rev.*, vol. 3, no. 3, pp. 269–279, Jul. 1990, doi: 10.1128/cmr.3.3.269.
- [21] D. J. Hardy, B. B. Hulbert, and P. C. Migneault, “Time to detection of positive BacT/Alert blood cultures and lack of need for routine subculture of 5- to 7-day negative cultures,” *J. Clin. Microbiol.*, vol. 30, no. 10, pp. 2743–2745, Oct. 1992, doi: 10.1128/jcm.30.10.2743-2745.1992.
- [22] G. Peralta *et al.*, “Time-to-positivity in patients with *Escherichia coli* bacteraemia,” *Clin. Microbiol. Infect.*, vol. 13, no. 11, pp. 1077–1082, Nov. 2007, doi: 10.1111/j.1469-0691.2007.01817.x.
- [23] A. Lever and I. Mackenzie, “Sepsis: definition, epidemiology, and diagnosis,” *BMJ*, vol. 335, no. 7625, pp. 879–883, Oct. 2007, doi: 10.1136/bmj.39346.495880.AE.
- [24] C. S. Scheer *et al.*, “Impact of antibiotic administration on blood culture positivity at the beginning of sepsis: a prospective clinical cohort study,” *Clin. Microbiol. Infect.*, vol. 25, no. 3, pp. 326–331, Mar. 2019, doi: 10.1016/j.cmi.2018.05.016.
- [25] J. A. Capdevila *et al.*, “Value of differential quantitative blood cultures in the diagnosis of catheter-related sepsis,” *Eur. J. Clin. Microbiol. Infect. Dis.*, vol. 11, no. 5, pp. 403–407, May 1992, doi: 10.1007/BF01961854.
- [26] H. Salimnia *et al.*, “Evaluation of the FilmArray Blood Culture Identification Panel: Results of a Multicenter Controlled Trial,” *J. Clin. Microbiol.*, vol. 54, no. 3, pp. 687–698, Feb. 2016, doi: 10.1128/jcm.01679-15.
- [27] M. Marschal, J. Bachmaier, I. Autenrieth, P. Oberhettinger, M. Willmann, and S. Peter, “Evaluation of the Accelerate Pheno System for Fast Identification and Antimicrobial Susceptibility Testing from Positive Blood Cultures in Bloodstream Infections Caused by Gram-Negative Pathogens,” *J. Clin. Microbiol.*, vol. 55, no. 7, pp. 2116–2126, Jun. 2017, doi: 10.1128/jcm.00181-17.
- [28] H. Jg *et al.*, “Hematological and iron-related analytes--reference data for persons aged 1 year and over: United States, 1988-94.,” *Vital Health Stat. 11.*, no. 247, pp. 1–156, Mar. 2005.
- [29] Y. Xue, H. Shi, B. Feng, L. Qiao, C. Ding, and S. Yu, “Rapid identification of bacteria directly from blood cultures by Co-magnetic bead enrichment and MALDI-TOF MS profiling,” *Talanta*, vol. 233, p. 122472, Oct. 2021, doi: 10.1016/j.talanta.2021.122472.
- [30] G. A. Denomme, “The structure and function of the molecules that carry human red blood cell and platelet antigens,” *Transfus. Med. Rev.*, vol. 18, no. 3, pp. 203–231, Jul. 2004, doi: 10.1016/j.tmr.2004.03.006.
- [31] Z. Wu, B. Willing, J. Bjerketorp, J. K. Jansson, and K. Hjort, “Soft inertial microfluidics for high throughput separation of bacteria from human blood cells,” *Lab. Chip*, vol. 9, no. 9, pp. 1193–1199, 2009, doi: 10.1039/B817611F.
- [32] X. Lu and X. Xuan, “Inertia-enhanced pinched flow fractionation,” *Anal. Chem.*, vol. 87, no. 8, pp. 4560–4565, 2015.

- [33] X. Lu and X. Xuan, “Continuous Microfluidic Particle Separation via Elasto-Inertial Pinched Flow Fractionation,” *Anal. Chem.*, vol. 87, no. 12, pp. 6389–6396, Jun. 2015, doi: 10.1021/acs.analchem.5b01432.
- [34] M. Mizuno, M. Yamada, R. Mitamura, K. Ike, K. Toyama, and M. Seki, “Magnetophoresis-Integrated Hydrodynamic Filtration System for Size- and Surface Marker-Based Two-Dimensional Cell Sorting,” *Anal. Chem.*, vol. 85, no. 16, pp. 7666–7673, Aug. 2013, doi: 10.1021/ac303336f.
- [35] H.-K. Seo, Y.-H. Kim, H.-O. Kim, and Y.-J. Kim, “Hybrid cell sorters for on-chip cell separation by hydrodynamics and magnetophoresis,” *J. Micromechanics Microengineering*, vol. 20, no. 9, p. 095019, Aug. 2010, doi: 10.1088/0960-1317/20/9/095019.
- [36] S. Podszun *et al.*, “Enrichment of viable bacteria in a micro-volume by free-flow electrophoresis,” *Lab. Chip*, vol. 12, no. 3, pp. 451–457, Jan. 2012, doi: 10.1039/C1LC20575G.
- [37] M. Horká *et al.*, “Determination of methicillin-resistant and methicillin-susceptible *Staphylococcus aureus* bacteria in blood by capillary zone electrophoresis,” *Anal. Chim. Acta*, vol. 868, pp. 67–72, Apr. 2015, doi: 10.1016/j.aca.2015.02.001.
- [38] P. Dow, K. Kotz, S. Gruszka, J. Holder, and J. Fiering, “Acoustic separation in plastic microfluidics for rapid detection of bacteria in blood using engineered bacteriophage,” *Lab. Chip*, vol. 18, no. 6, pp. 923–932, 2018, doi: 10.1039/C7LC01180F.
- [39] P. Ohlsson, K. Petersson, P. Augustsson, and T. Laurell, “Acoustic impedance matched buffers enable separation of bacteria from blood cells at high cell concentrations,” *Sci. Rep.*, vol. 8, no. 1, p. 9156, Dec. 2018, doi: 10.1038/s41598-018-25551-0.
- [40] A. J. Mach and D. D. Carlo, “Continuous scalable blood filtration device using inertial microfluidics,” *Biotechnol. Bioeng.*, vol. 107, no. 2, pp. 302–311, 2010, doi: <https://doi.org/10.1002/bit.22833>.
- [41] I.-F. Cheng, T.-Y. Chen, R.-J. Lu, and H.-W. Wu, “Rapid identification of bacteria utilizing amplified dielectrophoretic force-assisted nanoparticle-induced surface-enhanced Raman spectroscopy,” *Nanoscale Res. Lett.*, vol. 9, no. 1, p. 324, Jun. 2014, doi: 10.1186/1556-276X-9-324.
- [42] R. M. Cooper *et al.*, “A microdevice for rapid optical detection of magnetically captured rare blood pathogens,” *Lab. Chip*, vol. 14, no. 1, pp. 182–188, 2014, doi: 10.1039/C3LC50935D.
- [43] D. Cai, M. Xiao, P. Xu, Y.-C. Xu, and W. Du, “An integrated microfluidic device utilizing dielectrophoresis and multiplex array PCR for point-of-care detection of pathogens,” *Lab. Chip*, vol. 14, no. 20, pp. 3917–3924, Sep. 2014, doi: 10.1039/C4LC00669K.
- [44] X. Chen, K. M. Ryan, D. Hines, L. Pan, K. Du, and S. Xu, “Three-dimensional visualization of dentine occlusion based on FIB-SEM tomography,” *Sci. Rep.*, vol. 13, no. 1, Art. no. 1, Feb. 2023, doi: 10.1038/s41598-023-29155-1.
- [45] R. Layouni *et al.*, “High contrast cleavage detection for enhancing porous silicon sensor sensitivity,” *Opt. Express*, vol. 29, no. 1, pp. 1–11, Jan. 2021, doi: 10.1364/OE.412469.
- [46] S. Kersting, V. Rausch, F. F. Bier, and M. von Nickisch-Rosenegk, “Multiplex isothermal solid-phase recombinase polymerase amplification for the specific and fast DNA-based detection of three bacterial pathogens,” *Microchim. Acta*, vol. 181, no. 13, pp. 1715–1723, Oct. 2014, doi: 10.1007/s00604-014-1198-5.
- [47] Q. He, M. Bao, K. Hass, W. Lin, P. Qin, and K. Du, “Perspective of Molecular Diagnosis in Healthcare: From Barcode to Pattern Recognition,” *Diagnostics*, vol. 9, no. 3, Art. no. 3, Sep. 2019, doi: 10.3390/diagnostics9030075.
- [48] M. Bao *et al.*, “A simple, pipette-free, and power-free device for virus nucleic acid detection,” in *Frontiers in Biological Detection: From Nanosensors to Systems XV*, SPIE, Mar. 2023, pp. 25–27. doi: 10.1117/12.2653148.

- [49] K. Hass *et al.*, “Chapter 7 - Recent advances in nucleic acid analysis and detection with microfluidic and nanofluidics,” in *Multidisciplinary Microfluidic and Nanofluidic Lab-on-a-chip*, X. (James) Li, C. Yang, and P. C. H. Li, Eds., Amsterdam: Elsevier, 2022, pp. 199–233. doi: 10.1016/B978-0-444-59432-7.00001-7.
- [50] N. T. Trung, N. S. Thau, M. H. Bang, and L. H. Song, “PCR-based Sepsis@Quick test is superior in comparison with blood culture for identification of sepsis-causative pathogens,” *Sci. Rep.*, vol. 9, no. 1, Art. no. 1, Sep. 2019, doi: 10.1038/s41598-019-50150-y.
- [51] S. Omar, S. Murphy, R. Gheevarghese, and N. Poppleton, “A retrospective evaluation of a multiplex polymerase chain reaction test directly applied to blood for the management of sepsis in the critically ill,” *South. Afr. J. Crit. Care Online*, vol. 37, no. 3, pp. 115–118, Nov. 2021, doi: 10.7196/SAJCC.2021.v37i3.495.
- [52] C. Oeser *et al.*, “PCR for the detection of pathogens in neonatal early onset sepsis,” *PLOS ONE*, vol. 15, no. 1, p. e0226817, Jan. 2020, doi: 10.1371/journal.pone.0226817.
- [53] V. E. Hillary and S. A. Ceasar, “A Review on the Mechanism and Applications of CRISPR/Cas9/Cas12/Cas13/Cas14 Proteins Utilized for Genome Engineering,” *Mol. Biotechnol.*, vol. 65, no. 3, pp. 311–325, Mar. 2023, doi: 10.1007/s12033-022-00567-0.
- [54] C. J. Smith and A. M. Osborn, “Advantages and limitations of quantitative PCR (Q-PCR)-based approaches in microbial ecology,” *FEMS Microbiol. Ecol.*, vol. 67, no. 1, pp. 6–20, Jan. 2009, doi: 10.1111/j.1574-6941.2008.00629.x.
- [55] S. Lutz *et al.*, “Microfluidic lab-on-a-foil for nucleic acid analysis based on isothermal recombinase polymerase amplification (RPA),” *Lab. Chip*, vol. 10, no. 7, pp. 887–893, 2010, doi: 10.1039/B921140C.
- [56] Z. A. Crannell, B. Rohrman, and R. Richards-Kortum, “Equipment-Free Incubation of Recombinase Polymerase Amplification Reactions Using Body Heat,” *PLOS ONE*, vol. 9, no. 11, p. e112146, Nov. 2014, doi: 10.1371/journal.pone.0112146.
- [57] O. Piepenburg, C. H. Williams, D. L. Stemple, and N. A. Armes, “DNA Detection Using Recombination Proteins,” *PLOS Biol.*, vol. 4, no. 7, p. e204, Jun. 2006, doi: 10.1371/journal.pbio.0040204.
- [58] J. Waitkus *et al.*, “Gold Nanoparticle Enabled Localized Surface Plasmon Resonance on Unique Gold Nanomushroom Structures for On-Chip CRISPR-Cas13a Sensing (Adv. Mater. Interfaces 1/2023),” *Adv. Mater. Interfaces*, vol. 10, no. 1, p. 2370004, 2023, doi: 10.1002/admi.202370004.
- [59] L. Liu *et al.*, “Gold Nanoparticle-Labeled CRISPR-Cas13a Assay for the Sensitive Solid-State Nanopore Molecular Counting,” *Adv. Mater. Technol.*, vol. 7, no. 3, p. 2101550, 2022, doi: 10.1002/admt.202101550.
- [60] K. N. Hass *et al.*, “Integrated Micropillar Polydimethylsiloxane Accurate CRISPR Detection System for Viral DNA Sensing,” *ACS Omega*, vol. 5, no. 42, pp. 27433–27441, Oct. 2020, doi: 10.1021/acsomega.0c03917.
- [61] M. Bao, E. Jensen, Y. Chang, G. Korensky, and K. Du, “Magnetic Bead-Quantum Dot (MB-Qdot) Clustered Regularly Interspaced Short Palindromic Repeat Assay for Simple Viral DNA Detection,” *ACS Appl. Mater. Interfaces*, vol. 12, no. 39, pp. 43435–43443, Sep. 2020, doi: 10.1021/acsomega.0c12482.
- [62] M. Bao *et al.*, “Challenges and Opportunities for Clustered Regularly Interspaced Short Palindromic Repeats Based Molecular Biosensing,” *ACS Sens.*, vol. 6, no. 7, pp. 2497–2522, Jul. 2021, doi: 10.1021/acssensors.1c00530.
- [63] L. Liu *et al.*, “Aerosol Jet Printing-Enabled Dual-Function Electrochemical and Colorimetric Biosensor for SARS-CoV-2 Detection,” *Anal. Chem.*, Jul. 2023, doi: 10.1021/acs.analchem.3c01724.
- [64] R. Barrangou, “The roles of CRISPR–Cas systems in adaptive immunity and beyond,” *Curr. Opin. Immunol.*, vol. 32, pp. 36–41, Feb. 2015, doi: 10.1016/j.coi.2014.12.008.

- [65] Z. Zhu *et al.*, “PAM-free loop-mediated isothermal amplification coupled with CRISPR/Cas12a cleavage (Cas-PfLAMP) for rapid detection of rice pathogens,” *Biosens. Bioelectron.*, vol. 204, p. 114076, May 2022, doi: 10.1016/j.bios.2022.114076.
- [66] T. Zhang *et al.*, “Direct Detection of Foodborne Pathogens via a Proximal DNA Probe-Based CRISPR-Cas12 Assay,” *J. Agric. Food Chem.*, vol. 69, no. 43, pp. 12828–12836, Nov. 2021, doi: 10.1021/acs.jafc.1c04663.
- [67] M. Wang, R. Zhang, and J. Li, “CRISPR/cas systems redefine nucleic acid detection: Principles and methods,” *Biosens. Bioelectron.*, vol. 165, p. 112430, Oct. 2020, doi: 10.1016/j.bios.2020.112430.
- [68] Y. Dai, Y. Wu, G. Liu, and J. J. Gooding, “CRISPR Mediated Biosensing Toward Understanding Cellular Biology and Point-of-Care Diagnosis,” *Angew. Chem. Int. Ed.*, vol. 59, no. 47, pp. 20754–20766, 2020, doi: 10.1002/anie.202005398.
- [69] J. Wei, “Accurate and sensitive analysis of *Staphylococcus aureus* through CRISPR-Cas12a based recycling signal amplification cascades for early diagnosis of skin and soft tissue infections,” *J. Microbiol. Methods*, vol. 183, p. 106167, Apr. 2021, doi: 10.1016/j.mimet.2021.106167.
- [70] H. Liu *et al.*, “RPA-Cas12a-FS: A frontline nucleic acid rapid detection system for food safety based on CRISPR-Cas12a combined with recombinase polymerase amplification,” *Food Chem.*, vol. 334, p. 127608, Jan. 2021, doi: 10.1016/j.foodchem.2020.127608.
- [71] Z. Chen *et al.*, “CRISPR/Cas12a and immuno-RCA based electrochemical biosensor for detecting pathogenic bacteria,” *J. Electroanal. Chem.*, vol. 901, p. 115755, Nov. 2021, doi: 10.1016/j.jelechem.2021.115755.
- [72] S. Bu *et al.*, “Ultrasensitive detection of pathogenic bacteria by CRISPR/Cas12a coupling with a primer exchange reaction,” *Sens. Actuators B Chem.*, vol. 347, p. 130630, Nov. 2021, doi: 10.1016/j.snb.2021.130630.
- [73] N. Sundararajan, D. Kim, and A. A. Berlin, “Microfluidic operations using deformable polymer membranes fabricated by single layer soft lithography,” *Lab. Chip*, vol. 5, no. 3, pp. 350–354, Feb. 2005, doi: 10.1039/B500792P.
- [74] D. Tachibana *et al.*, “Ultrafast and Highly Deformable Electromagnetic Hydrogel Actuators Assembled from Liquid Metal Gel Fiber,” *Adv. Intell. Syst.*, vol. 4, no. 5, p. 2100212, 2022, doi: 10.1002/aisy.202100212.
- [75] D. Velasco Anez, C. Hadji, E. Santanach-Carreras, E. Lorceau, and C. Picard, “Microfluidic channels of adjustable height using deformable elastomer,” *Microfluid. Nanofluidics*, vol. 25, no. 1, p. 7, Jan. 2021, doi: 10.1007/s10404-020-02408-5.
- [76] K. Du, I. Wathuthanthri, J. Ding, and C.-H. Choi, “Superhydrophobic waveguide: Liquid-core air-cladding waveguide platform for optofluidics,” *Appl. Phys. Lett.*, vol. 113, no. 14, p. 143701, Oct. 2018, doi: 10.1063/1.5049692.
- [77] X. Ren, B. M. Foster, P. Ghassemi, J. S. Strobl, B. A. Kerr, and M. Agah, “Entrapment of Prostate Cancer Circulating Tumor Cells with a Sequential Size-Based Microfluidic Chip,” *Anal. Chem.*, vol. 90, no. 12, pp. 7526–7534, Jun. 2018, doi: 10.1021/acs.analchem.8b01134.
- [78] M. DiSalvo *et al.*, “Characterization of Tensioned PDMS Membranes for Imaging Cytometry on Microarray Arrays,” *Anal. Chem.*, vol. 90, no. 7, pp. 4792–4800, Apr. 2018, doi: 10.1021/acs.analchem.8b00176.
- [79] X. Chen, L. Falzon, J. Zhang, X. Zhang, R.-Q. Wang, and K. Du, “Experimental and theoretical study on the microparticle trapping and release in a deformable nano-sieve channel,” *Nanotechnology*, vol. 31, no. 5, p. 05LT01, Jan. 2020, doi: 10.1088/1361-6528/ab2279.
- [80] I. C. Christov, V. Cognet, T. C. Shidhore, and H. A. Stone, “Flow rate–pressure drop relation for deformable shallow microfluidic channels,” *J. Fluid Mech.*, vol. 841, pp. 267–286, Apr. 2018, doi: 10.1017/jfm.2018.30.

- [81] R.-Q. Wang, E. E. Adams, A. W.-K. Law, and A. C. H. Lai, “Scaling Particle Cloud Dynamics: From Lab to Field,” *J. Hydraul. Eng.*, vol. 141, no. 7, p. 06015006, Jul. 2015, doi: 10.1061/(ASCE)HY.1943-7900.0000993.
- [82] R.-Q. Wang, A. W.-K. Law, and E. E. Adams, “Large-Eddy Simulation (LES) of settling particle cloud dynamics,” *Int. J. Multiph. Flow*, vol. 67, pp. 65–75, Dec. 2014, doi: 10.1016/j.ijmultiphaseflow.2014.08.004.
- [83] A. C. H. Lai, R.-Q. Wang, A. W.-K. Law, and E. E. Adams, “Modeling and experiments of polydisperse particle clouds,” *Environ. Fluid Mech.*, vol. 16, no. 4, pp. 875–898, Aug. 2016, doi: 10.1007/s10652-016-9462-3.
- [84] B. H. Wunsch *et al.*, “Nanoscale lateral displacement arrays for the separation of exosomes and colloids down to 20 nm,” *Nat. Nanotechnol.*, vol. 11, no. 11, Art. no. 11, Nov. 2016, doi: 10.1038/nnano.2016.134.
- [85] T. Salafi, K. K. Zeming, and Y. Zhang, “Advancements in microfluidics for nanoparticle separation,” *Lab. Chip*, vol. 17, no. 1, pp. 11–33, Dec. 2016, doi: 10.1039/C6LC01045H.
- [86] L. Jiang *et al.*, “Monitoring the progression of cell death and the disassembly of dying cells by flow cytometry,” *Nat. Protoc.*, vol. 11, no. 4, Art. no. 4, Apr. 2016, doi: 10.1038/nprot.2016.028.
- [87] Y. Jia, Y. Ren, and H. Jiang, “Continuous dielectrophoretic particle separation using a microfluidic device with 3D electrodes and vaulted obstacles,” *ELECTROPHORESIS*, vol. 36, no. 15, pp. 1744–1753, 2015, doi: <https://doi.org/10.1002/elps.201400565>.
- [88] S. Rampini, P. Li, and G. U. Lee, “Micromagnet arrays enable precise manipulation of individual biological analyte–superparamagnetic bead complexes for separation and sensing,” *Lab. Chip*, vol. 16, no. 19, pp. 3645–3663, Sep. 2016, doi: 10.1039/C6LC00707D.
- [89] C. M. Gabardo, A. M. Kwong, and L. Soleymani, “Rapidly prototyped multi-scale electrodes to minimize the voltage requirements for bacterial cell lysis,” *Analyst*, vol. 140, no. 5, pp. 1599–1608, Feb. 2015, doi: 10.1039/C4AN02150A.
- [90] Q. She, R. Wang, A. G. Fane, and C. Y. Tang, “Membrane fouling in osmotically driven membrane processes: A review,” *J. Membr. Sci.*, vol. 499, pp. 201–233, Feb. 2016, doi: 10.1016/j.memsci.2015.10.040.
- [91] H. S. Rho, Y. Yang, A. T. Hanke, M. Ottens, L. W. M. M. Terstappen, and H. Gardeniers, “Programmable v-type valve for cell and particle manipulation in microfluidic devices,” *Lab. Chip*, vol. 16, no. 2, pp. 305–311, Jan. 2016, doi: 10.1039/C5LC01206F.
- [92] J. Alvarado, J. Comtet, E. de Langre, and A. E. Hosoi, “Nonlinear flow response of soft hair beds,” *Nat. Phys.*, vol. 13, no. 10, Art. no. 10, Oct. 2017, doi: 10.1038/nphys4225.
- [93] J. W. Parks and H. Schmidt, “Flexible optofluidic waveguide platform with multi-dimensional reconfigurability,” *Sci. Rep.*, vol. 6, no. 1, Art. no. 1, Sep. 2016, doi: 10.1038/srep33008.
- [94] A. Mehboudi and J. Yeom, “A one-dimensional model for compressible fluid flows through deformable microchannels,” *Phys. Fluids*, vol. 30, no. 9, p. 092003, Sep. 2018, doi: 10.1063/1.5043202.
- [95] J. Lee, Y.-K. Yun, Y. Kim, and K. Jo, “PDMS nanoslits without roof collapse,” *Bull. Korean Chem. Soc.*, vol. 30, no. 8, pp. 1793–1797, 2009.
- [96] M. Yu, Y. Hou, R. Song, X. Xu, and S. Yao, “Tunable Confinement for Bridging Single-Cell Manipulation and Single-Molecule DNA Linearization,” *Small*, vol. 14, no. 17, p. 1800229, 2018, doi: <https://doi.org/10.1002/sml.201800229>.
- [97] J. D. Baker *et al.*, “Programmable, Pneumatically Actuated Microfluidic Device with an Integrated Nanochannel Array To Track Development of Individual Bacteria,” *Anal. Chem.*, vol. 88, no. 17, pp. 8476–8483, Sep. 2016, doi: 10.1021/acs.analchem.6b00889.
- [98] A. Mehboudi and J. Yeom, “A two-step sealing-and-reinforcement SU8 bonding paradigm for the fabrication of shallow microchannels,” *J. Micromechanics Microengineering*, vol. 28, no. 3, p. 035002, Mar. 2018, doi: 10.1088/1361-6439/aa9eb1.

- [99] G. Korensky *et al.*, “Single *Chlamydomonas reinhardtii* cell separation from bacterial cells and auto-fluorescence tracking with a nanosieve device,” *ELECTROPHORESIS*, vol. 42, no. 1–2, pp. 95–102, 2021, doi: 10.1002/elps.202000146.
- [100] K. Du *et al.*, “Microfluidic System for Detection of Viral RNA in Blood Using a Barcode Fluorescence Reporter and a Photocleavable Capture Probe,” *Anal. Chem.*, vol. 89, no. 22, pp. 12433–12440, Nov. 2017, doi: 10.1021/acs.analchem.7b03527.
- [101] K. L. Mills, X. Zhu, S. Takayama, and M. D. Thouless, “The mechanical properties of a surface-modified layer on polydimethylsiloxane,” *J. Mater. Res.*, vol. 23, no. 1, pp. 37–48, Jan. 2008, doi: 10.1557/JMR.2008.0029.
- [102] C. Ferrari *et al.*, “Kingdom-wide comparison reveals the evolution of diurnal gene expression in Archaeplastida,” *Nat. Commun.*, vol. 10, no. 1, Art. no. 1, Feb. 2019, doi: 10.1038/s41467-019-08703-2.
- [103] B. Liu and C. Benning, “Lipid metabolism in microalgae distinguishes itself,” *Curr. Opin. Biotechnol.*, vol. 24, no. 2, pp. 300–309, Apr. 2013, doi: 10.1016/j.copbio.2012.08.008.
- [104] X. Chen *et al.*, “Rapid *Escherichia coli* Trapping and Retrieval from Bodily Fluids via a Three-Dimensional Bead-Stacked Nanodevice,” *ACS Appl. Mater. Interfaces*, vol. 12, no. 7, Art. no. 7, Feb. 2020, doi: 10.1021/acsami.9b19311.
- [105] D. Brennan, J. Justice, B. Corbett, T. McCarthy, and P. Galvin, “Emerging optofluidic technologies for point-of-care genetic analysis systems: a review,” *Anal. Bioanal. Chem.*, vol. 395, no. 3, pp. 621–636, Oct. 2009, doi: 10.1007/s00216-009-2826-5.
- [106] R. Brayner, A. Couté, J. Livage, C. Perrette, and C. Sicard, “Micro-algal biosensors,” *Anal. Bioanal. Chem.*, vol. 401, no. 2, pp. 581–597, Aug. 2011, doi: 10.1007/s00216-011-5107-z.
- [107] L. Afi, P. Metzger, C. Largeau, J. Connan, C. Berkaloff, and B. Rousseau, “Bacterial degradation of green microalgae: incubation of *Chlorella emersonii* and *Chlorella vulgaris* with *Pseudomonas oleovorans* and *Flavobacterium aquatile*,” *Org. Geochem.*, vol. 25, no. 1, pp. 117–130, Dec. 1996, doi: 10.1016/S0146-6380(96)00113-1.
- [108] M. Arora, A. C. Anil, J. Delany, N. Rajarajan, K. Emami, and E. Mesbahi, “Carbohydrate-degrading bacteria closely associated with *Tetraselmis indica*: influence on algal growth,” *Aquat. Biol.*, vol. 15, no. 1, pp. 61–71, Apr. 2012, doi: 10.3354/ab00402.
- [109] H. Wang, R. T. Hill, T. Zheng, X. Hu, and B. Wang, “Effects of bacterial communities on biofuel-producing microalgae: stimulation, inhibition and harvesting,” *Crit. Rev. Biotechnol.*, vol. 36, no. 2, pp. 341–352, Mar. 2016, doi: 10.3109/07388551.2014.961402.
- [110] B. K. Hønsvall, D. Altin, and L. J. Robertson, “Continuous harvesting of microalgae by new microfluidic technology for particle separation,” *Bioresour. Technol.*, vol. 200, pp. 360–365, Jan. 2016, doi: 10.1016/j.biortech.2015.10.046.
- [111] A. Dewan, J. Kim, R. H. McLean, S. A. Vanapalli, and M. N. Karim, “Growth kinetics of microalgae in microfluidic static droplet arrays,” *Biotechnol. Bioeng.*, vol. 109, no. 12, pp. 2987–2996, 2012, doi: 10.1002/bit.24568.
- [112] M. C. Miller, P. S. Robinson, C. Wagner, and D. J. O’Shannessy, “The Parsortix™ Cell Separation System—A versatile liquid biopsy platform,” *Cytometry A*, vol. 93, no. 12, pp. 1234–1239, 2018, doi: 10.1002/cyto.a.23571.
- [113] X. Jin *et al.*, “An efficient method for CTCs screening with excellent operability by integrating Parsortix™-like cell separation chip and selective size amplification,” *Biomed. Microdevices*, vol. 20, no. 2, p. 51, Jun. 2018, doi: 10.1007/s10544-018-0293-5.
- [114] K. E. Heiman, R. K. Mody, S. D. Johnson, P. M. Griffin, and L. H. Gould, “*Escherichia coli* O157 Outbreaks in the United States, 2003–2012,” *Emerg. Infect. Dis.*, vol. 21, no. 8, pp. 1293–1301, Aug. 2015, doi: 10.3201/eid2108.141364.
- [115] E. Scallan *et al.*, “Foodborne Illness Acquired in the United States—Major Pathogens - Volume 17, Number 1—January 2011 - Emerging Infectious Diseases journal - CDC”, doi: 10.3201/eid1701.p11101.

- [116] R. on A. Resistance (London) and Grande-Bretagne, *Antimicrobial Resistance: Tackling a Crisis for the Health and Wealth of Nations*. Review on Antimicrobial Resistance, 2014.
- [117] L. B. Reller, M. Weinstein, J. H. Jorgensen, and M. J. Ferraro, “Antimicrobial Susceptibility Testing: A Review of General Principles and Contemporary Practices,” *Clin. Infect. Dis.*, vol. 49, no. 11, pp. 1749–1755, Dec. 2009, doi: 10.1086/647952.
- [118] H. Shao *et al.*, “Chip-based analysis of exosomal mRNA mediating drug resistance in glioblastoma,” *Nat. Commun.*, vol. 6, no. 1, Art. no. 1, May 2015, doi: 10.1038/ncomms7999.
- [119] N. Oshimori, D. Oristian, and E. Fuchs, “TGF- β Promotes Heterogeneity and Drug Resistance in Squamous Cell Carcinoma,” *Cell*, vol. 160, no. 5, pp. 963–976, Feb. 2015, doi: 10.1016/j.cell.2015.01.043.
- [120] S. Y. Toh, M. Citartan, S. C. B. Gopinath, and T.-H. Tang, “Aptamers as a replacement for antibodies in enzyme-linked immunosorbent assay,” *Biosens. Bioelectron.*, vol. 64, pp. 392–403, Feb. 2015, doi: 10.1016/j.bios.2014.09.026.
- [121] W. Wu *et al.*, “Gold nanoparticle-based enzyme-linked antibody-aptamer sandwich assay for detection of Salmonella Typhimurium,” *ACS Appl. Mater. Interfaces*, vol. 6, no. 19, pp. 16974–16981, 2014.
- [122] J. Haaber *et al.*, “Bacterial viruses enable their host to acquire antibiotic resistance genes from neighbouring cells,” *Nat. Commun.*, vol. 7, no. 1, Art. no. 1, Nov. 2016, doi: 10.1038/ncomms13333.
- [123] X. Liu *et al.*, “High-throughput screening of antibiotic-resistant bacteria in picodroplets,” *Lab. Chip*, vol. 16, no. 9, pp. 1636–1643, Apr. 2016, doi: 10.1039/C6LC00180G.
- [124] G. Koch *et al.*, “Evolution of resistance to a last-resort antibiotic in *Staphylococcus aureus* via bacterial competition,” *Cell*, vol. 158, no. 5, pp. 1060–1071, 2014.
- [125] S. Sanyasi *et al.*, “Polysaccharide-capped silver Nanoparticles inhibit biofilm formation and eliminate multi-drug-resistant bacteria by disrupting bacterial cytoskeleton with reduced cytotoxicity towards mammalian cells,” *Sci. Rep.*, vol. 6, no. 1, Art. no. 1, Apr. 2016, doi: 10.1038/srep24929.
- [126] R. M. T. de Wildt, C. R. Mundy, B. D. Gorick, and I. M. Tomlinson, “Antibody arrays for high-throughput screening of antibody–antigen interactions,” *Nat. Biotechnol.*, vol. 18, no. 9, Art. no. 9, Sep. 2000, doi: 10.1038/79494.
- [127] N. Tajima, M. Takai, and K. Ishihara, “Significance of Antibody Orientation Unraveled: Well-Oriented Antibodies Recorded High Binding Affinity,” *Anal. Chem.*, vol. 83, no. 6, pp. 1969–1976, Mar. 2011, doi: 10.1021/ac1026786.
- [128] E. García-Fernández *et al.*, “Membrane Microdomain Disassembly Inhibits MRSA Antibiotic Resistance,” *Cell*, vol. 171, no. 6, pp. 1354–1367.e20, Nov. 2017, doi: 10.1016/j.cell.2017.10.012.
- [129] “Membrane-Based, Sedimentation-Assisted Plasma Separator for Point-of-Care Applications | Analytical Chemistry.” <https://pubs.acs.org/doi/10.1021/ac402459h> (accessed Mar. 30, 2021).
- [130] W. Beattie, X. Qin, L. Wang, and H. Ma, “Clog-free cell filtration using resettable cell traps,” *Lab. Chip*, vol. 14, no. 15, pp. 2657–2665, Jul. 2014, doi: 10.1039/C4LC00306C.
- [131] S. C. Hong, J. S. Kang, J. E. Lee, S. S. Kim, and J. H. Jung, “Continuous aerosol size separator using inertial microfluidics and its application to airborne bacteria and viruses,” *Lab. Chip*, vol. 15, no. 8, pp. 1889–1897, 2015.
- [132] S. Shen *et al.*, “Spiral microchannel with ordered micro-obstacles for continuous and highly-efficient particle separation,” *Lab. Chip*, vol. 17, no. 21, pp. 3578–3591, 2017.
- [133] D.-H. Kuan, C.-C. Wu, W.-Y. Su, and N.-T. Huang, “A Microfluidic Device for Simultaneous Extraction of Plasma, Red Blood Cells, and On-Chip White Blood Cell Trapping,” *Sci. Rep.*, vol. 8, no. 1, pp. 1–9, Oct. 2018, doi: 10.1038/s41598-018-33738-8.

- [134] T. Ishikawa, T. Shioiri, K. Numayama-Tsuruta, H. Ueno, Y. Imai, and T. Yamaguchi, "Separation of motile bacteria using drift velocity in a microchannel," *Lab. Chip*, vol. 14, no. 5, pp. 1023–1032, 2014, doi: 10.1039/C3LC51302E.
- [135] B. M. Rudisch *et al.*, "Nonaqueous Micro Free-Flow Electrophoresis for Continuous Separation of Reaction Mixtures in Organic Media," *Anal. Chem.*, vol. 91, no. 10, pp. 6689–6694, May 2019, doi: 10.1021/acs.analchem.9b00714.
- [136] Z.-F. Wang *et al.*, "Ultrasensitive detection of bacteria by microchip electrophoresis based on multiple-concentration approaches combining chitosan sweeping, field-amplified sample stacking, and reversed-field stacking," *Anal. Chem.*, vol. 84, no. 3, pp. 1687–1694, 2012.
- [137] P. Ohlsson *et al.*, "Integrated acoustic separation, enrichment, and microchip polymerase chain reaction detection of bacteria from blood for rapid sepsis diagnostics," *Anal. Chem.*, vol. 88, no. 19, pp. 9403–9411, 2016.
- [138] Y. Ai, C. K. Sanders, and B. L. Marrone, "Separation of Escherichia coli Bacteria from Peripheral Blood Mononuclear Cells Using Standing Surface Acoustic Waves," *Anal. Chem.*, vol. 85, no. 19, pp. 9126–9134, Oct. 2013, doi: 10.1021/ac4017715.
- [139] J. A. Kulkarni *et al.*, "Rapid synthesis of lipid nanoparticles containing hydrophobic inorganic nanoparticles," *Nanoscale*, vol. 9, no. 36, pp. 13600–13609, 2017, doi: 10.1039/C7NR03272B.
- [140] F. Fanalista *et al.*, "Shape and Size Control of Artificial Cells for Bottom-Up Biology," *ACS Nano*, vol. 13, no. 5, pp. 5439–5450, May 2019, doi: 10.1021/acsnano.9b00220.
- [141] K. K. Zeming, S. Ranjan, and Y. Zhang, "Rotational separation of non-spherical bioparticles using I-shaped pillar arrays in a microfluidic device," *Nat. Commun.*, vol. 4, p. 1625, Mar. 2013, doi: 10.1038/ncomms2653.
- [142] L. R. Huang, "Continuous Particle Separation Through Deterministic Lateral Displacement," *Science*, vol. 304, no. 5673, pp. 987–990, May 2004, doi: 10.1126/science.1094567.
- [143] M. Campos *et al.*, "A Constant Size Extension Drives Bacterial Cell Size Homeostasis," *Cell*, vol. 159, no. 6, pp. 1433–1446, Dec. 2014, doi: 10.1016/j.cell.2014.11.022.
- [144] O. Dobe, A. Sarkar, and A. Halder, "Rough K-Means and Morphological Operation-Based Brain Tumor Extraction," in *Integrated Intelligent Computing, Communication and Security*, Springer, 2019, pp. 661–667.
- [145] R. A. Pollack, L. Findlay, W. Mondschein, and R. R. Modesto, *Laboratory Exercises in Microbiology*. John Wiley & Sons, 2018.
- [146] N. Altman and M. Krzywinski, "Clustering," *Nat. Methods*, vol. 14, no. 6, pp. 545–546, Jun. 2017, doi: 10.1038/nmeth.4299.
- [147] E. Essa, X. Xie, R. J. Errington, and N. White, "Phase contrast cell segmentation using machine learning approach," in *Conference proceedings: 4th International Conference on Computational and Mathematical Biomedical Engineering (CMBE)*, Citeseer, 2015.
- [148] K. Anane-Fenin, E. T. Akinlabi, and N. Perry, "Quantification of nanoparticle dispersion within polymer matrix using gap statistics," *Mater. Res. Express*, vol. 6, no. 7, p. 075310, Apr. 2019, doi: 10.1088/2053-1591/ab1106.
- [149] O. Stamati, E. Roubin, E. Andò, and Y. Malecot, "Phase segmentation of concrete x-ray tomographic images at meso-scale: Validation with neutron tomography," *Cem. Concr. Compos.*, vol. 88, pp. 8–16, Apr. 2018, doi: 10.1016/j.cemconcomp.2017.12.011.
- [150] A. Apisarnthanarak, J. Tunpornchai, K. Tanawitt, and L. M. Mundy, "Nonjudicious Dispensing of Antibiotics by Drug Stores in Pratumthani, Thailand," *Infect. Control Hosp. Epidemiol.*, vol. 29, no. 6, pp. 572–575, Jun. 2008, doi: 10.1086/587496.
- [151] N. A. Abahussain and A. Z. Taha, "Knowledge and attitudes of female school students on medications in eastern Saudi Arabia," *Saudi Med. J.*, vol. 28, no. 11, p. 1723, 2007.
- [152] S. T. Micek *et al.*, "Empiric Combination Antibiotic Therapy Is Associated with Improved Outcome against Sepsis Due to Gram-Negative Bacteria: a Retrospective Analysis,"

- Antimicrob. Agents Chemother.*, vol. 54, no. 5, pp. 1742–1748, May 2010, doi: 10.1128/AAC.01365-09.
- [153] V. R. Hill *et al.*, “Development of a rapid method for simultaneous recovery of diverse microbes in drinking water by ultrafiltration with sodium polyphosphate and surfactants,” *Appl. Environ. Microbiol.*, vol. 71, no. 11, pp. 6878–6884, 2005.
- [154] X. T. Zheng and Y. N. Tan, “Development of Blood-Cell-Selective Fluorescent Biodots for Lysis-Free Leukocyte Imaging and Differential Counting in Whole Blood,” *Small*, Aug. 2019, doi: 10.1002/sml.201903328.
- [155] X.-L. Su and Y. Li, “Quantum Dot Biolabeling Coupled with Immunomagnetic Separation for Detection of *Escherichia coli* O157:H7,” *Anal. Chem.*, vol. 76, no. 16, pp. 4806–4810, Aug. 2004, doi: 10.1021/ac049442+.
- [156] L. Malic *et al.*, “Polymer-based microfluidic chip for rapid and efficient immunomagnetic capture and release of *Listeria monocytogenes*,” *Lab. Chip*, vol. 15, no. 20, pp. 3994–4007, 2015, doi: 10.1039/C5LC00852B.
- [157] R. J. Narayan, *Medical Biosensors for Point of Care (POC) Applications*. Woodhead Publishing, 2016.
- [158] H. Shao *et al.*, “Chip-based analysis of exosomal mRNA mediating drug resistance in glioblastoma,” *Nat. Commun.*, vol. 6, p. 6999, 2015.
- [159] N. Oshimori, D. Oristian, and E. Fuchs, “TGF- β promotes heterogeneity and drug resistance in squamous cell carcinoma,” *Cell*, vol. 160, no. 5, pp. 963–976, 2015.
- [160] J. Haaber *et al.*, “Bacterial viruses enable their host to acquire antibiotic resistance genes from neighbouring cells,” *Nat. Commun.*, vol. 7, p. 13333, 2016.
- [161] X. Liu *et al.*, “High-throughput screening of antibiotic-resistant bacteria in picodroplets,” *Lab. Chip*, vol. 16, no. 9, pp. 1636–1643, 2016.
- [162] P. Ohlsson, K. Petersson, P. Augustsson, and T. Laurell, “Acoustic impedance matched buffers enable separation of bacteria from blood cells at high cell concentrations,” *Sci. Rep.*, vol. 8, no. 1, p. 9156, 2018.
- [163] H. G. Kye *et al.*, “Dual-neodymium magnet-based microfluidic separation device,” *Sci. Rep.*, vol. 9, no. 1, pp. 1–10, Jul. 2019, doi: 10.1038/s41598-019-45929-y.
- [164] P. Li and T. J. Huang, “Applications of Acoustofluidics in Bioanalytical Chemistry,” *Anal. Chem.*, vol. 91, no. 1, pp. 757–767, Jan. 2019, doi: 10.1021/acs.analchem.8b03786.
- [165] Y. Cheng, Y. Wang, Z. Ma, W. Wang, and X. Ye, “A bubble-and clogging-free microfluidic particle separation platform with multi-filtration,” *Lab. Chip*, vol. 16, no. 23, pp. 4517–4526, 2016.
- [166] Y. Yoon *et al.*, “Clogging-free microfluidics for continuous size-based separation of microparticles,” *Sci. Rep.*, vol. 6, p. 26531, 2016.
- [167] Z. Jin *et al.*, “Metallized DNA nanolithography for encoding and transferring spatial information for graphene patterning,” *Nat. Commun.*, vol. 4, p. 1663, 2013.
- [168] S. Kim *et al.*, “All-water-based electron-beam lithography using silk as a resist,” *Nat. Nanotechnol.*, vol. 9, no. 4, p. 306, 2014.
- [169] N. Lebleu, C. Roques, P. Aimar, and C. Causserand, “Role of the cell-wall structure in the retention of bacteria by microfiltration membranes,” *J. Membr. Sci.*, vol. 326, no. 1, pp. 178–185, Jan. 2009, doi: 10.1016/j.memsci.2008.09.049.
- [170] A. L. Zydney, W. M. Saltzman, and C. K. Colton, “Hydraulic resistance of red cell beds in an unstirred filtration cell,” *Chem. Eng. Sci.*, vol. 44, no. 1, pp. 147–159, 1989.
- [171] T. Ahmed, T. S. Shimizu, and R. Stocker, “Microfluidics for bacterial chemotaxis,” *Integr. Biol.*, vol. 2, no. 11–12, pp. 604–629, Nov. 2010, doi: 10.1039/c0ib00049c.
- [172] D. J. Beebe, G. A. Mensing, and G. M. Walker, “Physics and applications of microfluidics in biology,” *Annu. Rev. Biomed. Eng.*, vol. 4, no. 1, pp. 261–286, 2002.
- [173] H. Gu, P.-L. Ho, K. W. T. Tsang, L. Wang, and B. Xu, “Using Biofunctional Magnetic Nanoparticles to Capture Vancomycin-Resistant Enterococci and Other Gram-Positive

- Bacteria at Ultralow Concentration,” *J. Am. Chem. Soc.*, vol. 125, no. 51, pp. 15702–15703, Dec. 2003, doi: 10.1021/ja0359310.
- [174] C. Qian *et al.*, “Oxygen-Detecting Synaptic Device for Realization of Artificial Autonomic Nervous System for Maintaining Oxygen Homeostasis,” *Adv. Mater.*, vol. 32, no. 34, p. 2002653, 2020, doi: 10.1002/adma.202002653.
- [175] S. C. Cowin and L. Cardoso, “Blood and interstitial flow in the hierarchical pore space architecture of bone tissue,” *J. Biomech.*, vol. 48, no. 5, pp. 842–854, 2015.
- [176] O. Herrmann *et al.*, “Regulation of body temperature and neuroprotection by endogenous interleukin-6 in cerebral ischemia,” *J. Cereb. Blood Flow Metab.*, vol. 23, no. 4, pp. 406–415, 2003.
- [177] Y. Li, Y. Xiong, R. Wang, F. Tang, and X. Wang, “Blood banking-induced alteration of red blood cell oxygen release ability,” *Blood Transfus.*, vol. 14, no. 3, pp. 238–244, May 2016, doi: 10.2450/2015.0055-15.
- [178] H. W. Hou, A. A. S. Bhagat, W. C. Lee, S. Huang, J. Han, and C. T. Lim, “Microfluidic Devices for Blood Fractionation,” *Micromachines*, vol. 2, no. 3, Art. no. 3, Sep. 2011, doi: 10.3390/mi2030319.
- [179] M. Islam, M. Motasim Bellah, A. Sajid, M. Raziul Hasan, Y. Kim, and S. M. Iqbal, “Effects of Nanotexture on Electrical Profiling of Single Tumor Cell and Detection of Cancer from Blood in Microfluidic Channels,” *Sci. Rep.*, vol. 5, no. 1, Art. no. 1, Sep. 2015, doi: 10.1038/srep13031.
- [180] Z. Zhao, Y. Yang, Y. Zeng, and M. He, “A microfluidic ExoSearch chip for multiplexed exosome detection towards blood-based ovarian cancer diagnosis,” *Lab. Chip*, vol. 16, no. 3, pp. 489–496, 2016, doi: 10.1039/C5LC01117E.
- [181] K. K. Zeming *et al.*, “Label-Free Biophysical Markers from Whole Blood Microfluidic Immune Profiling Reveal Severe Immune Response Signatures,” *Small*, vol. 17, no. 12, p. 2006123, 2021, doi: <https://doi.org/10.1002/sml.202006123>.
- [182] F. Ellett *et al.*, “Diagnosis of sepsis from a drop of blood by measurement of spontaneous neutrophil motility in a microfluidic assay,” *Nat. Biomed. Eng.*, vol. 2, no. 4, pp. 207–214, Apr. 2018, doi: 10.1038/s41551-018-0208-z.
- [183] M. Grau *et al.*, “Effect of acute exercise on RBC deformability and RBC nitric oxide synthase signalling pathway in young sickle cell anaemia patients,” *Sci. Rep.*, vol. 9, no. 1, Art. no. 1, Aug. 2019, doi: 10.1038/s41598-019-48364-1.
- [184] J. R. Pawloski, D. T. Hess, and J. S. Stamler, “Impaired vasodilation by red blood cells in sickle cell disease,” *Proc. Natl. Acad. Sci.*, vol. 102, no. 7, pp. 2531–2536, Feb. 2005, doi: 10.1073/pnas.0409876102.
- [185] M. Kotepui, D. Piwkham, B. PhunPhuech, N. Phiwklam, C. Chupeerach, and S. Duangmano, “Effects of Malaria Parasite Density on Blood Cell Parameters,” *PLOS ONE*, vol. 10, no. 3, p. e0121057, Mar. 2015, doi: 10.1371/journal.pone.0121057.
- [186] D. R. Gossett *et al.*, “Label-free cell separation and sorting in microfluidic systems,” *Anal. Bioanal. Chem.*, vol. 397, no. 8, pp. 3249–3267, Aug. 2010, doi: 10.1007/s00216-010-3721-9.
- [187] M. S. Maria, P. E. Rakesh, T. S. Chandra, and A. K. Sen, “Capillary flow-driven microfluidic device with wettability gradient and sedimentation effects for blood plasma separation,” *Sci. Rep.*, vol. 7, no. 1, Art. no. 1, Mar. 2017, doi: 10.1038/srep43457.
- [188] B. A. Walker *et al.*, “Intraclonal heterogeneity is a critical early event in the development of myeloma and precedes the development of clinical symptoms,” *Leukemia*, vol. 28, no. 2, Art. no. 2, Feb. 2014, doi: 10.1038/leu.2013.199.
- [189] H. C. M. T. Prinsen *et al.*, “Rapid quantification of underivatized amino acids in plasma by hydrophilic interaction liquid chromatography (HILIC) coupled with tandem mass-spectrometry,” *J. Inherit. Metab. Dis.*, vol. 39, no. 5, pp. 651–660, 2016, doi: 10.1007/s10545-016-9935-z.

- [190] J. Korsak and Z. Wańkiewicz, “New Options of Apheresis in Renal Diseases: How and When?,” *Blood Purification*, vol. 41, no. 1–3, pp. 1–10, 2015.
- [191] L. Cao, A. Cobbs, R. P. Simon, and A. Zhou, “Distinct plasma proteomic changes in male and female African American stroke patients,” *Int. J. Physiol. Pathophysiol. Pharmacol.*, vol. 11, no. 2, pp. 12–20, Apr. 2019.
- [192] L. He *et al.*, “Diagnosis of Hemoglobinopathy and β -Thalassemia by 21 Tesla Fourier Transform Ion Cyclotron Resonance Mass Spectrometry and Tandem Mass Spectrometry of Hemoglobin from Blood,” *Clin. Chem.*, vol. 65, no. 8, pp. 986–994, Aug. 2019, doi: 10.1373/clinchem.2018.295766.
- [193] Y. K. Lee *et al.*, “Recent progress in laboratory diagnosis of thalassemia and hemoglobinopathy: a study by the Korean Red Blood Cell Disorder Working Party of the Korean Society of Hematology,” *Blood Res.*, vol. 54, no. 1, pp. 17–22, Mar. 2019, doi: 10.5045/br.2019.54.1.17.
- [194] V. VanDelinder and A. Groisman, “Separation of Plasma from Whole Human Blood in a Continuous Cross-Flow in a Molded Microfluidic Device,” *Anal. Chem.*, vol. 78, no. 11, pp. 3765–3771, Jun. 2006, doi: 10.1021/ac060042r.
- [195] T. A. Crowley and V. Pizziconi, “Isolation of plasma from whole blood using planar microfilters for lab-on-a-chip applications,” *Lab. Chip*, vol. 5, no. 9, pp. 922–929, 2005, doi: 10.1039/B502930A.
- [196] J. Moorthy and D. J. Beebe, “In situ fabricated porous filters for microsystems,” *Lab. Chip*, vol. 3, no. 2, pp. 62–66, May 2003, doi: 10.1039/B300450C.
- [197] J. S. Shim, A. W. Browne, and C. H. Ahn, “An on-chip whole blood/plasma separator with bead-packed microchannel on COC polymer,” *Biomed. Microdevices*, vol. 12, no. 5, pp. 949–957, Oct. 2010, doi: 10.1007/s10544-010-9449-7.
- [198] C. Li, C. Liu, Z. Xu, and J. Li, “Extraction of plasma from whole blood using a deposited microbead plug (DMBP) in a capillary-driven microfluidic device,” *Biomed. Microdevices*, vol. 14, no. 3, pp. 565–572, Jun. 2012, doi: 10.1007/s10544-012-9635-x.
- [199] J.-N. Kuo and B.-Y. Lin, “Microfluidic blood-plasma separation chip using channel size filtration effect,” *Microsyst. Technol.*, vol. 24, no. 4, pp. 2063–2070, Apr. 2018, doi: 10.1007/s00542-017-3607-2.
- [200] R. Zhong, N. Wu, and Y. Liu, “Microfluidic Human Blood Plasma Separation for Lab on Chip Based Heavy Metal Detections,” *ECS Trans.*, vol. 41, no. 38, p. 11, May 2012, doi: 10.1149/1.3697855.
- [201] Y. Wu *et al.*, “Continuously Tunable Ion Rectification and Conductance in Submicrochannels Stemming from Thermoresponsive Polymer Self-Assembly,” *Angew. Chem.*, vol. 131, no. 36, pp. 12611–12615, 2019, doi: 10.1002/ange.201906360.
- [202] M. Wang *et al.*, “Dynamic Curvature Nanochannel-Based Membrane with Anomalous Ionic Transport Behaviors and Reversible Rectification Switch,” *Adv. Mater.*, vol. 31, no. 11, p. 1805130, 2019, doi: 10.1002/adma.201805130.
- [203] S. W. Lee and S. S. Lee, “Shrinkage ratio of PDMS and its alignment method for the wafer level process,” *Microsyst. Technol.*, vol. 14, no. 2, pp. 205–208, Feb. 2008, doi: 10.1007/s00542-007-0417-y.
- [204] X. Chen *et al.*, “Rapid *Escherichia coli* Trapping and Retrieval from Bodily Fluids via a Three-Dimensional Bead-Stacked Nanodevice,” *ACS Appl. Mater. Interfaces*, vol. 12, no. 7, Art. no. 7, Feb. 2020, doi: 10.1021/acsami.9b19311.
- [205] X. Chen, S. Zhang, Y. Gan, R. Liu, R.-Q. Wang, and K. Du, “Understanding microbeads stacking in deformable Nano-Sieve for Efficient plasma separation and blood cell retrieval,” *J. Colloid Interface Sci.*, vol. 606, pp. 1609–1616, Jan. 2022, doi: 10.1016/j.jcis.2021.08.119.
- [206] *British Standard 903 (1950, 1957). Methods of testing vulcanized rubber, Part 19 (1950) and Part A7 (1957).*

- [207] J. Tang *et al.*, “Study on a novel composite coating based on PDMS doped with modified graphene oxide,” *J. Coat. Technol. Res.*, vol. 15, no. 2, pp. 375–383, Mar. 2018, doi: 10.1007/s11998-017-9991-9.
- [208] G. Tomaiuolo, M. Simeone, V. Martinelli, B. Rotoli, and S. Guido, “Red blood cell deformation in microconfined flow,” *Soft Matter*, vol. 5, no. 19, pp. 3736–3740, 2009, doi: 10.1039/B904584H.
- [209] Y.-Z. Yoon, J. Kotar, G. Yoon, and P. Cicutta, “The nonlinear mechanical response of the red blood cell,” *Phys. Biol.*, vol. 5, no. 3, p. 036007, Aug. 2008, doi: 10.1088/1478-3975/5/3/036007.
- [210] M. Fakhrol Ulum, L. Maylina, D. Noviana, and D. H. Bagus Wicaksono, “EDTA-treated cotton-thread microfluidic device used for one-step whole blood plasma separation and assay,” *Lab. Chip*, vol. 16, no. 8, pp. 1492–1504, 2016, doi: 10.1039/C6LC00175K.
- [211] M. Rafeie, J. Zhang, M. Asadnia, W. Li, and M. Ebrahimi Warkiani, “Multiplexing slanted spiral microchannels for ultra-fast blood plasma separation,” *Lab. Chip*, vol. 16, no. 15, pp. 2791–2802, 2016, doi: 10.1039/C6LC00713A.
- [212] K. Suhre *et al.*, “Connecting genetic risk to disease end points through the human blood plasma proteome,” *Nat. Commun.*, vol. 8, no. 1, Art. no. 1, Feb. 2017, doi: 10.1038/ncomms14357.
- [213] I. A. Zaporozhchenko *et al.*, “Profiling of 179 miRNA Expression in Blood Plasma of Lung Cancer Patients and Cancer-Free Individuals,” *Sci. Rep.*, vol. 8, no. 1, Art. no. 1, Apr. 2018, doi: 10.1038/s41598-018-24769-2.
- [214] R. D. Crapnell *et al.*, “Toward the Rapid Diagnosis of Sepsis: Detecting Interleukin-6 in Blood Plasma Using Functionalized Screen-Printed Electrodes with a Thermal Detection Methodology,” *Anal. Chem.*, vol. 93, no. 14, pp. 5931–5938, Apr. 2021, doi: 10.1021/acs.analchem.1c00417.
- [215] B. S. Lee *et al.*, “A fully automated immunoassay from whole blood on a disc,” *Lab. Chip*, vol. 9, no. 11, p. 1548, 2009, doi: 10.1039/b820321k.
- [216] C. Liu *et al.*, “Membrane-based, sedimentation-assisted plasma separator for point-of-care applications,” *Anal. Chem.*, vol. 85, no. 21, pp. 10463–10470, Nov. 2013, doi: 10.1021/ac402459h.
- [217] T. G. Kang, Y.-J. Yoon, H. Ji, P. Y. Lim, and Y. Chen, “A continuous flow micro filtration device for plasma/blood separation using submicron vertical pillar gap structures,” *J. Micromechanics Microengineering*, vol. 24, no. 8, p. 087001, Aug. 2014, doi: 10.1088/0960-1317/24/8/087001.
- [218] M. Kersaudy-Kerhoas and E. Sollier, “Micro-scale blood plasma separation: from acoustophoresis to egg-beaters,” *Lab. Chip*, vol. 13, no. 17, pp. 3323–3346, 2013, doi: 10.1039/C3LC50432H.
- [219] D. Kim, J. Y. Yun, S.-J. Park, and S. S. Lee, “Effect of microstructure on blood cell clogging in blood separators based on capillary action,” *Microsyst. Technol.*, vol. 15, no. 2, pp. 227–233, Feb. 2009, doi: 10.1007/s00542-008-0663-7.
- [220] T. Thomas *et al.*, “Evidence of Structural Protein Damage and Membrane Lipid Remodeling in Red Blood Cells from COVID-19 Patients,” *J. Proteome Res.*, vol. 19, no. 11, pp. 4455–4469, Nov. 2020, doi: 10.1021/acs.jproteome.0c00606.
- [221] M. Laforge *et al.*, “Tissue damage from neutrophil-induced oxidative stress in COVID-19,” *Nat. Rev. Immunol.*, vol. 20, no. 9, Art. no. 9, Sep. 2020, doi: 10.1038/s41577-020-0407-1.
- [222] M. Hosokawa *et al.*, “Leukocyte counting from a small amount of whole blood using a size-controlled microcavity array,” *Biotechnol. Bioeng.*, vol. 109, no. 8, pp. 2017–2024, 2012, doi: <https://doi.org/10.1002/bit.24471>.
- [223] G. Nardone *et al.*, “YAP regulates cell mechanics by controlling focal adhesion assembly,” *Nat. Commun.*, vol. 8, no. 1, Art. no. 1, May 2017, doi: 10.1038/ncomms15321.

- [224] M. R. Zanotelli *et al.*, “Energetic costs regulated by cell mechanics and confinement are predictive of migration path during decision-making,” *Nat. Commun.*, vol. 10, no. 1, Art. no. 1, Sep. 2019, doi: 10.1038/s41467-019-12155-z.
- [225] C. ten Pas, K. Du, L. Pan, R.-Q. Wang, and S. Xu, “Understanding the dynamics of fluid–structure interaction with an Air Deflected Microfluidic Chip (ADMC),” *Sci. Rep.*, vol. 12, no. 1, Art. no. 1, Nov. 2022, doi: 10.1038/s41598-022-24112-w.
- [226] A. Tarín-Pelló, B. Suay-García, and M.-T. Pérez-Gracia, “Antibiotic resistant bacteria: current situation and treatment options to accelerate the development of a new antimicrobial arsenal,” *Expert Rev. Anti Infect. Ther.*, vol. 20, no. 8, pp. 1095–1108, Aug. 2022, doi: 10.1080/14787210.2022.2078308.
- [227] J. O’Neill, “Tackling a global health crisis: initial steps,” *Rev. Antimicrob. Resist. Chaired Jim O’Neill*, 2015.
- [228] Q. Chen *et al.*, “CRISPR–Cas12-based field-deployable system for rapid detection of synthetic DNA sequence of the monkeypox virus genome,” *J. Med. Virol.*, vol. 95, no. 1, p. e28385, 2023, doi: 10.1002/jmv.28385.
- [229] P. Qin *et al.*, “Rapid and Fully Microfluidic Ebola Virus Detection with CRISPR-Cas13a,” *ACS Sens.*, vol. 4, no. 4, pp. 1048–1054, Apr. 2019, doi: 10.1021/acssensors.9b00239.
- [230] L. Liu, M. Dubrovsky, S. Gundavarapu, D. Vermeulen, and K. Du, “Viral nucleic acid detection with CRISPR-Cas12a using high contrast cleavage detection on micro-ring resonator biosensors,” in *Frontiers in Biological Detection: From Nanosensors to Systems XIII*, SPIE, Mar. 2021, pp. 8–13. doi: 10.1117/12.2580053.
- [231] J. S. Chen *et al.*, “CRISPR-Cas12a target binding unleashes indiscriminate single-stranded DNase activity,” *Science*, vol. 360, no. 6387, pp. 436–439, Apr. 2018, doi: 10.1126/science.aar6245.
- [232] O. Dmytrenko *et al.*, “Cas12a2 elicits abortive infection through RNA-triggered destruction of dsDNA,” *Nature*, vol. 613, no. 7944, Art. no. 7944, Jan. 2023, doi: 10.1038/s41586-022-05559-3.
- [233] L. Wang *et al.*, “A CRISPR/Cas12a-based label-free fluorescent method for visual signal output,” *Sens. Actuators B Chem.*, vol. 370, p. 132368, Nov. 2022, doi: 10.1016/j.snb.2022.132368.
- [234] M. Zeng *et al.*, “Harnessing multiplex CRRNA in the CRISPR/Cas12a system enables an amplification-free DNA diagnostic platform for ASFV detection,” *Anal. Chem.*, vol. 94, no. 30, pp. 10805–10812, 2022.
- [235] X. Liu *et al.*, “Electrochemical biosensor for detecting pathogenic bacteria based on a hybridization chain reaction and CRISPR-Cas12a,” *Anal. Bioanal. Chem.*, pp. 1–8, 2022.
- [236] W. Feng *et al.*, “Integrating reverse transcription recombinase polymerase amplification with CRISPR technology for the one-tube assay of RNA,” *Anal. Chem.*, vol. 93, no. 37, pp. 12808–12816, 2021.
- [237] M. Qing, S. L. Chen, Z. Sun, Y. Fan, H. Q. Luo, and N. B. Li, “Universal and programmable rolling circle amplification–CRISPR/Cas12a-mediated immobilization-free electrochemical biosensor,” *Anal. Chem.*, vol. 93, no. 20, pp. 7499–7507, 2021.
- [238] M. Zhang, H. Wang, H. Wang, F. Wang, and Z. Li, “CRISPR/Cas12a-assisted ligation-initiated loop-mediated isothermal amplification (CAL-LAMP) for highly specific detection of microRNAs,” *Anal. Chem.*, vol. 93, no. 22, pp. 7942–7948, 2021.
- [239] Q. He *et al.*, “High-throughput and all-solution phase African Swine Fever Virus (ASFV) detection using CRISPR-Cas12a and fluorescence based point-of-care system,” *Biosens. Bioelectron.*, vol. 154, p. 112068, Apr. 2020, doi: 10.1016/j.bios.2020.112068.
- [240] T. Sukonta, S. Senapin, W. Meemetta, and T. Chaijarasphong, “CRISPR-based platform for rapid, sensitive and field-deployable detection of scale drop disease virus in Asian sea bass (*Lates calcarifer*),” *J. Fish Dis.*, vol. 45, no. 1, pp. 107–120, 2022.

- [241] Z. Li, X. Xu, D. Wang, and X. Jiang, “Recent advancements in nucleic acid detection with microfluidic chip for molecular diagnostics,” *TrAC Trends Anal. Chem.*, p. 116871, 2022.
- [242] Y.-L. Fang *et al.*, “An integrated microfluidic system for early detection of sepsis-inducing bacteria,” *Lab. Chip*, vol. 21, no. 1, pp. 113–121, 2021.
- [243] A. Nanaware *et al.*, “Pneumatic controlled nanosieve for efficient capture and release of nanoparticles,” *J. Vac. Sci. Technol. B*, vol. 40, no. 6, 2022.
- [244] K. Du *et al.*, “Multiplexed efficient on-chip sample preparation and sensitive amplification-free detection of Ebola virus,” *Biosens. Bioelectron.*, vol. 91, pp. 489–496, 2017, doi: <https://doi.org/10.1016/j.bios.2016.12.071>.
- [245] K. Yin, X. Ding, Z. Li, H. Zhao, K. Cooper, and C. Liu, “Dynamic aqueous multiphase reaction system for one-pot CRISPR-Cas12a-based ultrasensitive and quantitative molecular diagnosis,” *Anal. Chem.*, vol. 92, no. 12, pp. 8561–8568, 2020.
- [246] R. Aman, A. Mahas, T. Marsic, N. Hassan, and M. M. Mahfouz, “Efficient, rapid, and sensitive detection of plant RNA viruses with one-pot RT-RPA–CRISPR/Cas12a assay,” *Front. Microbiol.*, vol. 11, p. 610872, 2020.
- [247] T. van der Poll, M. Shankar-Hari, and W. J. Wiersinga, “The immunology of sepsis,” *Immunity*, vol. 54, no. 11, pp. 2450–2464, 2021.
- [248] R. Sherwin, M. E. Winters, G. M. Vilke, and G. Wardi, “Does Early and Appropriate Antibiotic Administration Improve Mortality in Emergency Department Patients with Severe Sepsis or Septic Shock?,” *J. Emerg. Med.*, vol. 53, no. 4, pp. 588–595, Oct. 2017, doi: [10.1016/j.jemermed.2016.12.009](https://doi.org/10.1016/j.jemermed.2016.12.009).
- [249] E. E. Lebovitz and P. D. Burbelo, “Commercial Multiplex Technologies for the Microbiological Diagnosis of Sepsis,” *Mol. Diagn. Ther.*, vol. 17, no. 4, pp. 221–231, Aug. 2013, doi: [10.1007/s40291-013-0037-4](https://doi.org/10.1007/s40291-013-0037-4).
- [250] K. Du, Y. Liu, I. Wathuthanthri, and C.-H. Choi, “Dual applications of free-standing holographic nanopatterns for lift-off and stencil lithography,” *J. Vac. Sci. Technol. B*, vol. 30, no. 6, p. 06FF04, Oct. 2012, doi: [10.1116/1.4757110](https://doi.org/10.1116/1.4757110).
- [251] D. Thiry *et al.*, “The Kirkendall Effect in Binary Alloys: Trapping Gold in Copper Oxide Nanoshells,” *Chem. Mater.*, vol. 27, no. 18, pp. 6374–6384, Sep. 2015, doi: [10.1021/acs.chemmater.5b02391](https://doi.org/10.1021/acs.chemmater.5b02391).
- [252] Z. Zheng *et al.*, “Two-stage activated nano-truck enhanced specific aggregation and deep delivery for synergistic tumor ablation,” *Nanoscale*, vol. 12, no. 29, pp. 15845–15856, Jul. 2020, doi: [10.1039/D0NR03661G](https://doi.org/10.1039/D0NR03661G).
- [253] Y. Jia, P. Shen, T. Yan, W. Zhou, J. Sun, and X. Han, “Microfluidic Tandem Mechanical Sorting System for Enhanced Cancer Stem Cell Isolation and Ingredient Screening,” *Adv. Healthc. Mater.*, vol. 10, no. 20, p. 2100985, 2021, doi: [10.1002/adhm.202100985](https://doi.org/10.1002/adhm.202100985).
- [254] S. Guo, X. Chen, Y. Wan, S. Feng, and J. Luo, “Custom-Tailoring Loose Nanofiltration Membrane for Precise Biomolecule Fractionation: New Insight into Post-Treatment Mechanisms,” *ACS Appl. Mater. Interfaces*, vol. 12, no. 11, pp. 13327–13337, Mar. 2020, doi: [10.1021/acsami.0c00259](https://doi.org/10.1021/acsami.0c00259).
- [255] D. J. Berard *et al.*, “Convex lens-induced nanoscale templating,” *Proc. Natl. Acad. Sci.*, vol. 111, no. 37, pp. 13295–13300, Sep. 2014, doi: [10.1073/pnas.1321089111](https://doi.org/10.1073/pnas.1321089111).
- [256] M. N. Hamblin *et al.*, “Selective trapping and concentration of nanoparticles and viruses in dual-height nanofluidic channels,” *Lab. Chip*, vol. 10, no. 2, pp. 173–178, Dec. 2009, doi: [10.1039/B916746C](https://doi.org/10.1039/B916746C).
- [257] K.-T. Liao, J. Schumacher, H. J. Lezec, and S. M. Stavis, “Subnanometer structure and function from ion beams through complex fluidics to fluorescent particles,” *Lab. Chip*, vol. 18, no. 1, pp. 139–152, 2018, doi: [10.1039/C7LC01047H](https://doi.org/10.1039/C7LC01047H).
- [258] C. Wang *et al.*, “Wafer-scale integration of sacrificial nanofluidic chips for detecting and manipulating single DNA molecules,” *Nat. Commun.*, vol. 8, no. 1, Art. no. 1, Jan. 2017, doi: [10.1038/ncomms14243](https://doi.org/10.1038/ncomms14243).

- [259] X. Chen *et al.*, “Rapid *Escherichia coli* Trapping and Retrieval from Bodily Fluids via a Three-Dimensional Bead-Stacked Nanodevice,” *ACS Appl. Mater. Interfaces*, vol. 12, no. 7, pp. 7888–7896, Feb. 2020, doi: 10.1021/acsami.9b19311.
- [260] A. I. Barros, A. L. Gonçalves, M. Simões, and J. C. M. Pires, “Harvesting techniques applied to microalgae: A review,” *Renew. Sustain. Energy Rev.*, vol. 41, pp. 1489–1500, Jan. 2015, doi: 10.1016/j.rser.2014.09.037.
- [261] C. Wan *et al.*, “Current progress and future prospect of microalgal biomass harvest using various flocculation technologies,” *Bioresour. Technol.*, vol. 184, pp. 251–257, May 2015, doi: 10.1016/j.biortech.2014.11.081.
- [262] T. Searchinger *et al.*, “Use of U.S. Croplands for Biofuels Increases Greenhouse Gases Through Emissions from Land-Use Change,” *Science*, vol. 319, no. 5867, pp. 1238–1240, Feb. 2008, doi: 10.1126/science.1151861.
- [263] A. Gosset *et al.*, “Xurography-based microfluidic algal biosensor and dedicated portable measurement station for online monitoring of urban polluted samples,” *Biosens. Bioelectron.*, vol. 117, pp. 669–677, Oct. 2018, doi: 10.1016/j.bios.2018.07.005.
- [264] Y. Chang, M. Bao, J. Waitkus, H. Cai, and K. Du, “On-Demand Fully Enclosed Superhydrophobic–Optofluidic Devices Enabled by Microstereolithography,” *Langmuir*, vol. 38, no. 34, pp. 10672–10678, Aug. 2022, doi: 10.1021/acs.langmuir.2c01658.

Appendix A

Table A.1 Bill of Materials

Name of Materials/Equipment	Vender/Source	Catalog number
Polydimethylsiloxane (PDMS, SYLGARD™ 184)	Ellsworth Adhesives	SKU: 2065622
The fluorescent microspheres (5 µm in diameter)	Thermo Fisher Scientific	35-2B
The fluorescent nanoparticles (100 nm in diameter)	CD Bioparticles	DCFG-L003
The glass wafer (D263, 150 mm in diameter, 550 µm in thickness, double side polished)	University Wafer	ID# 1618
Applied Materials P5000 (Chamber A - PECVD of TEOS Silicon Dioxide)	RIT SMFL	N/A
Positive photoresist (AZ Mir™ 701)	RIT SMFL	N/A
Buffered oxide etching (BOE) bench (10:1 BOE Tank is for general oxide etching.)	RIT SMFL	N/A
Biopsy punch (1 mm in diameter)	Integra LifeSciences	33-31AA-P/25
BD-20AC laboratory corona treater	Electro-Technic Products	SKU: 12051A
JASCO FP-8500 spectrofluorometer	JASCO Global	N/A
CD-26 developer solution	Rohm and Haas Electronic Materials LLC	N/A
<i>Escherichia coli</i> (<i>E.coli</i>) bacteria cells	ATCC	ATCC 25922
Bacteria-free <i>C. reinhardtii</i> cells	Carolina Biological Supply	Item #: 152040
Multichannel syringe pump	eBay	WPI SP220I
Amscope XD-RFL microscope	AmScope	N/A
Scanning electron microscopy (Tescan Mira3)	RIT imaging science	N/A
Magnetic beads (10 mg/mL, 5 µm in diameter)	Alpha Nanotech Inc	N/A
Magnetic beads (10 mg/mL, 10 µm in diameter)	Alpha Nanotech Inc	N/A
Magnetic beads (2.8 µm in diameter)	Thermo Fisher Scientific	N/A
PBS (1× without calcium and magnesium, PH 7.4 ± 0.1)	Corning Inc	N/A
<i>BacLight</i> ™ Green Bacterial Stain	Thermo Fisher Scientific	B35000
Pig plasma solution	Sigma Aldrich	P2891-10 mL
Microcentrifuge (VWR Galaxy Mini C1213)	VWR International, LLC	N/A
Eulerian multiphase model (FLUENT 19.2)	ANSYS	N/A

Optical coherence tomography system	Thorlab	N/A
Digital microscope high-speed camera	Zeiss	AxioCam MRc, Zeiss
SPI-Module™ Sputter Coater	RIT imaging science	N/A
Human whole peripheral blood (Fresh, EDTA, 10 mL)	STEMCELL Technologies	70508.1
FstDgte Shore A durometer	RIT	N/A
a Chatillon® TCD1221 digital force tester	RIT	N/A
EasySep™ RBC depletion reagent	STEMCELL Technologies	18170
Microfluidic tubing	Scientific Commodities, Inc.	BB31695-PE/3
Photoresist mask (plastic)	Fineline Imaging	N/A
3-D printed mold for pneumatic chamber	Fictiv	N/A
iFlow Touch™ Microfluidic Pump System	Precigenome LLC	N/A
BD Luer-Lok™ 1 mL syringe	BD	N/A
Methicillin-resistant Staphylococcus aureus	ATCC	43300
Tryptic soy broth medium	MilliporeSigma	22092-500G
Ethylene-diaminetetraacetic acid (EDTA)	Rockland	MB-014
Lysozyme	Thermo Fisher	N/A
Triton X-100 (1.2%)	Thermo Fisher	N/A
Tris-HCl (20 mM)	Thermo Fisher	N/A
Proteinase K	Thermo Fisher	N/A
AMPure XP beads	Beckman Coulter	A63880
Nuclease-free water	Thermo Fisher	N/A
Guanidinium chloride	MilliporeSigma	N/A
TwistAmp® Basic kit	TwistDx™	N/A
The RPA primers, crRNA, AsCas12a, and fluorophore-quencher probes	Integrated DNA Technologies	N/A
NEBuffer™ r2.1	New England Biolabs	N/A
Blue light transilluminator	SmartBlue	NEB-E4100
Agilent BioTek Cytation 5 imaging reader	Agilent Technologies	Cytation 5